Composite Structures 370 (2025) 119329

Contents lists available at ScienceDirect

Composite Structures

journal homepage: www.elsevier.com/locate/compstruct

Hygro-thermal coupling effect on the magneto-mechanical response of curved laminated structures

Francesco Tornabene [*], Matteo Viscoti, Rossana Dimitri

Department of Innovation Engineering, School of Engineering, University of Salento, 73100 Lecce, Italy

ARTICLE INFO

Keywords:
Equivalent Layer-Wise
Hygro-thermal coupling
Navier solution
Piezomagnetic
Shell structures
Smart materials

ABSTRACT

This paper presents a refined two-dimensional model, based on higher-order theories, for the hygro-thermo-magneto-mechanical analysis of doubly-curved laminated shell structures. The formulation employs a generalized kinematic model with zigzag functions, and it uses curvilinear principal coordinates to describe the geometry of the panel. The model allows us to assess arbitrary values of the multifield unknown variables, due to their description by using the Equivalent-Layer-Wise approach. The multifield analysis considers the coupling between various physical effects, including hygro-thermal, piezomagnetic, pyromagnetic, and hygro-magnetic constitutive interactions. The panel rests on an elastic foundation modelled with the Winkler-Pasternak theory. Furthermore, each layer is homogenized with proper analytical expressions and it is treated as a continuum material. The fundamental equations are solved analytically using the Navier method, while a recovery procedure based on three-dimensional balance equations reconstructs the multifield primary and secondary variable distribution in the post-processing stage. The method adopts the generalized differential and integral quadrature to solve the equations. Numerical examples demonstrate the accuracy and the efficiency of the theory compared to more computationally demanding three-dimensional solutions obtained with a commercial finite element software. Furthermore, parametric studies explore the sensitivity of governing parameters, considering various curvatures and lamination schemes, load shapes, and load combinations. The model serves as a useful tool for investigating the multifield response of curved laminates with simplicity and less computational effort. It can be used for exploring new insights into the multifield coupling effects that are not considered in commonly used software for multifield analysis.

1. Introduction

New advances in engineering fields require sophisticated models to predict the structural response under various environmental conditions and physical phenomena [1–3]. For instance, refined numerical models are being developed for applications in biomedical engineering [4], aerospace industry [5], and civil engineering [6], focusing on the effect of moisture diffusion and heat exchange. Moisture and elevated temperature can induce additional stress and strain states within structures, potentially leading to unexpected failure or damage if not adequately considered during the design process [7,8]. In fact, each physical phenomenon influences the mechanical response of a structure. For example, hygrometric and thermal effects can alter the material properties of both the isotropic matrix and the reinforcing fibers in composite materials, leading to a degradation of the overall mechanical performance [9]. Moreover, the simultaneous presence of temperature and moisture distributions within a structure introduces combined effects that differ from those caused by individual phenomena alone. The experimental evidence has largely shown that an increased temperature can induce a moisture migration within a solid, and conversely, a moisture concentration gradient can induce pronounced temperature variations [8]. These phenomena are referred to as thermophoretic effect and thermal diffusion effect, respectively. Despite their significance, theoretical investigations on these effects remain relatively scarce [9], with existing studies relying on the Onsager principle to derive phenomenological coefficients in the constitutive relations [10]. When a structure is exposed to a hygrothermal environment and interacts with magnetic fields, temperature variations and moisture content can alter the distribution of magnetic quantities within the solid. These interactions, known as pyromagnetic and hygromagnetic effects, are not commonly addressed in practical applications [11–13]. However, they can be modelled if a proper constitutive relationship for the material is

---

[*] Corresponding author.
E-mail address: francesco.tornabene@unisalento.it (F. Tornabene).

https://doi.org/10.1016/j.compstruct.2025.119329
Received 19 February 2025; Received in revised form 17 April 2025; Accepted 22 May 2025

available, which couple magnetic field with temperature and moisture gradient components. Furthermore, minor variations in magnetic fields induced by changes in temperature and moisture content, can generate strain and stress states within the structure composed of piezomagnetic materials, emphasizing the need for accurate modelling of these coupled effects. In multifield analysis, additional terms and variables are introduced into the governing equations [14,15], thus increasing the computational cost for numerical investigations. For this reason, it is important to employ efficient formulations that balance accuracy with computational efficiency. Many formulations in the literature make simplifying assumptions about multifield unknown variables, which are then used to compute the corresponding deflection. For instance, in the thermo-mechanical analyses from Refs. [16,17], a linear or a parabolic profile of temperature distribution is assumed along the thickness direction, and this assumption remains unvaried within the entire physical domain. This approach aligns with the experimental evidence only for thin laminated structures. However, for moderately thick panels, the method is improved by solving the one-dimensional problem along the thickness direction. In other words, it is assumed that the distribution of temperature variation is unaffected by the boundaries of the structure. Another common approach is the use of two-dimensional (2D) formulations as an alternative to full three-dimensional (3D) analyses [18]. In this context, it is essential to assess the accuracy and reliability of the results. Among 2D formulations for laminated structures, the most common approaches from literature are the Equivalent Single Layer (ESL) and the Layer-Wise (LW) theories [19,20]. In the ESL theories, a kinematic model is defined for the entire laminate, with various effects analyzed by an appropriate selection of the analytical expressions for the so-called thickness functions [21]. This approach derives the governing equations for the reference surface, since a proper homogenization of the laminate is performed. In contrast, LW theories establish kinematic models on the middle surface of each lamina in the stacking sequence, ensuring the compatibility conditions at the interfaces [22]. Consequently, while ESL models allow an arbitrary selection of thickness functions, LW theories require these functions to be consistent with inter-layer kinematic compatibility [23,24]. LW formulations generally yield more accurate results due to their higher number of Degrees of Freedom (DOFs), which depend on the number of layers in the laminate. However, this accuracy corresponds to an increased computational cost, particularly for laminates with many layers. On the other hand, ESL formulations are computationally more efficient than LW, since their DOFs are fixed and do not depend on the layers, being predefined by the user. In some recent works, a hybrid approach, named Equivalent Layer-Wise (ELW), has been initially introduced for structural mechanics and has been extensively applied to multifield analysis [25]. This method ensures kinematic prescriptions at the top and bottom surfaces of the laminate through the Dirichlet boundary conditions, in addition to the well-known Neumann boundary conditions related to the secondary variables such as surface tractions, thermal fluxes, and magnetic fluxes. In this context, a key strategy is the well-known unified formulation, first developed and proposed for structural mechanics problems by Washizu [26] and Reddy [27]. This approach derives the governing equations by introducing arbitrary thickness functions and equivalent unknown variables, which serve as the DOFs of the problem. In this way, the resulting general theory is independent on the selected thickness functions, therefore the model can be enhanced by simply activating additional terms in the kinematic expansion until the convergence of results is achieved. Furthermore, this procedure embeds classical approaches such as the First-order Shear Deformation Theory (FSDT) and the Third-order Shear Deformation Theory (TSDT), widely applied in several applications and formulations over the years [28–32]. Higher-order approximations, referred to as Higher-order Shear Deformation Theories (HSDTs), are obtained by selecting more complex thickness functions. These functions can be polynomial [33,34] or non-polynomial [35,36], offering a certain flexibility and an improved accuracy for analyzing laminated structures under multifield conditions. Refs. [37,38] introduce an innovative function to simulate the slope changes in the through-the-thickness profile at each interface, known as zigzag effect. This approach has been successfully integrated with HSDTs for mechanical applications and multifield analyses, as demonstrated in Refs. [39–41], among others. In addition, Refs. [42,43] propose a refined zigzag function in the case of composite laminates, derived from the shear properties of constituent materials. Another essential consideration in multifield analysis is the evaluation of the constitutive properties of smart materials [44–46]. In fact, materials adopted in multifield analysis usually consists of two or more coexisting phases, each exhibiting an enhanced response to specific physical phenomena. Starting from the classical rule of mixtures, advanced methodologies have been developed to determine the equivalent properties of smart materials. All these approaches are based on the definition of a unit pattern within the material, called Reference Volume Element (RVE), which characterizes the geometric and physical properties of the overall material [47,48]. As reported in the milestone paper in Ref. [49], RVE in smart composites are often modelled in configurations such as laminates, cylindrical fibers, or ellipsoidal inclusions. The homogenization of smart materials is commonly performed using the Mori-Tanaka procedure [50], which delivers more accurate results than classical methods, especially for high concentrations of the constituent materials [51]. According to this methodology, a key factor is the computation of the Eshelby tensor for the RVE, which connects the strains in the heterogeneous material to that in the homogenized solid [52,53]. While this tensor is computed numerically [54–56], in case of ellipsoidal inclusions, some analytical expressions have been derived, which are widely applied in various contexts [57]. In some recent works, efforts have been made to extend analytical derivations of the Eshelby tensor to polygonal inclusions, as shown in Refs. [58,59]. The Mori-Tanaka procedure has been widely used in structural engineering to determine the equivalent properties of Carbon Nanotubes (CNTs) embedded in an isotropic matrix, accounting for the effects of fiber agglomerations and curvature [60,61]. Once the homogenized material properties are obtained for the RVE, it becomes possible to model their variation within the solid. This variation can occur, for example, due to changes in the concentration of the constituent materials or the presence of voids [62].

For complex models, a closed-form analytical solution can become a challenging issue. Even when an analytical solution is available, it is typically valid only for specific geometric and material configurations, as well as for loading and boundary conditions, as observed with methods like the Navier technique [63]. Therefore, in complex models the application of numerical procedures is required, providing approximate solutions that offer a sufficient accuracy for design purposes. The adoption of an efficient numerical method is crucial for obtaining accurate results, while minimizing the computational effort. Among numerical procedures, the Finite Element Method (FEM) has been extensively used to obtain numerical solutions in structural analysis [64–66]. The FEM-based approach involves a local approximation of the unknown variables within finite regions of the structure, known as finite elements, by using the so-called shape functions. However, this method can be computationally demanding, especially in complex applications involving singularities, curved region, mass concentrations, or cracks. In contrast, spectral collocation methods require a reduced number of DOFs by interpolating the solution at selected sample points distributed across the entire computational domain. Among these, the Generalized Differential Quadrature (GDQ) enables the numerical approximation of derivatives of arbitrary order using a quadrature formula [67–69]. A key advantage of the GDQ method is the direct approximation of derivatives, allowing for the numerical solution of fundamental equations directly in their strong form. The GDQ method has been widely applied to various structural problems, including shell structures [70–73], advanced material modelling [74,75], Functionally Graded Materials (FGMs) [76], singularities [77], and time stepping algorithms [78–80], among others. From the classical GDQ method, which employs Lagrange interpolating polynomials, it is possible to compute numerical integrations, leading to the development of the Generalized Integral Quadrature (GIQ) method [81]. Alternatively, when the Taylor series expansion is used to approximate the unknown function, the Taylor-based Generalized Integral Quadrature (T-GIQ) is applied. In this framework, analytical closed-form solutions are often used to validate numerical results under specific conditions. In fact, several attempts have been made in literature to consider different configurations when dealing with analytical solutions. Among others, the Levy solution should be mentioned for various boundary conditions modelling, as well as the boundary discontinuous method, which is widely utilized for clamped laminated structures, as detailed in Refs. [82,83]. Although analytical solutions are often effective for deriving accurate results for unknown variables, the stress and strain states, as well as gradient and flux components, may not always be physically consistent. Indeed, the use of generalized kinematic models along the thickness direction does not ensure a-priori the satisfaction of balance conditions under external loads, as highlighted in Ref. [84] for mechanical elasticity. To this end, a post-processing correction of primary and secondary variables is necessary to align results with those ones obtained from 3D simulations. This correction, known as recovery procedure, uses the GDQ to compute derivatives and to solve the balance equations [85]. An alternative approach consists in performing derivatives of in-plane quantities with the GDQ method, while GIQ is used to solve balance equations along the thickness direction. In this way, the loading conditions are perfectly satisfied, and the accuracy of 3D simulations is achieved using results derived from a 2D formulation. A review of the existing literature underscores the need for refined and efficient models capable of delivering highly accurate predictions for multifield analysis with a reduced computational effort. Furthermore, comprehensive models that incorporate all possible coupling effects among mechanical elasticity, heat transfer, mass diffusion and magnetostatics for practical engineering designs, are still lacking. Most studies focus only on some of the effects cited above. For instance, Ref. [86] presents a preliminary study on coupled thermo-mechanical modelling of laminated shell structures using higher-order theories. Similarly, Ref. [87] introduces a comprehensive ELW model, based on HSDTs, that includes electrostatic effects.

However, this model is limited in applicability to those lamination schemes for which the electrical properties of the constituent materials are known. For this reason, this paper introduces a refined 2D model, based on higher-order theories, zigzag functions, and unified formulation, for analyzing the multifield response of doubly-curved laminated panels subjected to magnetic fields, thermal conduction, and moisture diffusion. The governing equations are formulated in curvilinear principal coordinates and derived using the Master Balance principle under thermodynamic equilibrium conditions. Unlike most conventional tools, this formulation incorporates various multifield coupling effects within the constitutive model, including pyromagnetic and hygromagnetic phenomena, which are often neglected. In addition, thermal diffusion and thermophoretic effects are addressed through reciprocity relations. The model employs a continuum-based approach, with the homogenized properties of multiphase smart materials in the individual layers derived analytically using the Mori-Tanaka scheme, which employs the Eshelby tensor for the multifield case. The formulation is derived for arbitrary doubly-curved shell structures, and a semi-analytical Navier solution is applicable to specific geometries, boundary conditions, and material orientations. A post-processing recovery procedure is implemented to reconstruct the 3D distribution of unknown variables within the solid, starting from results based on the 2D model. This procedure is based on multifield balance equations, and accounts for the numerical computations of derivatives and integrals with the GDQ and GIQ, respectively. A systematic set of case studies is presented, demonstrating the accuracy of the model against more computationally expensive numerical FEM-based results. By properly activating some terms within the equations, the contributions of various multifield couplings are assessed, highlighting their influence on the overall structural response of the panel. Finally, a sensitivity analysis investigates the influence of some key governing parameters. The results of this study offer some valuable insights for practical engineering design in fields such as aerospace, mechanical engineering, health monitoring, and biomedical applications, among others, and provide a base for future theoretical and computational research on the topic.

2. Higher-order multiphysic formulation

The formulation begins with the geometric description of an arbitrary doubly-curved shell. This structure is represented in the Euclidean space as a 3D solid, defined using the parameters $(\alpha_1, \alpha_2, \zeta) \in [\alpha_1^0, \alpha_1^1] \times [\alpha_2^0, \alpha_2^1] \times [-h/2, h/2]$, where h denotes the total thickness of the shell. In line with the ELW approach [25], the position vector $\mathbf{R}(\alpha_1, \alpha_2, \zeta)$ is defined by the following relation:

$$\mathbf{R}(\alpha_1, \alpha_2, \zeta) = \mathbf{r}(\alpha_1, \alpha_2) + \frac{h}{2} z\ \mathbf{n}(\alpha_1, \alpha_2) \tag{1}$$

In the previous relation, every arbitrary point within the solid is reduced to the reference surface, denoted by $\mathbf{r}(\alpha_1, \alpha_2)$, which is positioned at the middle thickness of the shell ($\zeta = 0$). The height along the thickness direction is characterized by the dimensionless coordinate $z = 2\zeta/h$, varying in the outward normal direction $\mathbf{n}(\alpha_1, \alpha_2)$. The reference surface $\mathbf{r}$, as described in Eq. (1), is parametrized using the curvilinear principal coordinates α_1, α_2, which vary in the rectangular parametric domain $[\alpha_1^0, \alpha_1^1] \times [\alpha_2^0, \alpha_2^1]$ with $\alpha_i^0 < \alpha_i^1$ for $i = 1, 2$. In the same way, the normal unit vector $\boldsymbol{n}$ to the reference surface is defined for each point (α_1, α_2) as:

$$\mathbf{n}(\alpha_1, \alpha_2) = \frac{\mathbf{r}_{,1} \wedge \mathbf{r}_{,2}}{|\mathbf{r}_{,1} \wedge \mathbf{r}_{,2}|} \tag{2}$$

In the aforementioned equation, $\wedge$ is the well-known vector cross-product. In addition, the quantities $\mathbf{r}_{,i}$ and $\mathbf{r}_{,ij}$ with $i = 1, 2$, refer to the first-order and second-order partial derivatives of $\mathbf{r}$ with respect to α_i, $\alpha_j = \alpha_1, \alpha_2$, respectively. Other useful geometric quantities include the Lamé parameters $A_i = A_1, A_2$ and the principal radii of curvature $R_i = R_1, R_2$, both defined along $\alpha_i = \alpha_1, \alpha_2$ as follows:

$$\begin{aligned} A_i(\alpha_1, \alpha_2) &= \sqrt{\mathbf{r}_{,i} \cdot \mathbf{r}_{,i}} \\ R_i(\alpha_1, \alpha_2) &= -\frac{\mathbf{r}_{,i} \cdot \mathbf{r}_{,i}}{\mathbf{r}_{,ii} \cdot \mathbf{n}} \end{aligned} \tag{3}$$

Finally, the scaling parameters $H_i = H_1, H_2$ are introduced along the thickness direction. These parameters are defined as $H_i(\alpha_1, \alpha_2, \zeta) = 1 + \zeta/R_i$, and they are used to determine the length metrics at a given ζ, thus ensuring a proper description of the shell geometry across its thickness. The Lamé parameters in Eq. (3) are used to define the curvilinear abscissa $s_i = s_1, s_2$ of an arbitrary parametric line along the $\alpha_i = \alpha_1, \alpha_2$ principal direction. The infinitesimal variation $ds_i = A_i d\alpha_i$ is, thus, linked to the infinitesimal variation $d\alpha_i$. Then, the curvilinear abscissa s_i is determined by integrating it over the interval $[\alpha_i^0, \alpha_i]$ with $i = 1, 2$, and it varies within the interval $s_i \in [s_i^0, s_i^1]$. Finally, it is worth noting that the total thickness h of the laminate is calculated as the sum of the thicknesses h_k of each $k-$th layer in the stacking sequence.

Once the geometry of the laminated structure is defined, the multiphysic ELW model is introduced. The unknown variables for an arbitrary point in the 3D solid include the displacement field components $U_1^{(k)}, U_2^{(k)}, U_3^{(k)}$, expressed in meters $[\mathrm{m}]$ and referred to the curvilinear geometric reference system $O'\alpha_1\alpha_2\zeta$. In addition, the variation of the magnetic potential $\Delta\psi^{(k)} = \psi^{(k)} - \psi_0$ with respect to the reference value ψ_0 is expressed in ampere $[\mathrm{A}]$, the temperature variation $\Delta\mathrm{T}^{(k)} = \mathrm{T}^{(k)} - \mathrm{T}_0$ with respect to the absolute reference temperature T_0 is expressed in kelvin $[\mathrm{K}]$, and the moisture concentration variation $\Delta\mathrm{C}^{(k)} = \mathrm{C}^{(k)} - \mathrm{C}_0$ is measured with respect to the reference value C_0 in terms of moisture mass per unit volume of dry solid $[\mathrm{kg/m^3}]$. The reference variables ψ_0, $\mathrm{T}_0, \mathrm{C}_0$ correspond to a zero-stress and zero-strain configuration at any point within the solid. All these unknown variables are collected within the vector $\Delta^{(k)}$ of size 6×1, and they are expanded using the following kinematic model [25]:

$$\boldsymbol{\Delta}^{(k)} = \sum_{\tau=0}^{N+1} \mathbf{F}_\tau^{(k)} \boldsymbol{\delta}^{(\tau)} \Leftrightarrow \begin{bmatrix} U_1^{(k)} \\ U_2^{(k)} \\ U_3^{(k)} \\ \Delta\psi^{(k)} \\ \Delta\mathrm{T}^{(k)} \\ \Delta\mathrm{C}^{(k)} \end{bmatrix} = \sum_{\tau=0}^{N+1} \begin{bmatrix} F_\tau^{(k)\alpha_1} & 0 & 0 & 0 & 0 & 0 \\ 0 & F_\tau^{(k)\alpha_2} & 0 & 0 & 0 & 0 \\ 0 & 0 & F_\tau^{(k)\alpha_3} & 0 & 0 & 0 \\ 0 & 0 & 0 & F_\tau^{(k)\alpha_4} & 0 & 0 \\ 0 & 0 & 0 & 0 & F_\tau^{(k)\alpha_5} & 0 \\ 0 & 0 & 0 & 0 & 0 & F_\tau^{(k)\alpha_6} \end{bmatrix} \begin{bmatrix} u_1^{(\tau)} \\ u_2^{(\tau)} \\ u_3^{(\tau)} \\ \psi^{(\tau)} \\ \xi^{(\tau)} \\ \kappa^{(\tau)} \end{bmatrix} \tag{4}$$

In the above expression, each element of $\boldsymbol{\Delta}^{(k)}$ is expressed as the sum of $N+1$ terms. These terms consist of an arbitrary thickness function $F_\tau^{(k)\alpha_i} = F_\tau^{(k)\alpha_i}(\zeta)$ with $i = 1, \ldots, 6$, defined for each τ–th expansion order with $\tau = 0, \ldots, N+1$, which depends on the thickness coordinate ζ, and a generalized variable associated with any arbitrary (α_1, α_2) point on the reference surface. These generalized variables are grouped, for each $\tau = 0, \ldots, N+1$, into the vector $\boldsymbol{\delta}^{(\tau)}$, with size 6×1. The thickness functions introduced in Eq. (4) are defined following the ELW methodology and they are expressed in terms of dimensionless coordinate $\widetilde{z} = 2\zeta/h$ where $\widetilde{z} \in [-1, 1]$, as follows:

$$F_\tau^{(k)\alpha_i}(\widetilde{z}) = \begin{cases} \dfrac{1-\widetilde{z}}{2} & \text{for } \tau = 0 \\ J_{\tau+2}^{(\gamma,\delta)}(\widetilde{z}) - J_\tau^{(\gamma,\delta)}(\widetilde{z}) & \text{for } \tau = 1, .., N-1 \\ \dfrac{1+\widetilde{z}}{2} & \text{for } \tau = N \end{cases} \tag{5}$$

The thickness functions $F_\tau^{(k)\alpha_i}$ introduced in Eq. (5) are designed such that they are equal to 1 for $\tau = 0$ at the bottom surface, and for $\tau = N$ at the top surface. For all other expansion orders, these functions are zero at both the top and bottom surfaces. As a result, the 3D unknown variables at the top and bottom surfaces are directly related to the generalized variables associated with $\tau = 0, N$ through the following expressions:

$$\begin{aligned} \Delta_i^{(1)}\left(\alpha_1, \alpha_2, \zeta = -\frac{h}{2}\right) &= \Delta_i^{(-)} = \delta_i^{(0)}(\alpha_1, \alpha_2) \\ \Delta_i^{(l)}\left(\alpha_1, \alpha_2, \zeta = \frac{h}{2}\right) &= \Delta_i^{(+)} = \delta_i^{(N)}(\alpha_1, \alpha_2) \end{aligned} \tag{6}$$

The zigzag function corresponding to the $(N+1)$–th kinematic expansion order assumes the following expression, setting $\overline{z}_k = (\zeta - \zeta_k)/(\zeta_{k+1} - \zeta_k)$ a proper dimensionless variable:

$$F_{N+1}^{(k)\alpha_i} = \begin{cases} z_1 = -\dfrac{\zeta - \zeta_1}{\zeta_2 - \zeta_1} \\ z_k = (-1)^k \left(2\overline{z}_k - 1\right), \quad k = 2, \ldots, l-1 \\ z_l = (-1)^l \dfrac{\zeta - \zeta_{l+1}}{\zeta_{l+1} - \zeta_l} \end{cases} \tag{7}$$

The thickness function $F_{N+1}^{(k)\alpha_i}$ in Eq. (7) is zero at the top and bottom surfaces, while it becomes equal to 1 or -1 at the interfaces between adjacent layers of the laminate. For higher-order kinematic expansions with $\tau = 1, \ldots, N-1$, the thickness functions are expressed, following Eq. (5), using Jacobi polynomials $J_\tau^{(\gamma,\delta)}(\widetilde{z})$ of the τ–th order and characteristic parameters γ, δ [67]. These polynomials are computed using a recursive relation, where the characteristic parameters are set so that $A = 2\tau + \gamma + \delta - 2$, $B = A - 2$, $C = A - 1$, and $D = 2(\tau - 1)(\tau + \gamma + \delta - 1)B$:

$$J_\tau^{(\gamma,\delta)}(\widetilde{z}) = \begin{cases} 1 & \tau = 1 \\ \dfrac{1}{2}\left(2(\gamma+1) + (\gamma+\delta+2)(\widetilde{z}-1)\right) & \tau = 2 \\ \dfrac{C(AB\widetilde{z} + \gamma^2 - \delta^2)J_{\tau-1}^{(\gamma,\delta)}(\widetilde{z}) - 2(\tau+\gamma-2)(\tau+\delta-2)AJ_{\tau-2}^{(\gamma,\delta)}(\widetilde{z})}{D} & \tau = 3, \ldots N \end{cases} \tag{8}$$

The Jacobi polynomials employed in Eq. (8) include a broad family of polynomials determined the parameters γ, δ. More specifically, Lobatto polynomials are obtained by setting $\gamma = \delta = 1$, while Legendre polynomials correspond to $\gamma = \delta = 0$. Finally, from Eq. (8) the Chebyshev polynomials of the first, second, third, and fourth kinds are obtained by selecting $\gamma = \delta = -1/2, \gamma = \delta = 1/2, \gamma = -\delta = -1/2$, and $\gamma = -\delta = 1/2$, respectively. To classify the kinematic model used in each simulation, a specific nomenclature is introduced. The acronym ELDZL $-N$ is used, where "EL" signifies that the ELW approach is applied within the kinematic model, "D" indicates that displacement field components are the unknown variables, and "ZL" refers to the inclusion of the zigzag function as defined in Eq. (7). Finally, N identifies the expansion order of the kinematic model.

Having established the higher-order generalized kinematic model in Eq. (4), the ELW multifield kinematic relations are now formulated, taking into account the mechanical elasticity, magnetostatic effects, thermal conduction, and moisture diffusion equations. To this end, the 3D definition equations for a doubly-curved shell solid are introduced, using curvilinear principal coordinates $\alpha_1, \alpha_2, \zeta$. These equations relate the 3D configuration variables vector $\mathbf{\Delta}^{(k)}$ and the vector of primary variables, denoted by $\boldsymbol{\pi}^{(k)}$. Using a compact notation, this relationship can be expressed as [25]:

$$\boldsymbol{\pi}^{(k)} = \mathbf{D}\mathbf{\Delta}^{(k)} = \mathbf{D}_\zeta \mathbf{D}_\Omega \mathbf{\Delta}^{(k)} = \mathbf{D}_\zeta \sum_{i=1}^{6} \mathbf{D}_\Omega^{\alpha_i} \mathbf{\Delta}^{(k)} \tag{9}$$

where $\mathbf{D}$ is the 3D kinematic differential operator. The vector $\boldsymbol{\pi}^{(k)} = \left[\boldsymbol{\varepsilon}^{(k)T} \quad \mathscr{H}^{(k)T} \quad \widehat{\Delta \mathrm{T}}^{(k)} \widehat{\Delta \mathrm{C}}^{(k)} \boldsymbol{\theta}^{(k)T} \boldsymbol{\lambda}^{(k)T} \right]^T$ of 3D primary variables in Eq. (9) consists in the 3D strain vector $\boldsymbol{\varepsilon}^{(k)}$, the magnetic field vector $\mathscr{H}^{(k)}$, the thermal gradient vector $\boldsymbol{\theta}^{(k)}$, and the moisture concentration gradient vector $\boldsymbol{\lambda}^{(k)}$. Finally, $\widehat{\Delta \mathrm{T}}^{(k)} = \Delta \mathrm{T}^{(k)}$ and $\widehat{\Delta \mathrm{C}}^{(k)} = \Delta \mathrm{C}^{(k)}$ are conveniently introduced. These vectors can be written in their extended forms as follows:

$$\begin{aligned} \boldsymbol{\varepsilon}^{(k)} &= \left[\varepsilon_1^{(k)} \quad \varepsilon_2^{(k)} \quad \gamma_{12}^{(k)} \quad \gamma_{13}^{(k)} \quad \gamma_{23}^{(k)} \quad \varepsilon_3^{(k)} \right]^T \\ \mathscr{H}^{(k)} &= \left[\mathscr{H}_1^{(k)} \quad \mathscr{H}_2^{(k)} \quad \mathscr{H}_3^{(k)} \right]^T \\ \boldsymbol{\theta}^{(k)} &= \left[\theta_1^{(k)} \quad \theta_2^{(k)} \quad \theta_3^{(k)} \right]^T \\ \boldsymbol{\lambda}^{(k)} &= \left[\lambda_1^{(k)} \quad \lambda_2^{(k)} \quad \lambda_3^{(k)} \right]^T \end{aligned} \tag{10}$$

It should be noted that in Eq. (9), the differential operator $\mathbf{D}$ is expressed as the product of the operators $\mathbf{D}_\zeta$ and $\mathbf{D}_\Omega$, where $\mathbf{D}_\zeta$ contains the terms with derivatives with respect to ζ coordinate, and $\mathbf{D}_\Omega$ includes derivatives along α_1, α_2 principal directions. The operator $\mathbf{D}_\zeta$ is expressed as the sum of the operators $\mathbf{D}_\Omega^{\alpha_i}$ with $i = 1, \dots, 6$, as follows [25]:

$$\mathbf{D}_\Omega = \sum_{i=1}^{6} \mathbf{D}_\Omega^{\alpha_i} = \begin{bmatrix} \mathbf{D}_{\Omega(1)} & \mathbf{0} & \mathbf{0} & \mathbf{0} \\ \mathbf{0} & \mathbf{D}_{\Omega(2)} & \mathbf{0} & \mathbf{0} \\ \mathbf{0} & \mathbf{0} & \mathbf{D}_{\Omega(3)} & \mathbf{0} \\ \mathbf{0} & \mathbf{0} & \mathbf{0} & \mathbf{D}_{\Omega(3)} \\ \mathbf{0} & \mathbf{0} & \mathbf{D}_{\Omega(2)} & \mathbf{0} \\ \mathbf{0} & \mathbf{0} & \mathbf{0} & \mathbf{D}_{\Omega(2)} \end{bmatrix} \tag{11}$$

The terms $\mathbf{D}_{\Omega(1)}, \mathbf{D}_{\Omega(2)}$ and $\mathbf{D}_{\Omega(3)}$ assume the following extended form:

$$\begin{aligned} \mathbf{D}_{\Omega(1)} &= \left[\overline{\mathbf{D}}_\Omega^{\alpha_1} \quad \overline{\mathbf{D}}_\Omega^{\alpha_2} \quad \overline{\mathbf{D}}_\Omega^{\alpha_3} \right] \\ \mathbf{D}_{\Omega(2)} &= \left[-\frac{1}{A_1}\frac{\partial}{\partial \alpha_1} \quad -\frac{1}{A_2}\frac{\partial}{\partial \alpha_2} \quad -1 \right]^T \\ \mathbf{D}_{\Omega(3)} &= 1 \end{aligned} \tag{12}$$

where

$$\overline{\mathbf{D}}_\Omega^{\alpha_1} = \begin{bmatrix} \frac{1}{A_1}\frac{\partial}{\partial \alpha_1} \\ \frac{1}{A_1 A_2}\frac{\partial A_2}{\partial \alpha_1} \\ -\frac{1}{A_1 A_2}\frac{\partial A_1}{\partial \alpha_2} \\ \frac{1}{A_2}\frac{\partial}{\partial \alpha_2} \\ -\frac{1}{R_1} \\ 0 \\ 1 \\ 0 \\ 0 \end{bmatrix}, \quad \overline{\mathbf{D}}_\Omega^{\alpha_2} = \begin{bmatrix} \frac{1}{A_1 A_2}\frac{\partial A_1}{\partial \alpha_2} \\ \frac{1}{A_2}\frac{\partial}{\partial \alpha_2} \\ \frac{1}{A_1}\frac{\partial}{\partial \alpha_1} \\ -\frac{1}{A_1 A_2}\frac{\partial A_2}{\partial \alpha_1} \\ 0 \\ -\frac{1}{R_2} \\ 0 \\ 1 \\ 0 \end{bmatrix}, \quad \overline{\mathbf{D}}_\Omega^{\alpha_3} = \begin{bmatrix} \frac{1}{R_1} \\ \frac{1}{R_2} \\ 0 \\ 0 \\ \frac{1}{A_1}\frac{\partial}{\partial \alpha_1} \\ \frac{1}{A_2}\frac{\partial}{\partial \alpha_2} \\ 0 \\ 0 \\ 1 \end{bmatrix} \tag{13}$$

Finally, the operator $\mathbf{D}_\zeta$ is expressed as:

$$\mathbf{D}_\zeta = \begin{bmatrix} \mathbf{D}_{\zeta(1)} & \mathbf{0} & \mathbf{0} & \mathbf{0} & \mathbf{0} & \mathbf{0} \\ \mathbf{0} & \mathbf{D}_{\zeta(2)} & \mathbf{0} & \mathbf{0} & \mathbf{0} & \mathbf{0} \\ \mathbf{0} & \mathbf{0} & \mathbf{D}_{\zeta(3)} & 0 & \mathbf{0} & \mathbf{0} \\ \mathbf{0} & \mathbf{0} & 0 & \mathbf{D}_{\zeta(3)} & \mathbf{0} & \mathbf{0} \\ \mathbf{0} & \mathbf{0} & \mathbf{0} & \mathbf{0} & \mathbf{D}_{\zeta(2)} & \mathbf{0} \\ \mathbf{0} & \mathbf{0} & \mathbf{0} & \mathbf{0} & \mathbf{0} & \mathbf{D}_{\zeta(2)} \end{bmatrix} \tag{14}$$

The sub-matrices $\mathbf{D}_{\zeta(1)}, \mathbf{D}_{\zeta(2)}$ and $\mathbf{D}_{\zeta(3)}$ are reported below in expanded form [25]:

$$\mathbf{D}_{\zeta(1)} = \begin{bmatrix} \frac{1}{H_1} & 0 & 0 & 0 & 0 & 0 & 0 & 0 & 0 \\ 0 & \frac{1}{H_2} & 0 & 0 & 0 & 0 & 0 & 0 & 0 \\ 0 & 0 & \frac{1}{H_1} & \frac{1}{H_2} & 0 & 0 & 0 & 0 & 0 \\ 0 & 0 & 0 & 0 & \frac{1}{H_1} & 0 & \frac{\partial}{\partial \zeta} & 0 & 0 \\ 0 & 0 & 0 & 0 & 0 & \frac{1}{H_2} & 0 & \frac{\partial}{\partial \zeta} & 0 \\ 0 & 0 & 0 & 0 & 0 & 0 & 0 & 0 & \frac{\partial}{\partial \zeta} \end{bmatrix}$$

$$\mathbf{D}_{\zeta(2)} = \begin{bmatrix} \frac{1}{H_1} & 0 & 0 \\ 0 & \frac{1}{H_2} & 0 \\ 0 & 0 & \frac{\partial}{\partial \zeta} \end{bmatrix}, \quad \mathbf{D}_{\zeta(3)} = 1 \tag{15}$$

The introduction of the generalized kinematic model from Eq. (4) into the 3D definition equations (9) results in the introduction of the generalized definition operator $\mathbf{Z}^{(k\tau)\alpha_i}$ for each $\tau-$th kinematic expansion order, with $\tau = 0, \dots, N+1$ and $i = 1, \dots, 6$, varying in each point of the 3D doubly-curved solid. This matrix is defined as follows [25]:

$$\mathbf{Z}^{(k\tau)\alpha_i} = \begin{bmatrix} \mathbf{Z}_1^{(k\tau)\alpha_i} & \mathbf{0} & \mathbf{0} & \mathbf{0} & \mathbf{0} & \mathbf{0} \\ \mathbf{0} & \mathbf{Z}_2^{(k\tau)\alpha_i} & \mathbf{0} & \mathbf{0} & \mathbf{0} & \mathbf{0} \\ \mathbf{0} & \mathbf{0} & \mathbf{Z}_3^{(k\tau)\alpha_i} & \mathbf{0} & \mathbf{0} & \mathbf{0} \\ \mathbf{0} & \mathbf{0} & \mathbf{0} & \mathbf{Z}_3^{(k\tau)\alpha_i} & \mathbf{0} & \mathbf{0} \\ \mathbf{0} & \mathbf{0} & \mathbf{0} & \mathbf{0} & \mathbf{Z}_2^{(k\tau)\alpha_i} & \mathbf{0} \\ \mathbf{0} & \mathbf{0} & \mathbf{0} & \mathbf{0} & \mathbf{0} & \mathbf{Z}_2^{(k\tau)\alpha_i} \end{bmatrix} \tag{16}$$

The sub-matrices $\mathbf{Z}_m^{(k\tau)\alpha_i} = \mathbf{Z}_1^{(k\tau)\alpha_i}, \mathbf{Z}_2^{(k\tau)\alpha_i}, \mathbf{Z}_3^{(k\tau)\alpha_i}$ introduced in Eq. (16) take the following form:

$$\mathbf{Z}_m^{(k\tau)\alpha_i} = \mathbf{D}_{\zeta(m)} F_\tau^{(k)\alpha_i} \tag{17}$$

for $m = 1,2,3$. In this way, the kinematic definition equations are provided for the higher-order ELW model, according to the relations reported below [25]:

$$\boldsymbol{\pi}^{(k)} = \mathbf{D}_\zeta \sum_{i=1}^{6} \mathbf{D}_\Omega^{\alpha_i} \boldsymbol{\Delta}^{(k)} = \sum_{\tau=0}^{N+1} \sum_{i=1}^{6} \mathbf{Z}^{(k\tau)\alpha_i} \mathbf{D}_\Omega^{\alpha_i} \boldsymbol{\delta}^{(\tau)} = \sum_{\tau=0}^{N+1} \sum_{i=1}^{6} \mathbf{Z}^{(k\tau)\alpha_i} \boldsymbol{\pi}^{(\tau)\alpha_i} \tag{18}$$

In the previous equation, the vector $\boldsymbol{\pi}^{(\tau)\alpha_i} = \mathbf{D}_\Omega^{\alpha_i} \boldsymbol{\delta}^{(\tau)}$ of generalized primary variables is introduced for an arbitrary $\tau = 0,\ldots,N+1$. In line with the 3D vector $\boldsymbol{\pi}^{(k)}$ of primary variables, the vector $\boldsymbol{\pi}^{(\tau)\alpha_i} = \left[\boldsymbol{\varepsilon}^{(\tau)\alpha_i T} \quad \boldsymbol{\mathscr{H}}^{(\tau)\alpha_i T} \quad \widehat{\Delta \mathrm{T}}^{(\tau)\alpha_i} \widehat{\Delta \mathrm{C}}^{(\tau)\alpha_i} \boldsymbol{\theta}^{(\tau)\alpha_i T} \boldsymbol{\lambda}^{(\tau)\alpha_i T} \right]^T$ contains the vectors of the generalized primary variables for each physical problem within the present formulation. The sub-vectors $\boldsymbol{\varepsilon}^{(\tau)\alpha_i}$, $\boldsymbol{\mathscr{H}}^{(\tau)\alpha_i}$, $\widehat{\Delta \mathrm{T}}^{(\tau)\alpha_i}$, $\widehat{\Delta \mathrm{C}}^{(\tau)\alpha_i}$, $\boldsymbol{\theta}^{(\tau)\alpha_i}$ and $\boldsymbol{\lambda}^{(\tau)\alpha_i}$ take the following extended form:

$$\begin{gathered} \boldsymbol{\varepsilon}^{(\tau)\alpha_i}(\alpha_1,\alpha_2) = \left[\varepsilon_1^{(\tau)\alpha_i} \quad \varepsilon_2^{(\tau)\alpha_i} \quad \gamma_1^{(\tau)\alpha_i} \quad \gamma_2^{(\tau)\alpha_i} \quad \gamma_{13}^{(\tau)\alpha_i} \quad \gamma_{23}^{(\tau)\alpha_i} \quad \omega_{13}^{(\tau)\alpha_i} \quad \omega_{23}^{(\tau)\alpha_i} \quad \varepsilon_3^{(\tau)\alpha_i} \right]^T \\ \boldsymbol{\mathscr{H}}^{(\tau)\alpha_i}(\alpha_1,\alpha_2) = \left[\mathscr{H}_1^{(\tau)\alpha_i} \quad \mathscr{H}_2^{(\tau)\alpha_i} \quad \mathscr{H}_3^{(\tau)\alpha_i} \right]^T \\ \widehat{\Delta \mathrm{T}}^{(\tau)\alpha_i}(\alpha_1,\alpha_2) = \widehat{\Delta \mathrm{T}}^{(\tau)\alpha_i}, \quad \widehat{\Delta \mathrm{C}}^{(\tau)\alpha_i}(\alpha_1,\alpha_2) = \widehat{\Delta \mathrm{C}}^{(\tau)\alpha_i} \\ \boldsymbol{\theta}^{(\tau)\alpha_i}(\alpha_1,\alpha_2) = \left[\theta_1^{(\tau)\alpha_i} \quad \theta_2^{(\tau)\alpha_i} \quad \theta_3^{(\tau)\alpha_i} \right]^T, \quad \boldsymbol{\lambda}^{(\tau)\alpha_i}(\alpha_1,\alpha_2) = \left[\lambda_1^{(\tau)\alpha_i} \quad \lambda_2^{(\tau)\alpha_i} \quad \lambda_3^{(\tau)\alpha_i} \right]^T \end{gathered} \tag{19}$$

Once the kinematic relations for the higher-order multifield formulation are presented, the coupled constitutive equations are introduced. To this end, the hygro-thermo-magneto-elastic constitutive relations are introduced for a 3D solid. These relations allow one to express the 3D secondary variables, collected into the vector $\boldsymbol{\chi}^{(k)}$, in terms of the vector $\boldsymbol{\pi}^{(k)}$ of 3D primary variables within an arbitrary $k-$th layer [25]:

$$\boldsymbol{\chi}^{(k)} = \overline{\boldsymbol{\Gamma}}^{(k)} \boldsymbol{\pi}^{(k)} \Leftrightarrow \begin{bmatrix} \boldsymbol{\sigma}^{(k)} \\ \boldsymbol{\mathscr{B}}^{(k)} \\ \eta^{(k)} \\ \mu^{(k)} \\ \mathbf{h}^{(k)} \\ \mathbf{c}^{(k)} \end{bmatrix} = \begin{bmatrix} \overline{\boldsymbol{\Gamma}}_{\mathrm{C}}^{(k)} & -\overline{\boldsymbol{\Gamma}}_{\mathrm{Q}}^{(k)T} & -\overline{\boldsymbol{\Gamma}}_{z}^{(k)T} & -\overline{\boldsymbol{\Gamma}}_{e}^{(k)T} & \mathbf{0} & \mathbf{0} \\ \overline{\boldsymbol{\Gamma}}_{\mathrm{Q}}^{(k)} & \overline{\boldsymbol{\Gamma}}_{\mathrm{M}}^{(k)} & \overline{\boldsymbol{\Gamma}}_{\mathrm{w}}^{(k)T} & \overline{\boldsymbol{\Gamma}}_{\mathrm{f}}^{(k)T} & \mathbf{0} & \mathbf{0} \\ \overline{\boldsymbol{\Gamma}}_{z}^{(k)} & \overline{\boldsymbol{\Gamma}}_{\mathrm{w}}^{(k)} & \overline{\boldsymbol{\Gamma}}_{\mathrm{TT}}^{(k)} & \overline{\boldsymbol{\Gamma}}_{\mathrm{TC}}^{(k)} & \mathbf{0} & \mathbf{0} \\ \overline{\boldsymbol{\Gamma}}_{e}^{(k)} & \overline{\boldsymbol{\Gamma}}_{\mathrm{f}}^{(k)} & \overline{\boldsymbol{\Gamma}}_{\mathrm{TC}}^{(k)} & \overline{\boldsymbol{\Gamma}}_{\mathrm{CC}}^{(k)} & \mathbf{0} & \mathbf{0} \\ \mathbf{0} & \mathbf{0} & \mathbf{0} & \mathbf{0} & \overline{\boldsymbol{\Gamma}}_{\mathrm{K}}^{(k)} & \overline{\boldsymbol{\Gamma}}_{\mathrm{Y}}^{(k)} \\ \mathbf{0} & \mathbf{0} & \mathbf{0} & \mathbf{0} & \overline{\boldsymbol{\Gamma}}_{\mathrm{X}}^{(k)} & \overline{\boldsymbol{\Gamma}}_{\mathrm{S}}^{(k)} \end{bmatrix} \begin{bmatrix} \boldsymbol{\varepsilon}^{(k)} \\ \boldsymbol{\mathscr{H}}^{(k)} \\ \widehat{\Delta \mathrm{T}}^{(k)} \\ \widehat{\Delta \mathrm{C}}^{(k)} \\ \boldsymbol{\theta}^{(k)} \\ \boldsymbol{\lambda}^{(k)} \end{bmatrix} \tag{20}$$

As can be seen, the constitutive relation (20) introduces the complete coupling between the primary and secondary variables of the multifield problem. In particular, the secondary variables are collected within various sub-vectors, namely the stress vector $\boldsymbol{\sigma}^{(k)} = \left[\sigma_1^{(k)} \quad \sigma_2^{(k)} \quad \tau_{12}^{(k)} \quad \tau_{13}^{(k)} \quad \tau_{23}^{(k)} \quad \sigma_3^{(k)} \right]^T$, the magnetic flux vector $\boldsymbol{\mathscr{B}}^{(k)} = \left[\mathscr{B}_1^{(k)} \quad \mathscr{B}_2^{(k)} \quad \mathscr{B}_3^{(k)} \right]^T$, as well as the thermal flux vector $\mathbf{h}^{(k)} = \left[h_1^{(k)} \quad h_2^{(k)} \quad h_3^{(k)} \right]^T$ and the moisture flux vector $\mathbf{c}^{(k)} = \left[c_1^{(k)} \quad c_2^{(k)} \quad c_3^{(k)} \right]^T$. Furthermore, two scalar quantities are introduced: the specific entropy $\eta^{(k)}$ and the chemical potential $\mu^{(k)}$. The constitutive sub-matrices of Eq. (20) are taken from Ref. [25] and are reported below in extended form:

$$\overline{\boldsymbol{\Gamma}}_{\mathrm{C}}^{(k)} = \begin{bmatrix} \overline{C}_{11}^{(k)} & \overline{C}_{12}^{(k)} & \overline{C}_{16}^{(k)} & \overline{C}_{14}^{(k)} & \overline{C}_{15}^{(k)} & \overline{C}_{13}^{(k)} \\ \overline{C}_{12}^{(k)} & \overline{C}_{22}^{(k)} & \overline{C}_{26}^{(k)} & \overline{C}_{24}^{(k)} & \overline{C}_{25}^{(k)} & \overline{C}_{23}^{(k)} \\ \overline{C}_{16}^{(k)} & \overline{C}_{26}^{(k)} & \overline{C}_{66}^{(k)} & \overline{C}_{46}^{(k)} & \overline{C}_{56}^{(k)} & \overline{C}_{36}^{(k)} \\ \overline{C}_{14}^{(k)} & \overline{C}_{24}^{(k)} & \overline{C}_{46}^{(k)} & \overline{C}_{44}^{(k)} & \overline{C}_{45}^{(k)} & \overline{C}_{34}^{(k)} \\ \overline{C}_{15}^{(k)} & \overline{C}_{25}^{(k)} & \overline{C}_{56}^{(k)} & \overline{C}_{45}^{(k)} & \overline{C}_{55}^{(k)} & \overline{C}_{35}^{(k)} \\ \overline{C}_{13}^{(k)} & \overline{C}_{23}^{(k)} & \overline{C}_{36}^{(k)} & \overline{C}_{34}^{(k)} & \overline{C}_{35}^{(k)} & \overline{C}_{33}^{(k)} \end{bmatrix}$$

$$\overline{\boldsymbol{\Gamma}}_{\mathrm{M}}^{(k)} = \begin{bmatrix} \overline{m}_{11}^{(k)} & \overline{m}_{12}^{(k)} & \overline{m}_{13}^{(k)} \\ \overline{m}_{12}^{(k)} & \overline{m}_{22}^{(k)} & \overline{m}_{23}^{(k)} \\ \overline{m}_{13}^{(k)} & \overline{m}_{23}^{(k)} & \overline{m}_{33}^{(k)} \end{bmatrix}$$

$$\overline{\boldsymbol{\Gamma}}_{\mathrm{Q}}^{(k)} = \begin{bmatrix} \overline{q}_{11}^{(k)} & \overline{q}_{12}^{(k)} & \overline{q}_{16}^{(k)} & \overline{q}_{14}^{(k)} & \overline{q}_{15}^{(k)} & \overline{q}_{13}^{(k)} \\ \overline{q}_{21}^{(k)} & \overline{q}_{22}^{(k)} & \overline{q}_{26}^{(k)} & \overline{q}_{24}^{(k)} & \overline{q}_{25}^{(k)} & \overline{q}_{23}^{(k)} \\ \overline{q}_{31}^{(k)} & \overline{q}_{32}^{(k)} & \overline{q}_{36}^{(k)} & \overline{q}_{34}^{(k)} & \overline{q}_{35}^{(k)} & \overline{q}_{33}^{(k)} \end{bmatrix}$$

$$\overline{\boldsymbol{\Gamma}}_{\mathrm{z}}^{(k)} = \begin{bmatrix} \overline{z}_{11}^{(k)} & \overline{z}_{22}^{(k)} & \overline{z}_{12}^{(k)} & \overline{z}_{13}^{(k)} & \overline{z}_{23}^{(k)} & \overline{z}_{33}^{(k)} \end{bmatrix}$$

$$\overline{\boldsymbol{\Gamma}}_{\mathrm{e}}^{(k)} = \begin{bmatrix} \overline{e}_{11}^{(k)} & \overline{e}_{22}^{(k)} & \overline{e}_{12}^{(k)} & \overline{e}_{13}^{(k)} & \overline{e}_{23}^{(k)} & \overline{e}_{33}^{(k)} \end{bmatrix}$$

$$\overline{\boldsymbol{\Gamma}}_{\mathrm{w}}^{(k)} = \begin{bmatrix} \overline{w}_{11}^{(k)} & \overline{w}_{22}^{(k)} & \overline{w}_{33}^{(k)} \end{bmatrix} \overline{\boldsymbol{\Gamma}}_{\mathrm{f}}^{(k)} = \begin{bmatrix} \overline{f}_{11}^{(k)} & \overline{f}_{22}^{(k)} & \overline{f}_{33}^{(k)} \end{bmatrix}$$

$$\overline{\boldsymbol{\Gamma}}_{\mathrm{K}}^{(k)} = \begin{bmatrix} \overline{k}_{11}^{(k)} & \overline{k}_{12}^{(k)} & \overline{k}_{13}^{(k)} \\ \overline{k}_{12}^{(k)} & \overline{k}_{22}^{(k)} & \overline{k}_{23}^{(k)} \\ \overline{k}_{13}^{(k)} & \overline{k}_{23}^{(k)} & \overline{k}_{33}^{(k)} \end{bmatrix}, \quad \overline{\boldsymbol{\Gamma}}_{\mathrm{X}}^{(k)} = \begin{bmatrix} \overline{x}_{11}^{(k)} & \overline{x}_{12}^{(k)} & \overline{x}_{13}^{(k)} \\ \overline{x}_{12}^{(k)} & \overline{x}_{22}^{(k)} & \overline{x}_{23}^{(k)} \\ \overline{x}_{13}^{(k)} & \overline{x}_{23}^{(k)} & \overline{x}_{33}^{(k)} \end{bmatrix}$$

$$\overline{\boldsymbol{\Gamma}}_{\mathrm{Y}}^{(k)} = \begin{bmatrix} \overline{y}_{11}^{(k)} & \overline{y}_{12}^{(k)} & \overline{y}_{13}^{(k)} \\ \overline{y}_{12}^{(k)} & \overline{y}_{22}^{(k)} & \overline{y}_{23}^{(k)} \\ \overline{y}_{13}^{(k)} & \overline{y}_{23}^{(k)} & \overline{y}_{33}^{(k)} \end{bmatrix}, \quad \overline{\boldsymbol{\Gamma}}_{\mathrm{S}}^{(k)} = \begin{bmatrix} \overline{s}_{11}^{(k)} & \overline{s}_{12}^{(k)} & \overline{s}_{13}^{(k)} \\ \overline{s}_{12}^{(k)} & \overline{s}_{22}^{(k)} & \overline{s}_{23}^{(k)} \\ \overline{s}_{13}^{(k)} & \overline{s}_{23}^{(k)} & \overline{s}_{33}^{(k)} \end{bmatrix}$$

$$\overline{\boldsymbol{\Gamma}}_{\mathrm{TT}}^{(k)} = \overline{\xi}_{11}^{(k)}, \quad \overline{\boldsymbol{\Gamma}}_{\mathrm{TC}}^{(k)} = \overline{\xi}_{12}^{(k)}, \quad \overline{\boldsymbol{\Gamma}}_{\mathrm{CC}}^{(k)} = \overline{\xi}_{22}^{(k)} \tag{21}$$

The vectors $\overline{\boldsymbol{\Gamma}}_{\mathrm{z}}^{(k)}$ and $\overline{\boldsymbol{\Gamma}}_{\mathrm{e}}^{(k)}$ account for the additional strains induced by temperature variation and moisture concentration within the 3D solid. These quantities are expressed in terms of elastic stiffness matrix $\overline{\boldsymbol{\Gamma}}_{\mathrm{C}}^{(k)}$ by introducing the vectors $\overline{\boldsymbol{\Gamma}}_{\mathrm{a}}^{(k)} = \begin{bmatrix} \overline{a}_{11}^{(k)} & \overline{a}_{22}^{(k)} & \overline{a}_{12}^{(k)} & \overline{a}_{13}^{(k)} & \overline{a}_{23}^{(k)} & \overline{a}_{33}^{(k)} \end{bmatrix}^T$ and $\overline{\boldsymbol{\Gamma}}_{\mathrm{b}}^{(k)} = \begin{bmatrix} \overline{b}_{11}^{(k)} & \overline{b}_{22}^{(k)} & \overline{b}_{12}^{(k)} & \overline{b}_{13}^{(k)} & \overline{b}_{23}^{(k)} & \overline{b}_{33}^{(k)} \end{bmatrix}^T$ of size 6×1, which represent the rotated thermal expansion coefficients and hygroscopic expansion coefficients, respectively, denoted by $\overline{a}_{ij}^{(k)}$ and $\overline{b}_{ij}^{(k)}$ for $i,j = 1,\dots,3$ [25]:

$$\overline{\boldsymbol{\Gamma}}_{\mathrm{z}}^{(k)T} = \overline{\boldsymbol{\Gamma}}_{\mathrm{C}}^{(k)} \overline{\boldsymbol{\Gamma}}_{\mathrm{a}}^{(k)}, \quad \overline{\boldsymbol{\Gamma}}_{\mathrm{e}}^{(k)T} = \overline{\boldsymbol{\Gamma}}_{\mathrm{C}}^{(k)} \overline{\boldsymbol{\Gamma}}_{\mathrm{b}}^{(k)} \tag{22}$$

The constitutive relation in Eq. (20) is referred to the geometric reference system of the 3D shell solid, as discussed in Eq. (1). This relation is obtained by applying a proper transformation, within each $k-$th layer, to the constitutive relation expressed in the material reference system $O'\widehat{\alpha}_1^{(k)}\widehat{\alpha}_2^{(k)}\widehat{\zeta}^{(k)}$. This relationship is presented as follows:

$$\hat{\boldsymbol{\chi}}^{(k)} = \boldsymbol{\Gamma}^{(k)} \hat{\boldsymbol{\pi}}^{(k)} \quad \Leftrightarrow \quad \begin{bmatrix} \hat{\boldsymbol{\sigma}}^{(k)} \\ \hat{\boldsymbol{\mathcal{B}}}^{(k)} \\ \eta^{(k)} \\ \mu^{(k)} \\ \hat{\mathbf{h}}^{(k)} \\ \hat{\mathbf{c}}^{(k)} \end{bmatrix} = \begin{bmatrix} \boldsymbol{\Gamma}_{\mathrm{C}}^{(k)} & -\boldsymbol{\Gamma}_{\mathrm{Q}}^{(k)T} & -\boldsymbol{\Gamma}_{z}^{(k)T} & -\boldsymbol{\Gamma}_{e}^{(k)T} & \mathbf{0} & \mathbf{0} \\ \boldsymbol{\Gamma}_{\mathrm{Q}}^{(k)} & \boldsymbol{\Gamma}_{\mathrm{M}}^{(k)} & \boldsymbol{\Gamma}_{\mathrm{w}}^{(k)T} & \boldsymbol{\Gamma}_{f}^{(k)T} & \mathbf{0} & \mathbf{0} \\ \boldsymbol{\Gamma}_{z}^{(k)} & \boldsymbol{\Gamma}_{\mathrm{w}}^{(k)} & \boldsymbol{\Gamma}_{\mathrm{TT}}^{(k)} & \boldsymbol{\Gamma}_{\mathrm{TC}}^{(k)} & \mathbf{0} & \mathbf{0} \\ \boldsymbol{\Gamma}_{e}^{(k)} & \boldsymbol{\Gamma}_{f}^{(k)} & \boldsymbol{\Gamma}_{\mathrm{TC}}^{(k)} & \boldsymbol{\Gamma}_{\mathrm{CC}}^{(k)} & \mathbf{0} & \mathbf{0} \\ \mathbf{0} & \mathbf{0} & \mathbf{0} & \mathbf{0} & \boldsymbol{\Gamma}_{\mathrm{K}}^{(k)} & \boldsymbol{\Gamma}_{\mathrm{Y}}^{(k)} \\ \mathbf{0} & \mathbf{0} & \mathbf{0} & \mathbf{0} & \boldsymbol{\Gamma}_{\mathrm{X}}^{(k)} & \boldsymbol{\Gamma}_{\mathrm{S}}^{(k)} \end{bmatrix} \begin{bmatrix} \hat{\boldsymbol{\varepsilon}}^{(k)} \\ \hat{\boldsymbol{\mathcal{H}}}^{(k)} \\ \widehat{\Delta \mathrm{T}}^{(k)} \\ \widehat{\Delta \mathrm{C}}^{(k)} \\ \hat{\boldsymbol{\theta}}^{(k)} \\ \hat{\boldsymbol{\lambda}}^{(k)} \end{bmatrix} \tag{23}$$

In this case, the vectors of primary and secondary variables in the material reference system, $\widehat{\boldsymbol{\pi}}^{(k)}$ and $\widehat{\boldsymbol{\chi}}^{(k)}$, are associated with the 3D multifield constitutive matrix $\boldsymbol{\Gamma}^{(k)}$. The transformation from the material to the geometric reference system is carried out by defining an orthogonal transformation matrix $\mathbf{H}^{(k)}$. If the parallelism between the $\widehat{\alpha}_1^{(k)} - \widehat{\alpha}_2^{(k)}$ and $\alpha_1 - \alpha_2$ planes for an arbitrary $k = 1,\dots,l$ is assumed, this matrix depends on the angle $\vartheta^{(k)}$ between $\widehat{\alpha}_1^{(k)}$ and α_1 axes. In this case, the matrix $\mathbf{H}^{(k)}$ takes the following form [25]:

$$\mathbf{H}^{(k)} = \begin{bmatrix} \cos\vartheta^{(k)} & \sin\vartheta^{(k)} & 0 \\ -\sin\vartheta^{(k)} & \cos\vartheta^{(k)} & 0 \\ 0 & 0 & 1 \end{bmatrix} \tag{24}$$

The transformation of the 3D matrix $\boldsymbol{\Gamma}^{(k)}$ is carried out by introducing, in addition to the matrix $\mathbf{H}^{(k)}$ from Eq. (24), the matrix $\mathbf{T}^{(k)}$ of size 6×6, via the Kronecker product $\otimes$, as reported below:

$$\begin{aligned} \mathbf{T}^{(k)} &= \overline{\mathbf{T}}^{(k)}_{([1,5,4,7,8,9]\times[1,5,2+4,3+7,6+8,9])} \\ &= \left(\mathbf{H}^{(k)T} \otimes \left(\mathbf{H}^{(k)} \right)^{-1} \right)_{([1,5,4,7,8,9]\times[1,5,2+4,3+7,6+8,9])} \end{aligned} \tag{25}$$

In this way, the matrix $\overline{\boldsymbol{\Gamma}}^{(k)}$ is derived from Eq. (23) as follows:

$$\overline{\boldsymbol{\Gamma}}^{(k)} = \begin{bmatrix} \mathbf{T}^{(k)}\boldsymbol{\Gamma}_{\mathrm{C}}^{(k)}\mathbf{T}^{(k)T} & -\mathbf{T}^{(k)}\boldsymbol{\Gamma}_{\mathrm{Q}}^{(k)T}\mathbf{H}^{(k)} & -\mathbf{T}^{(k)}\boldsymbol{\Gamma}_{\mathrm{C}}^{(k)}\mathbf{T}^{(k)T}\overline{\boldsymbol{\Gamma}}_{\mathrm{a}}^{(k)} & -\mathbf{T}^{(k)}\boldsymbol{\Gamma}_{\mathrm{C}}^{(k)}\mathbf{T}^{(k)T}\overline{\boldsymbol{\Gamma}}_{\mathrm{b}}^{(k)} & \mathbf{0} & \mathbf{0} \\ \mathbf{H}^{(k)T}\boldsymbol{\Gamma}_{\mathrm{Q}}^{(k)}\mathbf{T}^{(k)T} & \mathbf{H}^{(k)T}\boldsymbol{\Gamma}_{\mathrm{M}}^{(k)}\mathbf{H}^{(k)} & \mathbf{H}^{(k)T}\boldsymbol{\Gamma}_{\mathrm{w}}^{(k)T} & \mathbf{H}^{(k)T}\boldsymbol{\Gamma}_{\mathrm{f}}^{(k)T} & \mathbf{0} & \mathbf{0} \\ \overline{\boldsymbol{\Gamma}}_{\mathrm{a}}^{(k)T}\mathbf{T}^{(k)T}\boldsymbol{\Gamma}_{\mathrm{C}}^{(k)}\mathbf{T}^{(k)} & \boldsymbol{\Gamma}_{\mathrm{w}}^{(k)}\mathbf{H}^{(k)} & \boldsymbol{\Gamma}_{\mathrm{TT}}^{(k)} & \boldsymbol{\Gamma}_{\mathrm{TC}}^{(k)} & \mathbf{0} & \mathbf{0} \\ \overline{\boldsymbol{\Gamma}}_{\mathrm{b}}^{(k)T}\mathbf{T}^{(k)T}\boldsymbol{\Gamma}_{\mathrm{C}}^{(k)}\mathbf{T}^{(k)} & \boldsymbol{\Gamma}_{\mathrm{f}}^{(k)}\mathbf{H}^{(k)} & \boldsymbol{\Gamma}_{\mathrm{TC}}^{(k)} & \boldsymbol{\Gamma}_{\mathrm{CC}}^{(k)} & \mathbf{0} & \mathbf{0} \\ \mathbf{0} & \mathbf{0} & \mathbf{0} & \mathbf{0} & \mathbf{H}^{(k)T}\boldsymbol{\Gamma}_{\mathrm{K}}^{(k)}\mathbf{H}^{(k)} & \mathbf{H}^{(k)T}\boldsymbol{\Gamma}_{\mathrm{Y}}^{(k)}\mathbf{H}^{(k)} \\ \mathbf{0} & \mathbf{0} & \mathbf{0} & \mathbf{0} & \mathbf{H}^{(k)T}\boldsymbol{\Gamma}_{\mathrm{X}}^{(k)}\mathbf{H}^{(k)} & \mathbf{H}^{(k)T}\boldsymbol{\Gamma}_{\mathrm{S}}^{(k)}\mathbf{H}^{(k)} \end{bmatrix} \tag{26}$$

As seen in Eq. (23), the matrices $\boldsymbol{\Gamma}_{\mathrm{Y}}^{(k)}$ and $\boldsymbol{\Gamma}_{\mathrm{X}}^{(k)}$ couple the Fick equations for mass diffusion with the Fourier equations for heat conduction. These matrices can be expressed in terms of the thermal conductivity matrix $\boldsymbol{\Gamma}_{\mathrm{K}}^{(k)}$ and the diffusivity matrix $\boldsymbol{\Gamma}_{\mathrm{S}}^{(k)}$, derived from the Onsager reciprocity relations. To this end, the coupling coefficients $\lambda^{(k)}$ and $\nu^{(k)}$ are introduced, as shown below, with $\rho^{(k)}$ representing the density of the material in the k−th layer [25]:

$$\begin{aligned}\boldsymbol{\Gamma}_{\mathrm{Y}}^{(k)} &= \nu^{(k)}\rho^{(k)}c^{(k)}\boldsymbol{\Gamma}_{\mathrm{S}}^{(k)} \\ \boldsymbol{\Gamma}_{\mathrm{X}}^{(k)} &= \frac{\lambda^{(k)}}{\rho^{(k)}c^{(k)}}\boldsymbol{\Gamma}_{\mathrm{K}}^{(k)}\end{aligned} \tag{27}$$

The so-called heat-of-transport-ratio $Q_h^{(k)}$, which is defined as the heat exchanged during the mass diffusion process, is evaluated as follows:

$$Q_h^{(k)} = \mathrm{T}_0\sqrt{\frac{\rho^{(k)}c^{(k)}\lambda^{(k)}\nu^{(k)}R_g}{u_d^{(k)}\mathrm{C}_\infty^{(k)}}} \tag{28}$$

Here, $R_g = 461.9\,\mathrm{J/(kg\,K)}$ is the universal gas constant, while T_0 is the reference temperature of the solid. Finally, $\mathrm{C}_\infty^{(k)} = \rho^{(k)}M_\infty^{(k)}$ is the well-known equilibrium moisture content, which represents the mass concentration that occurs at equilibrium. The quantity $u_d^{(k)}$ is assumed to be equal to 0.1. The following expression is, thus, adopted for $\nu^{(k)}$:

$$\nu^{(k)} = \frac{Q_h^{(k)}}{\rho^{(k)}c^{(k)}} \tag{29}$$

Finally, it should be noted that the product $\lambda^{(k)}\nu^{(k)}$ is calibrated through experimental tests, as extensively shown in Ref. [9]. The rotation matrices from Eqs. (24) and (25) are now used to obtain the vectors $\overline{\boldsymbol{\Gamma}}_{\mathrm{a}}^{(k)}$ and $\overline{\boldsymbol{\Gamma}}_{\mathrm{b}}^{(k)}$ of the rotated thermal and hygroscopic expansion coefficients from Eq. (22), which are conveniently collected into the matrices $\overline{\mathbf{A}}^{(k)}$ and $\overline{\mathbf{B}}^{(k)}$ of size 3×3:

$$\overline{\mathbf{A}}^{(k)} = \mathbf{Y}_\varepsilon \odot \left(\mathbf{H}^{(k)T}\widehat{\mathbf{A}}^{(k)}\mathbf{H}^{(k)}\right)\overline{\mathbf{B}}^{(k)} = \mathbf{Y}_\varepsilon \odot \left(\mathbf{H}^{(k)T}\widehat{\mathbf{B}}^{(k)}\mathbf{H}^{(k)}\right) \tag{30}$$

In the previous equation, the matrix $\mathbf{Y}_\varepsilon$ of size 3×3 relates the engineering strain components to the 3D strain components, while the matrices $\overline{\mathbf{A}}^{(k)}$ and $\overline{\mathbf{B}}^{(k)}$ of size 3×3 contain the coefficients $\overline{a}_{ij}^{(k)}$ and $\overline{b}_{ij}^{(k)}$, with $i,j = 1,2,3$. In the relation provided below, the matrices $\mathbf{A}^{(k)}$ and $\mathbf{B}^{(k)}$ are conveniently introduced, whose elements are denoted by $a_{ij}^{(k)}$ and $b_{ij}^{(k)}$, respectively [25]:

$$\begin{aligned}\mathbf{A}^{(k)} &= \begin{bmatrix} a_{11}^{(k)} & a_{12}^{(k)} & a_{13}^{(k)} \\ a_{12}^{(k)} & a_{22}^{(k)} & a_{23}^{(k)} \\ a_{13}^{(k)} & a_{23}^{(k)} & a_{33}^{(k)} \end{bmatrix} = \begin{bmatrix} 1 & 2 & 2 \\ 2 & 1 & 2 \\ 2 & 2 & 1 \end{bmatrix} \odot \begin{bmatrix} \widehat{a}_{11}^{(k)} & \widehat{a}_{12}^{(k)} & \widehat{a}_{13}^{(k)} \\ \widehat{a}_{12}^{(k)} & \widehat{a}_{22}^{(k)} & \widehat{a}_{23}^{(k)} \\ \widehat{a}_{13}^{(k)} & \widehat{a}_{23}^{(k)} & \widehat{a}_{33}^{(k)} \end{bmatrix} = \mathbf{Y}_\varepsilon \odot \widehat{\mathbf{A}}^{(k)} \\ \mathbf{B}^{(k)} &= \begin{bmatrix} b_{11}^{(k)} & b_{12}^{(k)} & b_{13}^{(k)} \\ b_{12}^{(k)} & b_{22}^{(k)} & b_{23}^{(k)} \\ b_{13}^{(k)} & b_{23}^{(k)} & b_{33}^{(k)} \end{bmatrix} = \begin{bmatrix} 1 & 2 & 2 \\ 2 & 1 & 2 \\ 2 & 2 & 1 \end{bmatrix} \odot \begin{bmatrix} \widehat{b}_{11}^{(k)} & \widehat{b}_{12}^{(k)} & \widehat{b}_{13}^{(k)} \\ \widehat{b}_{12}^{(k)} & \widehat{b}_{22}^{(k)} & \widehat{b}_{23}^{(k)} \\ \widehat{b}_{13}^{(k)} & \widehat{b}_{23}^{(k)} & \widehat{b}_{33}^{(k)} \end{bmatrix} = \mathbf{Y}_\varepsilon \odot \widehat{\mathbf{B}}^{(k)}\end{aligned} \tag{31}$$

Finally, the hygro-thermal constitutive coefficients $\overline{\boldsymbol{\Gamma}}_{\mathrm{TT}}^{(k)} = \boldsymbol{\Gamma}_{\mathrm{TT}}^{(k)} = \xi_{11}^{(k)}$, $\overline{\boldsymbol{\Gamma}}_{\mathrm{CC}}^{(k)} = \boldsymbol{\Gamma}_{\mathrm{CC}}^{(k)} = \xi_{22}^{(k)}$ and $\overline{\boldsymbol{\Gamma}}_{\mathrm{TC}}^{(k)} = \boldsymbol{\Gamma}_{\mathrm{TC}}^{(k)} = \xi_{12}^{(k)}$ are derived from the specific chemical potential, based on the expression given below:

$$\Delta\mu^{(k)} = \mu^{(k)} - \mu_0^{(k)} = R_g\mathrm{T}^{(k)}\log\Delta\mathrm{C}^{(k)} \tag{32}$$

The following definitions are then obtained by setting $\mathrm{C}_0^{(k)} = 0$, as detailed in Ref. [25]:

$$\begin{aligned}\xi_{11}^{(k)} &= \left(\frac{\partial\eta^{(k)}}{\partial\mathrm{T}}\right)_{\boldsymbol{\varepsilon},\Delta\mathrm{C}} = \left(\frac{\partial\eta^{(k)}}{\partial\mathrm{T}}\right)_{\boldsymbol{\varepsilon},\mathrm{C}_\infty} = \frac{\rho^{(k)}c^{(k)}}{\mathrm{T}_0} \\ \xi_{22}^{(k)} &= \left(\frac{\partial\mu^{(k)}}{\partial\mathrm{C}}\right)_{\boldsymbol{\varepsilon},\Delta\mathrm{T}} = \left(\frac{\partial\mu^{(k)}}{\partial\mathrm{C}}\right)_{\boldsymbol{\varepsilon},\mathrm{T}_0} = \frac{R_g\mathrm{T}_0}{\mathrm{C}_\infty^{(k)} - \mathrm{C}_0^{(k)}} \cong \frac{R_g\mathrm{T}_0}{\mathrm{C}_\infty^{(k)}} = \frac{R_g\mathrm{T}_0}{\rho^{(k)}M_\infty^{(k)}} \\ \xi_{12}^{(k)} &= \left(\frac{\partial\mu^{(k)}}{\partial\mathrm{T}}\right)_{\boldsymbol{\varepsilon},\Delta\mathrm{C}} = \left(\frac{\partial\mu^{(k)}}{\partial\mathrm{T}}\right)_{\boldsymbol{\varepsilon},\mathrm{C}_\infty} = \left(\frac{\partial\eta^{(k)}}{\partial\mathrm{C}}\right)_{\boldsymbol{\varepsilon},\Delta\mathrm{T}} = \left(\frac{\partial\eta^{(k)}}{\partial\mathrm{C}}\right)_{\boldsymbol{\varepsilon},\mathrm{T}_0} = \\ &= -\frac{\Delta\mu^{(k)}}{\mathrm{T}_0} = -R_g\log\left(\mathrm{C}_\infty^{(k)} - \mathrm{C}_0^{(k)}\right) \cong -R_g\log\mathrm{C}_\infty^{(k)} = -R_g\log\left(\rho^{(k)}M_\infty^{(k)}\right)\end{aligned} \tag{33}$$

At this point, a new vector, denoted by $\overline{\boldsymbol{\chi}}^{(k)}$, is introduced, which modifies the 3D secondary variables vector $\boldsymbol{\chi}^{(k)}$, as follows:

$$\begin{bmatrix} \boldsymbol{\sigma}^{(k)} \\ \mathscr{B}^{(k)} \\ \eta^{(k)} \\ \mu^{(k)} \\ \overline{\mathbf{h}}^{(k)} \\ \overline{\mathbf{c}}^{(k)} \end{bmatrix} = \begin{bmatrix} \widehat{\mathbf{I}} & \mathbf{0} & \mathbf{0} & \mathbf{0} & \mathbf{0} & \mathbf{0} \\ \mathbf{0} & \mathbf{I} & \mathbf{0} & \mathbf{0} & \mathbf{0} & \mathbf{0} \\ \mathbf{0} & \mathbf{0} & 1 & 0 & \mathbf{0} & \mathbf{0} \\ \mathbf{0} & \mathbf{0} & 0 & 1 & \mathbf{0} & \mathbf{0} \\ \mathbf{0} & \mathbf{0} & \mathbf{0} & \mathbf{0} & \dfrac{1}{\mathrm{T}_0}\mathbf{I} & \dfrac{\mu_\infty}{\mathrm{T}_0}\mathbf{I} \\ \mathbf{0} & \mathbf{0} & \mathbf{0} & \mathbf{0} & \mathbf{0} & \dfrac{\mu_\infty}{\mathrm{C}_\infty}\mathbf{I} \end{bmatrix} \begin{bmatrix} \boldsymbol{\sigma}^{(k)} \\ \mathscr{B}^{(k)} \\ \eta^{(k)} \\ \mu^{(k)} \\ \mathbf{h}^{(k)} \\ \mathbf{c}^{(k)} \end{bmatrix} \Leftrightarrow \overline{\boldsymbol{\chi}}^{(k)} = \mathbf{B}\,\boldsymbol{\chi}^{(k)} \tag{34}$$

In the previous definitions, the matrices $\widehat{\mathbf{I}}$ and $\mathbf{I}$ are adopted, with sizes 6×6 and 3×3, respectively. In this way, the virtual variation $\delta\mathrm{Y}$ of the total energy of the system can be expressed as [25]:

$$\begin{aligned}\delta\mathrm{Y} &= \sum_{k=1}^{l}\int_{\alpha_1}\int_{\alpha_2}\int_{\zeta_k}^{\zeta_{k+1}}\left(\delta\overline{\boldsymbol{\pi}}^{(k)T}\overline{\boldsymbol{\chi}}^{(k)}\right)A_1A_2H_1H_2\,d\alpha_1 d\alpha_2 d\zeta \\ &= \sum_{\tau=0}^{N+1}\sum_{i=1}^{6}\int_{\alpha_1}\int_{\alpha_2}\left(\delta\overline{\boldsymbol{\pi}}^{(\tau)\alpha_i}\right)^T\overline{\mathbf{B}}\boldsymbol{\Sigma}^{(\tau)\alpha_i}A_1A_2\,d\alpha_1 d\alpha_2\end{aligned} \tag{35}$$

where $\delta\overline{\boldsymbol{\pi}}^{(k)}$ represents the virtual variation of the 3D primary variables of the model. As shown in Eq. (35), the introduction of the generalized kinematic model from Eq. (5) leads to the definition of the vector of generalized secondary variables for each $\tau = 0, \ldots, N+1$, which is expressed as $\Sigma^{(\tau)\alpha_i} = \left[\mathbf{S}^{(\tau)\alpha_i T} \quad \mathbf{B}^{(\tau)\alpha_i T} \quad E^{(\tau)\alpha_i} \quad M^{(\tau)\alpha_i} \quad \mathbf{H}^{(\tau)\alpha_i T} \quad \mathbf{C}^{(\tau)\alpha_i T}\right]^T$. The sub-vectors $\mathbf{S}^{(\tau)\alpha_i}, \mathbf{B}^{(\tau)\alpha_i}, \mathbf{H}^{(\tau)\alpha_i}, \mathbf{C}^{(\tau)\alpha_i}$ are reported below in extended form:

$$\begin{aligned}\mathbf{S}^{(\tau)\alpha_i} &= \left[N_1^{(\tau)\alpha_i} \quad N_2^{(\tau)\alpha_i} \quad N_{12}^{(\tau)\alpha_i} \quad N_{21}^{(\tau)\alpha_i} \quad T_1^{(\tau)\alpha_i} \quad T_2^{(\tau)\alpha_i} \quad P_1^{(\tau)\alpha_i} \quad P_2^{(\tau)\alpha_i} \quad S_3^{(\tau)\alpha_i}\right]^T \\ \mathbf{B}^{(\tau)\alpha_i} &= \left[B_1^{(\tau)\alpha_i} \quad B_2^{(\tau)\alpha_i} \quad B_3^{(\tau)\alpha_i}\right]^T \\ \mathbf{H}^{(\tau)\alpha_i} &= \left[H_1^{(\tau)\alpha_i} \quad H_2^{(\tau)\alpha_i} \quad H_3^{(\tau)\alpha_i}\right]^T \\ \mathbf{C}^{(\tau)\alpha_i} &= \left[C_1^{(\tau)\alpha_i} \quad C_2^{(\tau)\alpha_i} \quad C_3^{(\tau)\alpha_i}\right]^T\end{aligned} \tag{36}$$

In the same way, the matrix $\overline{\mathbf{B}}$ in Eq. (35) takes the following form by introducing a proper identity matrix of 9 rows and 9 columns:

$$\overline{\mathbf{B}} = \begin{bmatrix} \breve{\mathbf{I}} & \mathbf{0} & \mathbf{0} & \mathbf{0} & \mathbf{0} & \mathbf{0} \\ \mathbf{0} & \mathbf{I} & \mathbf{0} & \mathbf{0} & \mathbf{0} & \mathbf{0} \\ \mathbf{0} & \mathbf{0} & 1 & 0 & \mathbf{0} & \mathbf{0} \\ \mathbf{0} & \mathbf{0} & 0 & 1 & \mathbf{0} & \mathbf{0} \\ \mathbf{0} & \mathbf{0} & \mathbf{0} & \mathbf{0} & \frac{1}{\mathrm{T}_0}\mathbf{I} & \frac{\mu_\infty}{\mathrm{T}_0}\mathbf{I} \\ \mathbf{0} & \mathbf{0} & \mathbf{0} & \mathbf{0} & \mathbf{0} & \frac{\mu_\infty}{\mathrm{C}_\infty}\mathbf{I} \end{bmatrix} \tag{37}$$

By substituting the constitutive relationship from Eq. (20) and the higher-order definition Eqs. (18)–(35), the following generalized constitutive relation is derived, which connects the secondary variables vector $\boldsymbol{\Sigma}^{(\tau)\alpha_i}$, for each $\tau = 0,\ldots,N+1$, with the vectors of the generalized primary variables $\boldsymbol{\pi}^{(\eta)\alpha_j}$ with $\eta = 0,\ldots,N+1$:

$$\begin{aligned} \boldsymbol{\Sigma}^{(\tau)\alpha_i} &= \sum_{\eta=0}^{N+1}\sum_{j=1}^{6}\left(\sum_{k=1}^{l}\int_{\zeta_k}^{\zeta_{k+1}}\left(\mathbf{Z}^{(k\tau)\alpha_i}\right)^T\overline{\boldsymbol{\Gamma}}^{(k)}\mathbf{Z}^{(k\eta)\alpha_j}H_1H_2\,d\zeta\right)\boldsymbol{\pi}^{(\eta)\alpha_j} \\ &= \sum_{\eta=0}^{N+1}\sum_{j=1}^{6}\mathbf{A}^{(\tau\eta)\alpha_i\alpha_j}\boldsymbol{\pi}^{(\eta)\alpha_j} \end{aligned} \tag{38}$$

The arbitrary element of the generalized constitutive matrix $\mathbf{A}^{(\tau\eta)\alpha_i\alpha_j}$, denoted by $A_{rsnm\,(pq)}^{(\tau\eta)[fg]\,\alpha_i\alpha_j}$ with $r,s = \varepsilon,\psi,\mathrm{T},\mathrm{C},\theta,\lambda$, can be evaluated for each point of the rectangular physical domain using the following condensed relation [25], setting $\tau,\eta = 0,\ldots,N+1$, $n,m = 1,\ldots,17$, $p,q = 0,1,2$, and $i,j = 1,\ldots,6$:

$$A_{rs\,nm\,(pq)}^{(\tau\eta)[fg]\,\alpha_i\alpha_j} = \sum_{k=1}^{l}\int_{\zeta_k}^{\zeta_{k+1}}\overline{\Upsilon}_{nm}^{(k)}\frac{\partial^f F_\tau^{(k)\alpha_i}}{\partial\zeta^f}\,\frac{\partial^g F_\eta^{(k)\alpha_j}}{\partial\zeta^g}\,\frac{H_1H_2}{H_1^pH_2^q}\,d\zeta \tag{39}$$

Here, the coefficient $\overline{\Upsilon}_{nm}^{(k)} = \kappa\,\overline{\Gamma}_{nm}^{(k)}$ is defined from the element $\overline{\Gamma}_{nm}^{(k)}$ of the 3D constitutive matrix $\overline{\boldsymbol{\Gamma}}^{(k)}$ in Eq. (20). In addition, κ represents the shear correction factor, which is equal to 1, except for those kinematic models characterized by a uniform distribution of out-of-plane displacement field components, where the value 5/6 is assumed. The generalized constitutive matrix $\mathbf{A}^{(\tau\eta)\alpha_i\alpha_j}$ in Eq. (38) is conveniently expressed as follows [25]:

$$\mathbf{A}^{(\tau\eta)\alpha_i\alpha_j} = \begin{bmatrix} \mathbf{A}_{\varepsilon\varepsilon}^{(\tau\eta)\alpha_i\alpha_j} & \mathbf{A}_{\varepsilon\psi}^{(\tau\eta)\alpha_i\alpha_j} & \mathbf{A}_{\varepsilon\mathrm{T}}^{(\tau\eta)\alpha_i\alpha_j} & \mathbf{A}_{\varepsilon\mathrm{C}}^{(\tau\eta)\alpha_i\alpha_j} & \mathbf{0} & \mathbf{0} \\ \mathbf{A}_{\psi\varepsilon}^{(\tau\eta)\alpha_i\alpha_j} & \mathbf{A}_{\psi\psi}^{(\tau\eta)\alpha_i\alpha_j} & \mathbf{A}_{\psi\mathrm{T}}^{(\tau\eta)\alpha_i\alpha_j} & \mathbf{A}_{\psi\mathrm{C}}^{(\tau\eta)\alpha_i\alpha_j} & \mathbf{0} & \mathbf{0} \\ \mathbf{A}_{\mathrm{T}\varepsilon}^{(\tau\eta)\alpha_i\alpha_j} & \mathbf{A}_{\mathrm{T}\psi}^{(\tau\eta)\alpha_i\alpha_j} & \mathbf{A}_{\mathrm{TT}}^{(\tau\eta)\alpha_i\alpha_j} & \mathbf{A}_{\mathrm{TC}}^{(\tau\eta)\alpha_i\alpha_j} & \mathbf{0} & \mathbf{0} \\ \mathbf{A}_{\mathrm{C}\varepsilon}^{(\tau\eta)\alpha_i\alpha_j} & \mathbf{A}_{\mathrm{C}\psi}^{(\tau\eta)\alpha_i\alpha_j} & \mathbf{A}_{\mathrm{CT}}^{(\tau\eta)\alpha_i\alpha_j} & \mathbf{A}_{\mathrm{CC}}^{(\tau\eta)\alpha_i\alpha_j} & \mathbf{0} & \mathbf{0} \\ \mathbf{0} & \mathbf{0} & \mathbf{0} & \mathbf{0} & \mathbf{A}_{\theta\theta}^{(\tau\eta)\alpha_i\alpha_j} & \mathbf{A}_{\theta\lambda}^{(\tau\eta)\alpha_i\alpha_j} \\ \mathbf{0} & \mathbf{0} & \mathbf{0} & \mathbf{0} & \mathbf{A}_{\lambda\theta}^{(\tau\eta)\alpha_i\alpha_j} & \mathbf{A}_{\lambda\lambda}^{(\tau\eta)\alpha_i\alpha_j} \end{bmatrix} \tag{40}$$

The sub-matrices appearing in Eq. (40) are provided below to identify the position of each generalized term derived in Eq. (39):

$$\mathbf{A}_{\varepsilon\varepsilon}^{(\tau\eta)\alpha_i\alpha_j} = \left[\left(A_{\varepsilon\varepsilon nm(pq)}^{(\tau\eta)[fg]\alpha_i\alpha_j}\right)_{hs}\right]_{\substack{h=1,\ldots,9\\ s=1,\ldots,9}} = \left[\begin{array}{cccccc|ccc} A_{11(20)}^{(\tau\eta)[00]\alpha_i\alpha_j} & A_{12(11)}^{(\tau\eta)[00]\alpha_i\alpha_j} & A_{16(20)}^{(\tau\eta)[00]\alpha_i\alpha_j} & A_{16(11)}^{(\tau\eta)[00]\alpha_i\alpha_j} & A_{14(20)}^{(\tau\eta)[00]\alpha_i\alpha_j} & A_{15(11)}^{(\tau\eta)[00]\alpha_i\alpha_j} & A_{14(10)}^{(\tau\eta)[01]\alpha_i\alpha_j} & A_{15(10)}^{(\tau\eta)[01]\alpha_i\alpha_j} & A_{13(10)}^{(\tau\eta)[01]\alpha_i\alpha_j} \\ A_{12(11)}^{(\tau\eta)[00]\alpha_i\alpha_j} & A_{22(02)}^{(\tau\eta)[00]\alpha_i\alpha_j} & A_{26(11)}^{(\tau\eta)[00]\alpha_i\alpha_j} & A_{26(02)}^{(\tau\eta)[00]\alpha_i\alpha_j} & A_{24(11)}^{(\tau\eta)[00]\alpha_i\alpha_j} & A_{25(02)}^{(\tau\eta)[00]\alpha_i\alpha_j} & A_{24(01)}^{(\tau\eta)[01]\alpha_i\alpha_j} & A_{25(01)}^{(\tau\eta)[01]\alpha_i\alpha_j} & A_{23(01)}^{(\tau\eta)[01]\alpha_i\alpha_j} \\ A_{16(20)}^{(\tau\eta)[00]\alpha_i\alpha_j} & A_{26(11)}^{(\tau\eta)[00]\alpha_i\alpha_j} & A_{66(20)}^{(\tau\eta)[00]\alpha_i\alpha_j} & A_{66(11)}^{(\tau\eta)[00]\alpha_i\alpha_j} & A_{46(20)}^{(\tau\eta)[00]\alpha_i\alpha_j} & A_{56(11)}^{(\tau\eta)[00]\alpha_i\alpha_j} & A_{46(10)}^{(\tau\eta)[01]\alpha_i\alpha_j} & A_{56(10)}^{(\tau\eta)[01]\alpha_i\alpha_j} & A_{36(10)}^{(\tau\eta)[01]\alpha_i\alpha_j} \\ A_{16(11)}^{(\tau\eta)[00]\alpha_i\alpha_j} & A_{26(02)}^{(\tau\eta)[00]\alpha_i\alpha_j} & A_{66(11)}^{(\tau\eta)[00]\alpha_i\alpha_j} & A_{66(02)}^{(\tau\eta)[00]\alpha_i\alpha_j} & A_{46(11)}^{(\tau\eta)[00]\alpha_i\alpha_j} & A_{56(02)}^{(\tau\eta)[00]\alpha_i\alpha_j} & A_{46(01)}^{(\tau\eta)[01]\alpha_i\alpha_j} & A_{56(01)}^{(\tau\eta)[01]\alpha_i\alpha_j} & A_{36(01)}^{(\tau\eta)[01]\alpha_i\alpha_j} \\ A_{14(20)}^{(\tau\eta)[00]\alpha_i\alpha_j} & A_{24(11)}^{(\tau\eta)[00]\alpha_i\alpha_j} & A_{46(20)}^{(\tau\eta)[00]\alpha_i\alpha_j} & A_{46(11)}^{(\tau\eta)[00]\alpha_i\alpha_j} & A_{44(20)}^{(\tau\eta)[00]\alpha_i\alpha_j} & A_{45(11)}^{(\tau\eta)[00]\alpha_i\alpha_j} & A_{44(10)}^{(\tau\eta)[01]\alpha_i\alpha_j} & A_{45(10)}^{(\tau\eta)[01]\alpha_i\alpha_j} & A_{34(10)}^{(\tau\eta)[01]\alpha_i\alpha_j} \\ A_{15(11)}^{(\tau\eta)[00]\alpha_i\alpha_j} & A_{25(02)}^{(\tau\eta)[00]\alpha_i\alpha_j} & A_{56(11)}^{(\tau\eta)[00]\alpha_i\alpha_j} & A_{56(02)}^{(\tau\eta)[00]\alpha_i\alpha_j} & A_{45(11)}^{(\tau\eta)[00]\alpha_i\alpha_j} & A_{55(02)}^{(\tau\eta)[00]\alpha_i\alpha_j} & A_{45(01)}^{(\tau\eta)[01]\alpha_i\alpha_j} & A_{55(01)}^{(\tau\eta)[01]\alpha_i\alpha_j} & A_{35(01)}^{(\tau\eta)[01]\alpha_i\alpha_j} \\ \hline A_{14(10)}^{(\tau\eta)[10]\alpha_i\alpha_j} & A_{24(01)}^{(\tau\eta)[10]\alpha_i\alpha_j} & A_{46(10)}^{(\tau\eta)[10]\alpha_i\alpha_j} & A_{46(01)}^{(\tau\eta)[10]\alpha_i\alpha_j} & A_{44(10)}^{(\tau\eta)[10]\alpha_i\alpha_j} & A_{45(01)}^{(\tau\eta)[10]\alpha_i\alpha_j} & A_{44(00)}^{(\tau\eta)[11]\alpha_i\alpha_j} & A_{45(00)}^{(\tau\eta)[11]\alpha_i\alpha_j} & A_{34(00)}^{(\tau\eta)[11]\alpha_i\alpha_j} \\ A_{15(10)}^{(\tau\eta)[10]\alpha_i\alpha_j} & A_{25(01)}^{(\tau\eta)[10]\alpha_i\alpha_j} & A_{56(10)}^{(\tau\eta)[10]\alpha_i\alpha_j} & A_{56(01)}^{(\tau\eta)[10]\alpha_i\alpha_j} & A_{45(10)}^{(\tau\eta)[10]\alpha_i\alpha_j} & A_{55(01)}^{(\tau\eta)[10]\alpha_i\alpha_j} & A_{45(00)}^{(\tau\eta)[11]\alpha_i\alpha_j} & A_{55(00)}^{(\tau\eta)[11]\alpha_i\alpha_j} & A_{35(00)}^{(\tau\eta)[11]\alpha_i\alpha_j} \\ A_{13(10)}^{(\tau\eta)[10]\alpha_i\alpha_j} & A_{23(01)}^{(\tau\eta)[10]\alpha_i\alpha_j} & A_{36(10)}^{(\tau\eta)[10]\alpha_i\alpha_j} & A_{36(01)}^{(\tau\eta)[10]\alpha_i\alpha_j} & A_{34(10)}^{(\tau\eta)[10]\alpha_i\alpha_j} & A_{35(01)}^{(\tau\eta)[10]\alpha_i\alpha_j} & A_{34(00)}^{(\tau\eta)[11]\alpha_i\alpha_j} & A_{35(00)}^{(\tau\eta)[11]\alpha_i\alpha_j} & A_{33(00)}^{(\tau\eta)[11]\alpha_i\alpha_j} \end{array}\right]$$

$$\mathbf{A}_{\psi\psi}^{(\tau\eta)\alpha_i\alpha_j} = \left[\left(A_{\psi\psi nm(pq)}^{(\tau\eta)[fg]\alpha_i\alpha_j}\right)_{hs}\right]_{\substack{h=1,2,3\\ s=1,2,3}} = \left[\begin{array}{cc|c} M_{11(20)}^{(\tau\eta)[00]\alpha_i\alpha_j} & M_{12(11)}^{(\tau\eta)[00]\alpha_i\alpha_j} & M_{13(10)}^{(\tau\eta)[01]\alpha_i\alpha_j} \\ M_{12(11)}^{(\tau\eta)[00]\alpha_i\alpha_j} & M_{22(02)}^{(\tau\eta)[00]\alpha_i\alpha_j} & M_{23(01)}^{(\tau\eta)[01]\alpha_i\alpha_j} \\ \hline M_{13(10)}^{(\tau\eta)[10]\alpha_i\alpha_j} & M_{23(01)}^{(\tau\eta)[10]\alpha_i\alpha_j} & M_{33(00)}^{(\tau\eta)[11]\alpha_i\alpha_j} \end{array}\right]$$

$$\mathbf{A}_{\varepsilon\psi}^{(\tau\eta)\alpha_i\alpha_j} = \left[\left(A_{\varepsilon\psi nm(pq)}^{(\tau\eta)[fg]\alpha_i\alpha_j}\right)_{hs}\right]_{\substack{h=1,\ldots,9\\ s=1,2,3}} = -\left[\begin{array}{cccccc|ccc} Q_{11(20)}^{(\tau\eta)[00]\alpha_i\alpha_j} & Q_{12(11)}^{(\tau\eta)[00]\alpha_i\alpha_j} & Q_{16(20)}^{(\tau\eta)[00]\alpha_i\alpha_j} & Q_{16(11)}^{(\tau\eta)[00]\alpha_i\alpha_j} & Q_{14(20)}^{(\tau\eta)[00]\alpha_i\alpha_j} & Q_{15(11)}^{(\tau\eta)[00]\alpha_i\alpha_j} & Q_{14(10)}^{(\tau\eta)[10]\alpha_i\alpha_j} & Q_{15(10)}^{(\tau\eta)[10]\alpha_i\alpha_j} & Q_{13(10)}^{(\tau\eta)[10]\alpha_i\alpha_j} \\ Q_{21(11)}^{(\tau\eta)[00]\alpha_i\alpha_j} & Q_{22(02)}^{(\tau\eta)[00]\alpha_i\alpha_j} & Q_{26(11)}^{(\tau\eta)[00]\alpha_i\alpha_j} & Q_{26(02)}^{(\tau\eta)[00]\alpha_i\alpha_j} & Q_{24(11)}^{(\tau\eta)[00]\alpha_i\alpha_j} & Q_{25(02)}^{(\tau\eta)[00]\alpha_i\alpha_j} & Q_{24(01)}^{(\tau\eta)[10]\alpha_i\alpha_j} & Q_{25(01)}^{(\tau\eta)[10]\alpha_i\alpha_j} & Q_{23(01)}^{(\tau\eta)[10]\alpha_i\alpha_j} \\ \hline Q_{31(10)}^{(\tau\eta)[01]\alpha_i\alpha_j} & Q_{32(01)}^{(\tau\eta)[01]\alpha_i\alpha_j} & Q_{36(10)}^{(\tau\eta)[01]\alpha_i\alpha_j} & Q_{36(01)}^{(\tau\eta)[01]\alpha_i\alpha_j} & Q_{34(10)}^{(\tau\eta)[01]\alpha_i\alpha_j} & Q_{35(01)}^{(\tau\eta)[01]\alpha_i\alpha_j} & Q_{34(00)}^{(\tau\eta)[11]\alpha_i\alpha_j} & Q_{35(00)}^{(\tau\eta)[11]\alpha_i\alpha_j} & Q_{33(00)}^{(\tau\eta)[11]\alpha_i\alpha_j} \end{array}\right]^T$$

$$\mathbf{A}_{\psi\varepsilon}^{(\tau\eta)\alpha_i\alpha_j} = \left[\left(A_{\psi\varepsilon nm(pq)}^{(\tau\eta)[fg]\alpha_i\alpha_j}\right)_{hs}\right]_{\substack{h=1,2,3\\ s=1,\ldots,9}} = \left[\begin{array}{cccccc|ccc} Q_{11(20)}^{(\tau\eta)[00]\alpha_i\alpha_j} & Q_{12(11)}^{(\tau\eta)[00]\alpha_i\alpha_j} & Q_{16(20)}^{(\tau\eta)[00]\alpha_i\alpha_j} & Q_{16(11)}^{(\tau\eta)[00]\alpha_i\alpha_j} & Q_{14(20)}^{(\tau\eta)[00]\alpha_i\alpha_j} & Q_{15(11)}^{(\tau\eta)[00]\alpha_i\alpha_j} & Q_{14(10)}^{(\tau\eta)[01]\alpha_i\alpha_j} & Q_{15(10)}^{(\tau\eta)[01]\alpha_i\alpha_j} & Q_{13(10)}^{(\tau\eta)[01]\alpha_i\alpha_j} \\ Q_{21(11)}^{(\tau\eta)[00]\alpha_i\alpha_j} & Q_{22(02)}^{(\tau\eta)[00]\alpha_i\alpha_j} & Q_{26(11)}^{(\tau\eta)[00]\alpha_i\alpha_j} & Q_{26(02)}^{(\tau\eta)[00]\alpha_i\alpha_j} & Q_{24(11)}^{(\tau\eta)[00]\alpha_i\alpha_j} & Q_{25(02)}^{(\tau\eta)[00]\alpha_i\alpha_j} & Q_{24(01)}^{(\tau\eta)[01]\alpha_i\alpha_j} & Q_{25(01)}^{(\tau\eta)[01]\alpha_i\alpha_j} & Q_{23(01)}^{(\tau\eta)[01]\alpha_i\alpha_j} \\ \hline Q_{31(10)}^{(\tau\eta)[10]\alpha_i\alpha_j} & Q_{32(01)}^{(\tau\eta)[10]\alpha_i\alpha_j} & Q_{36(10)}^{(\tau\eta)[10]\alpha_i\alpha_j} & Q_{36(01)}^{(\tau\eta)[10]\alpha_i\alpha_j} & Q_{34(10)}^{(\tau\eta)[10]\alpha_i\alpha_j} & Q_{35(01)}^{(\tau\eta)[10]\alpha_i\alpha_j} & Q_{34(00)}^{(\tau\eta)[11]\alpha_i\alpha_j} & Q_{35(00)}^{(\tau\eta)[11]\alpha_i\alpha_j} & Q_{33(00)}^{(\tau\eta)[11]\alpha_i\alpha_j} \end{array}\right]$$

$$\mathbf{A}_{\varepsilon\mathrm{T}}^{(\tau\eta)\alpha_i\alpha_j} = \left[\left(A_{\varepsilon\mathrm{T}nm(pq)}^{(\tau\eta)[fg]\alpha_i\alpha_j}\right)_{hs}\right]_{\substack{h=1,\dots,9\\ s=1}} = -\begin{bmatrix} Z_{11(10)}^{(\tau\eta)[00]\alpha_i\alpha_j} & Z_{22(01)}^{(\tau\eta)[00]\alpha_i\alpha_j} & Z_{12(10)}^{(\tau\eta)[00]\alpha_i\alpha_j} & Z_{12(01)}^{(\tau\eta)[00]\alpha_i\alpha_j} & Z_{13(10)}^{(\tau\eta)[00]\alpha_i\alpha_j} & Z_{23(01)}^{(\tau\eta)[00]\alpha_i\alpha_j} & Z_{13(00)}^{(\tau\eta)[10]\alpha_i\alpha_j} & Z_{23(00)}^{(\tau\eta)[10]\alpha_i\alpha_j} & Z_{33(00)}^{(\tau\eta)[10]\alpha_i\alpha_j} \end{bmatrix}^T$$

$$\mathbf{A}_{T\varepsilon}^{(\tau\eta)\alpha_i\alpha_j} = \left[\left(A_{T\varepsilon nm(pq)}^{(\tau\eta)[fg]\alpha_i\alpha_j}\right)_{hs}\right]_{\substack{h=1\\ s=1,\dots,9}} = \begin{bmatrix} Z_{11(10)}^{(\tau\eta)[00]\alpha_i\alpha_j} & Z_{22(01)}^{(\tau\eta)[00]\alpha_i\alpha_j} & Z_{12(10)}^{(\tau\eta)[00]\alpha_i\alpha_j} & Z_{12(01)}^{(\tau\eta)[00]\alpha_i\alpha_j} & Z_{13(10)}^{(\tau\eta)[00]\alpha_i\alpha_j} & Z_{23(01)}^{(\tau\eta)[00]\alpha_i\alpha_j} & Z_{13(00)}^{(\tau\eta)[01]\alpha_i\alpha_j} & Z_{23(00)}^{(\tau\eta)[01]\alpha_i\alpha_j} & Z_{33(00)}^{(\tau\eta)[01]\alpha_i\alpha_j} \end{bmatrix}$$

$$\mathbf{A}_{\varepsilon\mathrm{C}}^{(\tau\eta)\alpha_i\alpha_j} = \left[\left(A_{\varepsilon\mathrm{C}nm(pq)}^{(\tau\eta)[fg]\alpha_i\alpha_j}\right)_{hs}\right]_{\substack{h=1,..,9\\ s=1}} = -\begin{bmatrix} E_{11(10)}^{(\tau\eta)[00]\alpha_i\alpha_j} & E_{22(01)}^{(\tau\eta)[00]\alpha_i\alpha_j} & E_{12(10)}^{(\tau\eta)[00]\alpha_i\alpha_j} & E_{12(01)}^{(\tau\eta)[00]\alpha_i\alpha_j} & E_{13(10)}^{(\tau\eta)[00]\alpha_i\alpha_j} & E_{23(01)}^{(\tau\eta)[00]\alpha_i\alpha_j} & E_{13(00)}^{(\tau\eta)[10]\alpha_i\alpha_j} & E_{23(00)}^{(\tau\eta)[10]\alpha_i\alpha_j} & E_{33(00)}^{(\tau\eta)[10]\alpha_i\alpha_j} \end{bmatrix}^T$$

$$\mathbf{A}_{C\varepsilon}^{(\tau\eta)\alpha_i\alpha_j} = \left[\left(A_{C\varepsilon nm(pq)}^{(\tau\eta)[fg]\alpha_i\alpha_j}\right)_{hs}\right]_{\substack{h=1\\ s=1,\dots,9}} = \begin{bmatrix} E_{11(10)}^{(\tau\eta)[00]\alpha_i\alpha_j} & E_{22(01)}^{(\tau\eta)[00]\alpha_i\alpha_j} & E_{12(10)}^{(\tau\eta)[00]\alpha_i\alpha_j} & E_{12(01)}^{(\tau\eta)[00]\alpha_i\alpha_j} & E_{13(10)}^{(\tau\eta)[00]\alpha_i\alpha_j} & E_{23(01)}^{(\tau\eta)[00]\alpha_i\alpha_j} & E_{13(00)}^{(\tau\eta)[01]\alpha_i\alpha_j} & E_{23(00)}^{(\tau\eta)[01]\alpha_i\alpha_j} & E_{33(00)}^{(\tau\eta)[01]\alpha_i\alpha_j} \end{bmatrix}$$

$$\mathbf{A}_{\psi\mathrm{T}}^{(\tau\eta)\alpha_i\alpha_j} = \left[\left(A_{\psi\mathrm{T}nm(pq)}^{(\tau\eta)[fg]\,\alpha_i\alpha_j}\right)_{hs}\right]_{\substack{h=1,2,3\\ s=1}} = \begin{bmatrix} W_{11(10)}^{(\tau\eta)[00]\alpha_i\alpha_j} & W_{22(01)}^{(\tau\eta)[00]\alpha_i\alpha_j} & W_{33(00)}^{(\tau\eta)[01]\alpha_i\alpha_j} \end{bmatrix}^T$$

$$\mathbf{A}_{\mathrm{T}\psi}^{(\tau\eta)\alpha_i\alpha_j} = \left[\left(A_{\mathrm{T}\psi nm(pq)}^{(\tau\eta)[fg]\,\alpha_i\alpha_j}\right)_{hs}\right]_{\substack{h=1\\ s=1,2,3}} = \begin{bmatrix} W_{11(10)}^{(\tau\eta)[00]\alpha_i\alpha_j} & W_{22(01)}^{(\tau\eta)[00]\alpha_i\alpha_j} & W_{33(00)}^{(\tau\eta)[10]\alpha_i\alpha_j} \end{bmatrix}$$

$$\mathbf{A}_{\psi\mathrm{C}}^{(\tau\eta)\alpha_i\alpha_j} = \left[\left(A_{\psi\mathrm{C}nm(pq)}^{(\tau\eta)[fg]\,\alpha_i\alpha_j}\right)_{hs}\right]_{\substack{h=1,2,3\\ s=1}} = \begin{bmatrix} F_{11(10)}^{(\tau\eta)[00]\alpha_i\alpha_j} & F_{22(01)}^{(\tau\eta)[00]\alpha_i\alpha_j} & F_{33(00)}^{(\tau\eta)[01]\alpha_i\alpha_j} \end{bmatrix}^T$$

$$\mathbf{A}_{\mathrm{C}\psi}^{(\tau\eta)\alpha_i\alpha_j} = \left[\left(A_{\mathrm{C}\psi nm(pq)}^{(\tau\eta)[fg]\,\alpha_i\alpha_j}\right)_{hs}\right]_{\substack{h=1\\ s=1,2,3}} = \begin{bmatrix} F_{11(10)}^{(\tau\eta)[00]\alpha_i\alpha_j} & F_{22(01)}^{(\tau\eta)[00]\alpha_i\alpha_j} & F_{33(00)}^{(\tau\eta)[10]\alpha_i\alpha_j} \end{bmatrix}$$

$$\mathbf{A}_{\mathrm{TT}}^{(\tau\eta)\alpha_i\alpha_j} = \left[\left(A_{\mathrm{TT}nm(pq)}^{(\tau\eta)[fg]\,\alpha_i\alpha_j}\right)_{hs}\right]_{\substack{h=1\\ s=1}} = C_{11(00)}^{(\tau\eta)[00]\alpha_i\alpha_j}$$

$$\mathbf{A}_{\mathrm{CC}}^{(\tau\eta)\alpha_i\alpha_j} = \left[\left(A_{\mathrm{CC}nm(pq)}^{(\tau\eta)[fg]\,\alpha_i\alpha_j}\right)_{hs}\right]_{\substack{h=1\\ s=1}} = T_{11(00)}^{(\tau\eta)[00]\alpha_i\alpha_j}$$

$$\mathbf{A}_{\mathrm{TC}}^{(\tau\eta)\alpha_i\alpha_j} = \mathbf{A}_{\mathrm{CT}}^{(\tau\eta)\alpha_i\alpha_j} = \left[\left(A_{\mathrm{TC}nm(pq)}^{(\tau\eta)[fg]\,\alpha_i\alpha_j}\right)_{hs}\right]_{\substack{h=1\\ s=1}} = B_{11(00)}^{(\tau\eta)[00]\alpha_i\alpha_j}$$

$$\mathbf{A}_{\theta\theta}^{(\tau\eta)\alpha_i\alpha_j} = \left[\left(A_{\theta\theta nm(pq)}^{(\tau\eta)[fg]\alpha_i\alpha_j}\right)_{hs}\right]_{\substack{h=1,2,3\\ s=1,2,3}} = \left[\begin{array}{cc|c} K_{11(20)}^{(\tau\eta)[00]\alpha_i\alpha_j} & K_{12(11)}^{(\tau\eta)[00]\alpha_i\alpha_j} & K_{13(10)}^{(\tau\eta)[01]\alpha_i\alpha_j} \\ K_{12(11)}^{(\tau\eta)[00]\alpha_i\alpha_j} & K_{22(02)}^{(\tau\eta)[00]\alpha_i\alpha_j} & K_{23(01)}^{(\tau\eta)[01]\alpha_i\alpha_j} \\ \hline K_{13(10)}^{(\tau\eta)[10]\alpha_i\alpha_j} & K_{23(01)}^{(\tau\eta)[10]\alpha_i\alpha_j} & K_{33(00)}^{(\tau\eta)[11]\alpha_i\alpha_j} \end{array}\right]$$

$$\mathbf{A}_{\lambda\lambda}^{(\tau\eta)\alpha_i\alpha_j} = \left[\left(A_{\lambda\lambda nm(pq)}^{(\tau\eta)[fg]\alpha_i\alpha_j}\right)_{hs}\right]_{\substack{h=1,2,3\\ s=1,2,3}} = \left[\begin{array}{cc|c} S_{11(20)}^{(\tau\eta)[00]\alpha_i\alpha_j} & S_{12(11)}^{(\tau\eta)[00]\alpha_i\alpha_j} & S_{13(10)}^{(\tau\eta)[01]\alpha_i\alpha_j} \\ S_{12(11)}^{(\tau\eta)[00]\alpha_i\alpha_j} & S_{22(02)}^{(\tau\eta)[00]\alpha_i\alpha_j} & S_{23(01)}^{(\tau\eta)[01]\alpha_i\alpha_j} \\ \hline S_{13(10)}^{(\tau\eta)[10]\alpha_i\alpha_j} & S_{23(01)}^{(\tau\eta)[10]\alpha_i\alpha_j} & S_{33(00)}^{(\tau\eta)[11]\alpha_i\alpha_j} \end{array}\right]$$

$$\mathbf{A}_{\lambda\theta}^{(\tau\eta)\alpha_i\alpha_j} = \left[\left(A_{\lambda\theta nm(pq)}^{(\tau\eta)[fg]\alpha_i\alpha_j}\right)_{hs}\right]_{\substack{h=1,2,3\\ s=1,2,3}} = \left[\begin{array}{cc|c} X_{11(20)}^{(\tau\eta)[00]\alpha_i\alpha_j} & X_{12(11)}^{(\tau\eta)[00]\alpha_i\alpha_j} & X_{13(10)}^{(\tau\eta)[01]\alpha_i\alpha_j} \\ X_{12(11)}^{(\tau\eta)[00]\alpha_i\alpha_j} & X_{22(02)}^{(\tau\eta)[00]\alpha_i\alpha_j} & X_{23(01)}^{(\tau\eta)[01]\alpha_i\alpha_j} \\ \hline X_{13(10)}^{(\tau\eta)[10]\alpha_i\alpha_j} & X_{23(01)}^{(\tau\eta)[10]\alpha_i\alpha_j} & X_{33(00)}^{(\tau\eta)[11]\alpha_i\alpha_j} \end{array}\right]$$

$$\mathbf{A}_{\theta\lambda}^{(\tau\eta)\alpha_i\alpha_j} = \left[\left(A_{\theta\lambda nm(pq)}^{(\tau\eta)[fg]\alpha_i\alpha_j}\right)_{hs}\right]_{\substack{h=1,2,3\\ s=1,2,3}} = \left[\begin{array}{cc|c} Y_{11(20)}^{(\tau\eta)[00]\alpha_i\alpha_j} & Y_{12(11)}^{(\tau\eta)[00]\alpha_i\alpha_j} & Y_{13(10)}^{(\tau\eta)[01]\alpha_i\alpha_j} \\ Y_{12(11)}^{(\tau\eta)[00]\alpha_i\alpha_j} & Y_{22(02)}^{(\tau\eta)[00]\alpha_i\alpha_j} & Y_{23(01)}^{(\tau\eta)[01]\alpha_i\alpha_j} \\ \hline Y_{13(10)}^{(\tau\eta)[10]\alpha_i\alpha_j} & Y_{23(01)}^{(\tau\eta)[10]\alpha_i\alpha_j} & Y_{33(00)}^{(\tau\eta)[11]\alpha_i\alpha_j} \end{array}\right] \tag{41}$$

Finally, a more practical form of the generalized constitutive relation from Eq. (38) is derived by introducing the definition of the generalized primary variables, as given in Eq. (18), in terms of the generalized configuration variable vector. The resulting expression is:

$$\mathbf{\Sigma}^{(\tau)\alpha_i} = \sum_{\eta=0}^{N+1}\sum_{j=1}^{6}\mathbf{A}^{(\tau\eta)\alpha_i\alpha_j}\mathbf{D}_{\Omega}^{\alpha_j}\boldsymbol{\delta}^{(\eta)} = \sum_{\eta=0}^{N+1}\mathbf{O}^{(\tau\eta)\alpha_i}\boldsymbol{\delta}^{(\eta)} \tag{42}$$

The elements of the matrix $\mathbf{O}^{(\tau\eta)\alpha_i}$ for an arbitrary $\tau,\eta = 0,\dots,N+1$ are provided in Ref. [25].

The doubly-curved solid is assumed to be subjected to various multifield surface loads acting at $\zeta = h/2$ (+) and $\zeta = -h/2$ (−), which are the heights of the top and bottom surfaces of the panel, respectively. These loads include the mechanical surface loads $q_1^{(-)}, q_2^{(-)}, q_3^{(-)}$ and $q_1^{(+)}$, $q_2^{(+)}$, $q_3^{(+)}$, the surface tractions $q_{1efk}^{(-)}, q_{2efk}^{(-)}, q_{3efk}^{(-)}$ and $q_{1efk}^{(+)}, q_{2efk}^{(+)}, q_{3efk}^{(+)}$ induced by an external elastic foundation, as well as the surface magnetic fluxes $q_{\mathrm{B}}^{(-)}, q_{\mathrm{B}}^{(+)}$, the thermal fluxes $q_{\mathrm{T}}^{(-)}, q_{\mathrm{T}}^{(+)}$, and the hygrometric fluxes $q_{\mathrm{C}}^{(-)}$, $q_{\mathrm{C}}^{(+)}$. All these external surface loads are defined as the product of a normalized distribution $\tilde{q}_\alpha^{(\pm)}$ with α = 1, 2, 3, B, T, C, depending on the geometry principal coordinates α_1, α_2, and the corresponding magnitude $\overline{q}_\alpha^{(\pm)}$, as follows:

$$q_\alpha^{(\pm)} = \overline{q}_\alpha^{(\pm)}\tilde{q}_\alpha^{(\pm)}(\alpha_1,\alpha_2) \tag{43}$$

The virtual work of the multifield surface actions in Eq. (43) is $\delta L_s = \delta L_{es} + \delta L_{fs} + \delta \mathrm{Q}_{\psi s} + \delta \mathrm{Q}_{\mathrm{T}s} + \delta \mathrm{Q}_{\mathrm{C}s}$, where δL_{es} and δL_{fs} are the virtual work of mechanical surface loads and from elastic foundation, respectively, $\delta \mathrm{Q}_{\psi s}$ is the virtual work of magnetic fluxes, while $\delta \mathrm{Q}_{\mathrm{T}s}$ and $\delta \mathrm{Q}_{\mathrm{C}s}$ are the virtual works of thermal loads and moisture fluxes, respectively. In this way, the total virtual work δL_s can be derived from the integration of these contributions over the reference surface of the doubly-curved shell. To this end, the scaling parameters $H_i^{(-)}$ and $H_i^{(+)}$ are defined with $i = 1, 2$ by assuming $\zeta = h/2$ and $\zeta = -h/2$, respectively:

$$\begin{aligned} \delta L_s = \int_{\alpha_1}\int_{\alpha_2}\Bigg(\Bigg(& q_{1s}^{(-)}\delta U_1^{(-)} + q_{2s}^{(-)}\delta U_2^{(-)} + q_{3s}^{(-)}\delta U_3^{(-)} + q_{\mathrm{B}s}^{(-)}\delta\Delta\psi^{(-)} + \frac{q_{\mathrm{T}s}^{(-)}}{\mathrm{T}_0}\delta\Delta\mathrm{T}^{(-)} + \frac{\mu_\infty q_{\mathrm{C}s}^{(-)}}{\mathrm{C}_\infty}\delta\Delta\mathrm{C}^{(-)}\Bigg)H_1^{(-)}H_2^{(-)} + \\ & + \left(q_{1s}^{(+)}\delta U_1^{(+)} + q_{2s}^{(+)}\delta U_2^{(+)} + q_{3s}^{(+)}\delta U_3^{(+)} + q_{\mathrm{B}s}^{(+)}\delta\Delta\psi^{(+)} + \frac{q_{\mathrm{T}s}^{(+)}}{\mathrm{T}_0}\delta\Delta\mathrm{T}^{(+)} + \frac{\mu_\infty q_{\mathrm{C}s}^{(+)}}{\mathrm{C}_\infty}\delta\Delta\mathrm{C}^{(+)}\right)H_1^{(+)}H_2^{(+)}\Bigg)A_1A_2\,d\alpha_1 d\alpha_2 \end{aligned} \tag{44}$$

with $q_{is}^{(-)} = q_i^{(-)} + q_{iefk}^{(-)}$ and $q_{is}^{(+)} = q_i^{(+)} + q_{iefk}^{(+)}$ for $i = 1, 2, 3$, while $q_{\alpha s}^{(-)} = q_\alpha^{(-)}$ and $q_{\alpha s}^{(+)} = q_\alpha^{(+)}$ for $\alpha = \mathrm{B}, \mathrm{T}, \mathrm{C}$. The actions from the elastic foundation at the top and bottom surfaces are derived using the well-known Winkler-Pasternak model, as shown in the following definitions:

$$\begin{aligned} q_{1efk}^{(\pm)} &= -k_{1f}^{(\pm)}U_1^{(\pm)} \\ q_{2efk}^{(\pm)} &= -k_{2f}^{(\pm)}U_2^{(\pm)} \\ q_{3efk}^{(\pm)} &= -k_{3f}^{(\pm)}U_3^{(\pm)} + G_f^{(\pm)}\nabla_{(\pm)}^2 U_3^{(\pm)} \end{aligned} \tag{45}$$

In the previous relation, the symbol $\nabla_{(\pm)}^2$ refers to the Laplacian operator associated with the top and bottom surfaces of the shell. This operator is expressed in curvilinear principal coordinates as follows [25]:

$$\begin{aligned} \nabla_{(\pm)}^2 = \Bigg(& \frac{1}{A_1^2\left(H_1^{(\pm)}\right)^2}\frac{\partial^2}{\partial\alpha_1^2} + \frac{1}{A_2^2\left(H_2^{(\pm)}\right)^2}\frac{\partial^2}{\partial\alpha_2^2} + \Bigg(\frac{1}{A_1^2A_2\left(H_1^{(\pm)}\right)^2}\frac{\partial A_2}{\partial\alpha_1} - \frac{h}{2A_1^2R_2^2\left(H_1^{(\pm)}\right)^2 H_2^{(\pm)}}\frac{\partial R_2}{\partial\alpha_1} + \\ & - \frac{1}{A_1^3\left(H_1^{(\pm)}\right)^2}\frac{\partial A_1}{\partial\alpha_1} - \frac{h}{2A_1^2R_1^2\left(H_1^{(\pm)}\right)^3}\frac{\partial R_1}{\partial\alpha_1}\Bigg)\frac{\partial}{\partial\alpha_1} + \Bigg(\frac{1}{A_1A_2^2\left(H_2^{(\pm)}\right)^2}\frac{\partial A_1}{\partial\alpha_2} + \frac{h}{2A_2^2R_1^2\left(H_2^{(\pm)}\right)^2 H_1^{(\pm)}}\frac{\partial R_1}{\partial\alpha_2} + \\ & - \frac{1}{A_2^3\left(H_2^{(\pm)}\right)^2}\frac{\partial A_2}{\partial\alpha_2} - \frac{h}{2A_2^2R_2^2\left(H_2^{(\pm)}\right)^3}\frac{\partial R_2}{\partial\alpha_2}\Bigg)\frac{\partial}{\partial\alpha_2}\Bigg) \end{aligned} \tag{46}$$

The Winkler foundation model is derived from Eq. (45) by setting $G_f^{(\pm)} = 0$. If the kinematic model from Eq. (5) is used to define the virtual variation of the 3D configuration variables at the top and bottom of the solid, Eq. (44) is expressed as follows [25]:

$$\delta L_s = \int_{\alpha_1}\int_{\alpha_2}\sum_{\tau=0}^{N+1}\left(q_{1s}^{(\tau)}\delta u_1^{(\tau)} + q_{2s}^{(\tau)}\delta u_2^{(\tau)} + q_{3s}^{(\tau)}\delta u_3^{(\tau)} + q_{\mathrm{B}s}^{(\tau)}\delta\psi^{(\tau)} + \frac{q_{\mathrm{T}s}^{(\tau)}}{\mathrm{T}_0}\delta\xi^{(\tau)} + \frac{\upmu_\infty q_{\mathrm{C}s}^{(\tau)}}{\mathrm{C}_\infty}\delta\kappa^{(\tau)}\right)A_1A_2\,d\alpha_1 d\alpha_2 \tag{47}$$

In the previous relation, the virtual work δL_s of surface loads acting on the outer surfaces is expressed in terms of the generalized surface loads $q_{\alpha s}^{(\tau)}$ with $\alpha = 1,2,3,\mathrm{B},\mathrm{T},\mathrm{C}$, introduced for each $\tau = 0,\dots,N+1$:

$$\begin{aligned}
q_{1s}^{(\tau)} &= q_{1s}^{(-)}F_\tau^{(1)\alpha_1(-)}H_1^{(-)}H_2^{(-)} + q_{1s}^{(+)}F_\tau^{(l)\alpha_1(+)}H_1^{(+)}H_2^{(+)}\\
q_{2s}^{(\tau)} &= q_{2s}^{(-)}F_\tau^{(1)\alpha_2(-)}H_1^{(-)}H_2^{(-)} + q_{2s}^{(+)}F_\tau^{(l)\alpha_2(+)}H_1^{(+)}H_2^{(+)}\\
q_{3s}^{(\tau)} &= q_{3s}^{(-)}F_\tau^{(1)\alpha_3(-)}H_1^{(-)}H_2^{(-)} + q_{3s}^{(+)}F_\tau^{(l)\alpha_3(+)}H_1^{(+)}H_2^{(+)}\\
q_{\mathrm{B}s}^{(\tau)} &= q_{\mathrm{B}s}^{(-)}F_\tau^{(1)\alpha_4(-)}H_1^{(-)}H_2^{(-)} + q_{\mathrm{B}s}^{(+)}F_\tau^{(l)\alpha_4(+)}H_1^{(+)}H_2^{(+)}\\
q_{\mathrm{T}s}^{(\tau)} &= q_{\mathrm{T}s}^{(-)}F_\tau^{(1)\alpha_5(-)}H_1^{(-)}H_2^{(-)} + q_{\mathrm{T}s}^{(+)}F_\tau^{(l)\alpha_5(+)}H_1^{(+)}H_2^{(+)}\\
q_{\mathrm{C}s}^{(\tau)} &= q_{\mathrm{C}s}^{(-)}F_\tau^{(1)\alpha_6(-)}H_1^{(-)}H_2^{(-)} + q_{\mathrm{C}s}^{(+)}F_\tau^{(l)\alpha_6(+)}H_1^{(+)}H_2^{(+)}
\end{aligned} \tag{48}$$

The generalized surface loads in Eq. (48) are expressed in terms of the generalized thickness functions $F_\tau^{(1)\alpha_i(-)}, F_\tau^{(l)\alpha_i(+)}$, evaluated at the top and bottom surfaces. By employing the definitions from Eq. (45)–(48), the extended expression for the generalized loads $q_{1efk}^{(\tau)}, q_{2efk}^{(\tau)}, q_{3efk}^{(\tau)}$ are derived, dependent on the generalized configuration variables $u_1^{(\tau)}, u_2^{(\tau)}, u_3^{(\tau)}$, as shown in the following:

$$\begin{aligned}
q_{1efk}^{(\tau)} &= -\left(k_{1f}^{(-)}F_\eta^{(1)\alpha_1(-)}F_\tau^{(1)\alpha_1(-)}H_1^{(-)}H_2^{(-)} + k_{1f}^{(+)}F_\eta^{(l)\alpha_1(+)}F_\tau^{(l)\alpha_1(+)}H_1^{(+)}H_2^{(+)}\right)u_1^{(\tau)} = -L_{fm1}^{(\tau\eta)\alpha_1\alpha_1}u_1^{(\tau)}\\
q_{2efk}^{(\tau)} &= -\left(k_{2f}^{(-)}F_\eta^{(1)\alpha_2(-)}F_\tau^{(1)\alpha_2(-)}H_1^{(-)}H_2^{(-)} + k_{2f}^{(+)}F_\eta^{(l)\alpha_2(+)}F_\tau^{(l)\alpha_2(+)}H_1^{(+)}H_2^{(+)}\right)u_2^{(\tau)} = -L_{fm2}^{(\tau\eta)\alpha_2\alpha_2}u_2^{(\tau)}\\
q_{3efk}^{(\tau)} &= -\left(\left(k_{3f}^{(-)} - G_f^{(-)}\nabla_{(-)}^2\right)F_\eta^{(1)\alpha_3(-)}F_\tau^{(1)\alpha_3(-)}H_1^{(-)}H_2^{(-)} + \left(k_{3f}^{(+)} - G_f^{(+)}\nabla_{(+)}^2\right)F_\eta^{(l)\alpha_3(+)}F_\tau^{(l)\alpha_3(+)}H_1^{(+)}H_2^{(+)}\right)u_3^{(\tau)} = -L_{fm3}^{(\tau\eta)\alpha_3\alpha_3}u_3^{(\tau)}
\end{aligned} \tag{49}$$

It should be noted that $q_{is}^{(\tau)} = q_i^{(\tau)} + q_{iefk}^{(\tau)}$ with $i = 1,2,3$, while $q_{\alpha s}^{(\tau)} = q_\alpha^{(\tau)}$ for $\alpha = \mathrm{B},\mathrm{T},\mathrm{C}$. For convenience, the generalized surface actions from Eq. (49) are collected for each $\tau = 0,\dots,N+1$ into the vector $\mathbf{q}_{efk}^{(\tau)} = \begin{bmatrix} q_{1efk}^{(\tau)} & q_{2efk}^{(\tau)} & q_{3efk}^{(\tau)} & 0 & 0 & 0 \end{bmatrix}^T$. Similarly, the vector $\mathbf{q}^{(\tau)} = \begin{bmatrix} q_1^{(\tau)} & q_2^{(\tau)} & q_3^{(\tau)} & q_{\mathrm{B}}^{(\tau)} & q_{\mathrm{T}}^{(\tau)} & q_{\mathrm{C}}^{(\tau)} \end{bmatrix}^T$ is conveniently introduced based on the definition in Eq. (48). This allows the total generalized load vector $\mathbf{q}_s^{(\tau)} = \begin{bmatrix} q_{1s}^{(\tau)} & q_{2s}^{(\tau)} & q_{3s}^{(\tau)} & q_{\mathrm{B}s}^{(\tau)} & q_{\mathrm{T}s}^{(\tau)} & q_{\mathrm{C}s}^{(\tau)} \end{bmatrix}^T$ to be expressed as $\mathbf{q}_s^{(\tau)} = \mathbf{q}_{efk}^{(\tau)} + \mathbf{q}^{(\tau)}$. Finally, the reference entropy $\overline{\upeta}^{(k)}$ and chemical potential $\overline{\upmu}^{(k)}$ over the 3D solid are associated with the virtual works δL_{T} and δL_{C}, respectively, which are evaluated using the following expression:

$$\begin{aligned}
\delta L_{\mathrm{T}} &= -\sum_{k=1}^{l}\int_{\zeta_k}^{\zeta_{k+1}}\int_{\alpha_1}\int_{\alpha_2}\overline{\upeta}^{(k)}\delta\Delta\mathrm{T}^{(k)}H_1H_2A_1A_2\,d\alpha_1 d\alpha_2 d\zeta\\
\delta L_{\mathrm{C}} &= -\sum_{k=1}^{l}\int_{\zeta_k}^{\zeta_{k+1}}\int_{\alpha_1}\int_{\alpha_2}\overline{\upmu}^{(k)}\delta\Delta\mathrm{C}^{(k)}H_1H_2A_1A_2\,d\alpha_1 d\alpha_2 d\zeta
\end{aligned} \tag{50}$$

These energy contributions arise because the shell solid is maintained at a given absolute reference temperature T_0 and a specific equilibrium moisture concentration C_∞. Under thermodynamic equilibrium, the integrals in Eq. (50) assume a null value. If the total virtual work is denoted by $\delta L = \delta L_{\mathrm{T}} + \delta L_{\mathrm{C}} + \delta L_s$, the multifield equilibrium configuration of the solid can be determined using the Master Balance principle [25], according to the relation provided below, with $[t_1, t_2]$ representing an arbitrary time interval where $t_1 < t_2$:

$$\int_{t_1}^{t_2}\delta\mathrm{E}\,dt = \int_{t_1}^{t_2}(\delta\Upsilon - \delta L)dt = 0 \tag{51}$$

The balance equations, along with the boundary conditions of the problem, are derived by substituting the expressions from Eq. (35), Eqs. (44) and (50) into the energetic contributions of Eq. (51). By applying the integration by parts rule and performing some mathematical manipulations, the following relations are obtained for an arbitrary $\tau-$th order with $\tau = 0,\dots,N+1$ [25]:

$$\begin{aligned}
&\frac{1}{A_1}\frac{\partial N_1^{(\tau)\alpha_1}}{\partial\alpha_1} + \frac{N_1^{(\tau)\alpha_1}}{A_1A_2}\frac{\partial A_2}{\partial\alpha_1} + \frac{1}{A_2}\frac{\partial N_{21}^{(\tau)\alpha_1}}{\partial\alpha_2} + \frac{N_{21}^{(\tau)\alpha_1}}{A_1A_2}\frac{\partial A_1}{\partial\alpha_2} + \frac{N_{12}^{(\tau)\alpha_1}}{A_1A_2}\frac{\partial A_1}{\partial\alpha_2}\\
&\quad - \frac{N_2^{(\tau)\alpha_1}}{A_1A_2}\frac{\partial A_2}{\partial\alpha_1} + \frac{T_1^{(\tau)\alpha_1}}{R_1} - P_1^{(\tau)\alpha_1} + q_{1s}^{(\tau)} = 0\\
&\frac{1}{A_2}\frac{\partial N_2^{(\tau)\alpha_2}}{\partial\alpha_2} + \frac{N_2^{(\tau)\alpha_2}}{A_1A_2}\frac{\partial A_1}{\partial\alpha_2} + \frac{1}{A_1}\frac{\partial N_{12}^{(\tau)\alpha_2}}{\partial\alpha_1} + \frac{N_{12}^{(\tau)\alpha_2}}{A_1A_2}\frac{\partial A_2}{\partial\alpha_1} + \frac{N_{21}^{(\tau)\alpha_2}}{A_1A_2}\frac{\partial A_2}{\partial\alpha_1}\\
&\quad - \frac{N_1^{(\tau)\alpha_2}}{A_1A_2}\frac{\partial A_1}{\partial\alpha_2} + \frac{T_2^{(\tau)\alpha_2}}{R_2} - P_2^{(\tau)\alpha_2} + q_{2s}^{(\tau)} = 0\\
&\frac{1}{A_1}\frac{\partial T_1^{(\tau)\alpha_3}}{\partial\alpha_1} + \frac{T_1^{(\tau)\alpha_3}}{A_1A_2}\frac{\partial A_2}{\partial\alpha_1} + \frac{1}{A_2}\frac{\partial T_2^{(\tau)\alpha_3}}{\partial\alpha_2} + \frac{T_2^{(\tau)\alpha_3}}{A_1A_2}\frac{\partial A_1}{\partial\alpha_2} - \frac{N_1^{(\tau)\alpha_3}}{R_1} - \frac{N_2^{(\tau)\alpha_3}}{R_2}\\
&\quad - S_3^{(\tau)\alpha_3} + q_{3s}^{(\tau)} = 0\\
&\frac{1}{A_1}\frac{\partial B_1^{(\tau)\alpha_4}}{\partial\alpha_1} + \frac{B_1^{(\tau)\alpha_4}}{A_1A_2}\frac{\partial A_2}{\partial\alpha_1} + \frac{1}{A_2}\frac{\partial B_2^{(\tau)\alpha_4}}{\partial\alpha_2} + \frac{B_2^{(\tau)\alpha_4}}{A_1A_2}\frac{\partial A_1}{\partial\alpha_2} - B_3^{(\tau)\alpha_4} + q_{\mathrm{B}s}^{(\tau)} = 0\\
&\frac{1}{A_1}\frac{\partial H_1^{(\tau)\alpha_5}}{\partial\alpha_1} + \frac{H_1^{(\tau)\alpha_5}}{A_1A_2}\frac{\partial A_2}{\partial\alpha_1} + \frac{1}{A_2}\frac{\partial H_2^{(\tau)\alpha_5}}{\partial\alpha_2} + \frac{H_2^{(\tau)\alpha_5}}{A_1A_2}\frac{\partial A_1}{\partial\alpha_2} - H_3^{(\tau)\alpha_5} + q_{\mathrm{T}s}^{(\tau)} = 0\\
&\frac{1}{A_1}\frac{\partial C_1^{(\tau)\alpha_6}}{\partial\alpha_1} + \frac{C_1^{(\tau)\alpha_6}}{A_1A_2}\frac{\partial A_2}{\partial\alpha_1} + \frac{1}{A_2}\frac{\partial C_2^{(\tau)\alpha_6}}{\partial\alpha_2} + \frac{C_2^{(\tau)\alpha_6}}{A_1A_2}\frac{\partial A_1}{\partial\alpha_2} - C_3^{(\tau)\alpha_6} + q_{\mathrm{C}s}^{(\tau)} = 0
\end{aligned} \tag{52}$$

The previous equations are, therefore, expressed in compact matrix form as follows:

$$\sum_{i=1}^{6}\mathbf{D}_\Omega^{*\alpha_i}\boldsymbol{\Sigma}^{(\tau)\alpha_i} + \mathbf{q}_s^{(\tau)} = \sum_{i=1}^{6}\mathbf{D}_\Omega^{*\alpha_i}\boldsymbol{\Sigma}^{(\tau)\alpha_i} + \mathbf{q}^{(\tau)} + \mathbf{q}_{efk}^{(\tau)} = \mathbf{0} \tag{53}$$

where the balance operators $\mathbf{D}_\Omega^{*\alpha_i}$ with $i = 1,\dots,6$ take the following aspect:

$$
\begin{gathered}
\mathbf{D}_\Omega^{*\alpha_1} = \begin{bmatrix} \overline{\mathbf{D}}_\Omega^{*\alpha_1} & \mathbf{0} & 0 & 0 & \mathbf{0} & \mathbf{0} \\ \mathbf{0} & \mathbf{0} & 0 & 0 & \mathbf{0} & \mathbf{0} \\ \mathbf{0} & \mathbf{0} & 0 & 0 & \mathbf{0} & \mathbf{0} \\ \mathbf{0} & \mathbf{0} & 0 & 0 & \mathbf{0} & \mathbf{0} \\ \mathbf{0} & \mathbf{0} & 0 & 0 & \mathbf{0} & \mathbf{0} \\ \mathbf{0} & \mathbf{0} & 0 & 0 & \mathbf{0} & \mathbf{0} \end{bmatrix}, \quad
\mathbf{D}_\Omega^{*\alpha_2} = \begin{bmatrix} \mathbf{0} & \mathbf{0} & 0 & 0 & \mathbf{0} & \mathbf{0} \\ \overline{\mathbf{D}}_\Omega^{*\alpha_2} & \mathbf{0} & 0 & 0 & \mathbf{0} & \mathbf{0} \\ \mathbf{0} & \mathbf{0} & 0 & 0 & \mathbf{0} & \mathbf{0} \\ \mathbf{0} & \mathbf{0} & 0 & 0 & \mathbf{0} & \mathbf{0} \\ \mathbf{0} & \mathbf{0} & 0 & 0 & \mathbf{0} & \mathbf{0} \\ \mathbf{0} & \mathbf{0} & 0 & 0 & \mathbf{0} & \mathbf{0} \end{bmatrix}, \quad
\mathbf{D}_\Omega^{*\alpha_3} = \begin{bmatrix} \mathbf{0} & \mathbf{0} & 0 & 0 & \mathbf{0} & \mathbf{0} \\ \mathbf{0} & \mathbf{0} & 0 & 0 & \mathbf{0} & \mathbf{0} \\ \overline{\mathbf{D}}_\Omega^{*\alpha_3} & \mathbf{0} & 0 & 0 & \mathbf{0} & \mathbf{0} \\ \mathbf{0} & \mathbf{0} & 0 & 0 & \mathbf{0} & \mathbf{0} \\ \mathbf{0} & \mathbf{0} & 0 & 0 & \mathbf{0} & \mathbf{0} \\ \mathbf{0} & \mathbf{0} & 0 & 0 & \mathbf{0} & \mathbf{0} \end{bmatrix}, \\
\mathbf{D}_\Omega^{*\alpha_4} = \begin{bmatrix} \mathbf{0} & \mathbf{0} & 0 & 0 & \mathbf{0} & \mathbf{0} \\ \mathbf{0} & \mathbf{0} & 0 & 0 & \mathbf{0} & \mathbf{0} \\ \mathbf{0} & \mathbf{0} & 0 & 0 & \mathbf{0} & \mathbf{0} \\ \mathbf{0} & \overline{\mathbf{D}}_\Omega^{*\alpha_4} & 0 & 0 & \mathbf{0} & \mathbf{0} \\ \mathbf{0} & \mathbf{0} & 0 & 0 & \mathbf{0} & \mathbf{0} \\ \mathbf{0} & \mathbf{0} & 0 & 0 & \mathbf{0} & \mathbf{0} \end{bmatrix}, \quad
\mathbf{D}_\Omega^{*\alpha_5} = \begin{bmatrix} \mathbf{0} & \mathbf{0} & 0 & 0 & \mathbf{0} & \mathbf{0} \\ \mathbf{0} & \mathbf{0} & 0 & 0 & \mathbf{0} & \mathbf{0} \\ \mathbf{0} & \mathbf{0} & 0 & 0 & \mathbf{0} & \mathbf{0} \\ \mathbf{0} & \mathbf{0} & 0 & 0 & \mathbf{0} & \mathbf{0} \\ \mathbf{0} & \mathbf{0} & 0 & 0 & \overline{\mathbf{D}}_\Omega^{*\alpha_5} & \mathbf{0} \\ \mathbf{0} & \mathbf{0} & 0 & 0 & \mathbf{0} & \mathbf{0} \end{bmatrix}, \quad
\mathbf{D}_\Omega^{*\alpha_6} = \begin{bmatrix} \mathbf{0} & \mathbf{0} & 0 & 0 & \mathbf{0} & \mathbf{0} \\ \mathbf{0} & \mathbf{0} & 0 & 0 & \mathbf{0} & \mathbf{0} \\ \mathbf{0} & \mathbf{0} & 0 & 0 & \mathbf{0} & \mathbf{0} \\ \mathbf{0} & \mathbf{0} & 0 & 0 & \mathbf{0} & \mathbf{0} \\ \mathbf{0} & \mathbf{0} & 0 & 0 & \mathbf{0} & \mathbf{0} \\ \mathbf{0} & \mathbf{0} & 0 & 0 & \mathbf{0} & \overline{\mathbf{D}}_\Omega^{*\alpha_6} \end{bmatrix}
\end{gathered}
\tag{54}
$$

The sub-operators $\overline{\mathbf{D}}_\Omega^{*\alpha_i}$ with $i = 1, \ldots, 6$ are defined as follows:

$$
\begin{gathered}
\overline{\mathbf{D}}_\Omega^{*\alpha_1} = \left[\frac{1}{A_1}\frac{\partial}{\partial\alpha_1} + \frac{1}{A_1A_2}\frac{\partial A_2}{\partial\alpha_1} \quad -\frac{1}{A_1A_2}\frac{\partial A_2}{\partial\alpha_1} \quad \frac{1}{A_1A_2}\frac{\partial A_1}{\partial\alpha_2} \quad \frac{1}{A_2}\frac{\partial}{\partial\alpha_2} + \frac{1}{A_1A_2}\frac{\partial A_1}{\partial\alpha_2} \quad \frac{1}{R_1} \quad 0 \quad -1 \quad 0 \quad 0 \right] \\
\overline{\mathbf{D}}_\Omega^{*\alpha_2} = \left[-\frac{1}{A_1A_2}\frac{\partial A_1}{\partial\alpha_2} \quad \frac{1}{A_2}\frac{\partial}{\partial\alpha_2} + \frac{1}{A_1A_2}\frac{\partial A_1}{\partial\alpha_2} \quad \frac{1}{A_1}\frac{\partial}{\partial\alpha_1} + \frac{1}{A_1A_2}\frac{\partial A_2}{\partial\alpha_1} \quad \frac{1}{A_1A_2}\frac{\partial A_2}{\partial\alpha_1} \quad 0 \quad \frac{1}{R_2} \quad 0 \quad -1 \quad 0 \right] \\
\overline{\mathbf{D}}_\Omega^{*\alpha_3} = \left[-\frac{1}{R_1} \quad -\frac{1}{R_2} \quad 0 \quad 0 \quad \frac{1}{A_1}\frac{\partial}{\partial\alpha_1} + \frac{1}{A_1A_2}\frac{\partial A_2}{\partial\alpha_1} \quad \frac{1}{A_2}\frac{\partial}{\partial\alpha_2} + \frac{1}{A_1A_2}\frac{\partial A_1}{\partial\alpha_2} \quad 0 \quad 0 \quad -1 \right] \\
\overline{\mathbf{D}}_\Omega^{*\alpha_4} = \overline{\mathbf{D}}_\Omega^{*\alpha_5} = \overline{\mathbf{D}}_\Omega^{*\alpha_6} = \left[\frac{1}{A_1}\frac{\partial}{\partial\alpha_1} + \frac{1}{A_1A_2}\frac{\partial A_2}{\partial\alpha_1} \quad \frac{1}{A_2}\frac{\partial}{\partial\alpha_2} + \frac{1}{A_1A_2}\frac{\partial A_1}{\partial\alpha_2} \quad -1 \right]
\end{gathered}
\tag{55}
$$

From the Master Balance principle in Eq. (51), when the integration by parts rule is applied, some relations are derived which are enforced at the four edges of the rectangular parametric domain $\left[\alpha_1^0, \alpha_1^1\right] \times \left[\alpha_2^0, \alpha_2^1\right]$. In particular, the following set of boundary conditions is obtained for each $\tau = 0, \ldots, N+1$ at $\alpha_1 = \alpha_1^0$ and $\alpha_1 = \alpha_1^1$:

$$
\begin{aligned}
N_1^{(\tau)\alpha_1} &= \overline{N}_1^{(\tau)\alpha_1} \quad \text{or} \quad u_1^{(\tau)} = \overline{u}_1^{(\tau)} \\
N_{12}^{(\tau)\alpha_2} &= \overline{N}_{12}^{(\tau)\alpha_2} \quad \text{or} \quad u_2^{(\tau)} = \overline{u}_2^{(\tau)} \\
T_1^{(\tau)\alpha_3} &= \overline{T}_1^{(\tau)\alpha_3} \quad \text{or} \quad u_3^{(\tau)} = \overline{u}_3^{(\tau)} \\
B_1^{(\tau)\alpha_4} &= \overline{B}_1^{(\tau)\alpha_4} \quad \text{or} \quad \psi^{(\tau)} = \overline{\psi}^{(\tau)} \\
H_1^{(\tau)\alpha_5} &= \overline{H}_1^{(\tau)\alpha_5} \quad \text{or} \quad \xi^{(\tau)} = \overline{\xi}^{(\tau)} \\
C_1^{(\tau)\alpha_6} &= \overline{C}_1^{(\tau)\alpha_6} \quad \text{or} \quad \kappa^{(\tau)} = \overline{\kappa}^{(\tau)}
\end{aligned}
\tag{56}
$$

Similarly, the boundary conditions at $\alpha_2 = \alpha_2^0$ and $\alpha_2 = \alpha_2^1$ can be expressed as follows:

$$
\begin{aligned}
N_{21}^{(\tau)\alpha_1} &= \overline{N}_{21}^{(\tau)\alpha_1} \quad \text{or} \quad u_1^{(\tau)} = \overline{u}_1^{(\tau)} \\
N_2^{(\tau)\alpha_2} &= \overline{N}_2^{(\tau)\alpha_2} \quad \text{or} \quad u_2^{(\tau)} = \overline{u}_2^{(\tau)} \\
T_2^{(\tau)\alpha_3} &= \overline{T}_2^{(\tau)\alpha_3} \quad \text{or} \quad u_3^{(\tau)} = \overline{u}_3^{(\tau)} \\
B_2^{(\tau)\alpha_4} &= \overline{B}_2^{(\tau)\alpha_4} \quad \text{or} \quad \psi^{(\tau)} = \overline{\psi}^{(\tau)} \\
H_2^{(\tau)\alpha_5} &= \overline{H}_2^{(\tau)\alpha_5} \quad \text{or} \quad \xi^{(\tau)} = \overline{\xi}^{(\tau)} \\
C_2^{(\tau)\alpha_6} &= \overline{C}_2^{(\tau)\alpha_6} \quad \text{or} \quad \kappa^{(\tau)} = \overline{\kappa}^{(\tau)}
\end{aligned}
\tag{57}
$$

In the previous relations, the quantities $\overline{u}_1^{(\tau)}, \overline{u}_2^{(\tau)}, \overline{u}_3^{(\tau)}, \overline{\psi}^{(\tau)}, \overline{\xi}^{(\tau)}, \overline{\kappa}^{(\tau)}$ refer to prescribed values of configuration variables, while $\overline{N}_1^{(\tau)\alpha_1}, \overline{N}_{12}^{(\tau)\alpha_2}, \overline{T}_1^{(\tau)\alpha_3}, \overline{B}_1^{(\tau)\alpha_4}, \overline{H}_1^{(\tau)\alpha_5}, \overline{C}_1^{(\tau)\alpha_6}$ and $\overline{N}_{21}^{(\tau)\alpha_1}, \overline{N}_2^{(\tau)\alpha_2}, \overline{T}_2^{(\tau)\alpha_3}, \overline{B}_2^{(\tau)\alpha_4}, \overline{H}_2^{(\tau)\alpha_5}, \overline{C}_2^{(\tau)\alpha_6}$ are specific values assumed by the higher-order multifield secondary variables, as defined in Eq. (38), enforced at the edges of the 2D parametric domain. As a particular case of Eqs. (56) and (57), the Simply-supported (S) boundary conditions set is defined, for an arbitrary $\tau = 0, \ldots, N+1$, according to the relations reported below:

$$\begin{aligned}
N_1^{(\tau)\alpha_1} = 0, \quad u_2^{(\tau)} = u_3^{(\tau)} = \psi^{(\tau)} = \xi^{(\tau)} = \kappa^{(\tau)} = 0 \quad \text{at} \quad \alpha_1 = \alpha_1^0 \ \text{and} \ \alpha_1 = \alpha_1^1 \\
N_2^{(\tau)\alpha_2} = 0, \quad u_1^{(\tau)} = u_3^{(\tau)} = \psi^{(\tau)} = \xi^{(\tau)} = \kappa^{(\tau)} = 0 \quad \text{at} \quad \alpha_2 = \alpha_2^0 \ \text{and} \ \alpha_2 = \alpha_2^1
\end{aligned} \tag{58}$$

Finally, the generalized constitutive relationship of Eq. (42), which expresses the secondary variable vector in terms of the configuration variables of the model, is introduced into Eq. (53) to derive the higher-order fundamental equations for the hygro-thermo-magneto-mechanical problem. These relations assume the following compact matrix form:

$$\sum_{\eta=0}^{N+1} \bar{\mathbf{L}}^{(\tau\eta)} \boldsymbol{\delta}^{(\eta)} + \mathbf{q}^{(\tau)} = \sum_{\eta=0}^{N+1} \mathbf{L}^{(\tau\eta)} \boldsymbol{\delta}^{(\eta)} + \mathbf{q}_{efk}^{(\tau)} + \mathbf{q}_{s}^{(\tau)} = \sum_{\eta=0}^{N+1} \left(\mathbf{L}^{(\tau\eta)} - \mathbf{L}_{fm}^{(\tau\eta)} \right) \boldsymbol{\delta}^{(\eta)} + \mathbf{q}_{s}^{(\tau)} = \mathbf{0} \tag{59}$$

The matrix $\bar{\mathbf{L}}^{(\tau\eta)}$ associated with an arbitrary kinematic expansion order $\tau,\eta = 0,\ldots,N+1$, is evaluated within the rectangular parametric domain as follows:

$$\bar{\mathbf{L}}^{(\tau\eta)} = \begin{bmatrix}
L_{11}^{(\tau\eta)\alpha_1\alpha_1} - L_{fm1}^{(\tau\eta)\alpha_1\alpha_1} & L_{12}^{(\tau\eta)\alpha_1\alpha_2} & L_{13}^{(\tau\eta)\alpha_1\alpha_3} & L_{14}^{(\tau\eta)\alpha_1\alpha_4} & L_{15}^{(\tau\eta)\alpha_1\alpha_5} & L_{16}^{(\tau\eta)\alpha_1\alpha_6} \\
L_{21}^{(\tau\eta)\alpha_2\alpha_1} & L_{22}^{(\tau\eta)\alpha_2\alpha_2} - L_{fm2}^{(\tau\eta)\alpha_2\alpha_2} & L_{23}^{(\tau\eta)\alpha_2\alpha_3} & L_{24}^{(\tau\eta)\alpha_2\alpha_4} & L_{25}^{(\tau\eta)\alpha_2\alpha_5} & L_{26}^{(\tau\eta)\alpha_2\alpha_6} \\
L_{31}^{(\tau\eta)\alpha_3\alpha_1} & L_{32}^{(\tau\eta)\alpha_3\alpha_2} & L_{33}^{(\tau\eta)\alpha_3\alpha_3} - L_{fm3}^{(\tau\eta)\alpha_3\alpha_3} & L_{34}^{(\tau\eta)\alpha_3\alpha_4} & L_{35}^{(\tau\eta)\alpha_3\alpha_5} & L_{36}^{(\tau\eta)\alpha_3\alpha_6} \\
L_{41}^{(\tau\eta)\alpha_4\alpha_1} & L_{42}^{(\tau\eta)\alpha_4\alpha_2} & L_{43}^{(\tau\eta)\alpha_4\alpha_3} & L_{44}^{(\tau\eta)\alpha_4\alpha_4} & L_{45}^{(\tau\eta)\alpha_4\alpha_5} & L_{46}^{(\tau\eta)\alpha_4\alpha_6} \\
0 & 0 & 0 & 0 & L_{55}^{(\tau\eta)\alpha_5\alpha_5} & L_{56}^{(\tau\eta)\alpha_5\alpha_6} \\
0 & 0 & 0 & 0 & L_{65}^{(\tau\eta)\alpha_6\alpha_5} & L_{66}^{(\tau\eta)\alpha_6\alpha_6}
\end{bmatrix} =$$
$$= \begin{bmatrix}
\bar{\mathbf{D}}_\Omega^{*\alpha_1} \mathbf{A}_{\varepsilon\varepsilon}^{(\tau\eta)\alpha_1\alpha_1} \bar{\mathbf{D}}_\Omega^{\alpha_1} - L_{fm1}^{(\tau\eta)\alpha_1\alpha_1} & \bar{\mathbf{D}}_\Omega^{*\alpha_1} \mathbf{A}_{\varepsilon\varepsilon}^{(\tau\eta)\alpha_1\alpha_2} \bar{\mathbf{D}}_\Omega^{\alpha_2} & \bar{\mathbf{D}}_\Omega^{*\alpha_1} \mathbf{A}_{\varepsilon\varepsilon}^{(\tau\eta)\alpha_1\alpha_3} \bar{\mathbf{D}}_\Omega^{\alpha_3} & \bar{\mathbf{D}}_\Omega^{*\alpha_1} \mathbf{A}_{\varepsilon\psi}^{(\tau\eta)\alpha_1\alpha_4} \bar{\mathbf{D}}_\Omega^{\alpha_4} & \bar{\mathbf{D}}_\Omega^{*\alpha_1} \mathbf{A}_{\varepsilon\mathrm{T}}^{(\tau\eta)\alpha_1\alpha_5} \bar{\mathbf{D}}_\Omega^{\alpha_5} & \bar{\mathbf{D}}_\Omega^{*\alpha_1} \mathbf{A}_{\varepsilon\mathrm{C}}^{(\tau\eta)\alpha_1\alpha_6} \bar{\mathbf{D}}_\Omega^{\alpha_6} \\
\bar{\mathbf{D}}_\Omega^{*\alpha_2} \mathbf{A}_{\varepsilon\varepsilon}^{(\tau\eta)\alpha_2\alpha_1} \bar{\mathbf{D}}_\Omega^{\alpha_1} & \bar{\mathbf{D}}_\Omega^{*\alpha_2} \mathbf{A}_{\varepsilon\varepsilon}^{(\tau\eta)\alpha_2\alpha_2} \bar{\mathbf{D}}_\Omega^{\alpha_2} - L_{fm2}^{(\tau\eta)\alpha_2\alpha_2} & \bar{\mathbf{D}}_\Omega^{*\alpha_2} \mathbf{A}_{\varepsilon\varepsilon}^{(\tau\eta)\alpha_2\alpha_3} \bar{\mathbf{D}}_\Omega^{\alpha_3} & \bar{\mathbf{D}}_\Omega^{*\alpha_2} \mathbf{A}_{\varepsilon\psi}^{(\tau\eta)\alpha_2\alpha_4} \bar{\mathbf{D}}_\Omega^{\alpha_4} & \bar{\mathbf{D}}_\Omega^{*\alpha_2} \mathbf{A}_{\varepsilon\mathrm{T}}^{(\tau\eta)\alpha_2\alpha_5} \bar{\mathbf{D}}_\Omega^{\alpha_5} & \bar{\mathbf{D}}_\Omega^{*\alpha_2} \mathbf{A}_{\varepsilon\mathrm{C}}^{(\tau\eta)\alpha_2\alpha_6} \bar{\mathbf{D}}_\Omega^{\alpha_6} \\
\bar{\mathbf{D}}_\Omega^{*\alpha_3} \mathbf{A}_{\varepsilon\varepsilon}^{(\tau\eta)\alpha_3\alpha_1} \bar{\mathbf{D}}_\Omega^{\alpha_1} & \bar{\mathbf{D}}_\Omega^{*\alpha_3} \mathbf{A}_{\varepsilon\varepsilon}^{(\tau\eta)\alpha_3\alpha_2} \bar{\mathbf{D}}_\Omega^{\alpha_2} & \bar{\mathbf{D}}_\Omega^{*\alpha_3} \mathbf{A}_{\varepsilon\varepsilon}^{(\tau\eta)\alpha_3\alpha_3} \bar{\mathbf{D}}_\Omega^{\alpha_3} - L_{fm3}^{(\tau\eta)\alpha_3\alpha_3} & \bar{\mathbf{D}}_\Omega^{*\alpha_3} \mathbf{A}_{\varepsilon\psi}^{(\tau\eta)\alpha_3\alpha_4} \bar{\mathbf{D}}_\Omega^{\alpha_4} & \bar{\mathbf{D}}_\Omega^{*\alpha_3} \mathbf{A}_{\varepsilon\mathrm{T}}^{(\tau\eta)\alpha_3\alpha_5} \bar{\mathbf{D}}_\Omega^{\alpha_5} & \bar{\mathbf{D}}_\Omega^{*\alpha_3} \mathbf{A}_{\varepsilon\mathrm{C}}^{(\tau\eta)\alpha_3\alpha_6} \bar{\mathbf{D}}_\Omega^{\alpha_6} \\
\bar{\mathbf{D}}_\Omega^{*\alpha_4} \mathbf{A}_{\psi\varepsilon}^{(\tau\eta)\alpha_4\alpha_1} \bar{\mathbf{D}}_\Omega^{\alpha_1} & \bar{\mathbf{D}}_\Omega^{*\alpha_4} \mathbf{A}_{\psi\varepsilon}^{(\tau\eta)\alpha_4\alpha_2} \bar{\mathbf{D}}_\Omega^{\alpha_2} & \bar{\mathbf{D}}_\Omega^{*\alpha_4} \mathbf{A}_{\psi\varepsilon}^{(\tau\eta)\alpha_4\alpha_3} \bar{\mathbf{D}}_\Omega^{\alpha_3} & \bar{\mathbf{D}}_\Omega^{*\alpha_4} \mathbf{A}_{\psi\psi}^{(\tau\eta)\alpha_4\alpha_4} \bar{\mathbf{D}}_\Omega^{\alpha_4} & \bar{\mathbf{D}}_\Omega^{*\alpha_4} \mathbf{A}_{\psi\mathrm{T}}^{(\tau\eta)\alpha_4\alpha_5} \bar{\mathbf{D}}_\Omega^{\alpha_5} & \bar{\mathbf{D}}_\Omega^{*\alpha_4} \mathbf{A}_{\psi\mathrm{C}}^{(\tau\eta)\alpha_4\alpha_6} \bar{\mathbf{D}}_\Omega^{\alpha_6} \\
0 & 0 & 0 & 0 & \bar{\mathbf{D}}_\Omega^{*\alpha_5} \mathbf{A}_{\theta\theta}^{(\tau\eta)\alpha_5\alpha_5} \bar{\mathbf{D}}_\Omega^{\alpha_5} & \bar{\mathbf{D}}_\Omega^{*\alpha_5} \mathbf{A}_{\theta\lambda}^{(\tau\eta)\alpha_5\alpha_6} \bar{\mathbf{D}}_\Omega^{\alpha_6} \\
0 & 0 & 0 & 0 & \bar{\mathbf{D}}_\Omega^{*\alpha_6} \mathbf{A}_{\lambda\theta}^{(\tau\eta)\alpha_6\alpha_5} \bar{\mathbf{D}}_\Omega^{\alpha_5} & \bar{\mathbf{D}}_\Omega^{*\alpha_6} \mathbf{A}_{\lambda\lambda}^{(\tau\eta)\alpha_6\alpha_6} \bar{\mathbf{D}}_\Omega^{\alpha_6}
\end{bmatrix} \tag{60}$$

Note that the terms $L_{fm1}^{(\tau\eta)\alpha_1\alpha_1}, L_{fm2}^{(\tau\eta)\alpha_2\alpha_2}, L_{fm3}^{(\tau\eta)\alpha_3\alpha_3}$ consider the effects of the Winkler-Pasternak foundation, as defined in Eq. (49) for each $\tau,\eta-$th kinematic expansion order. At this point, a semi-analytical solution of the fundamental Eq. (59) is derived according to the Navier method [25]. To this end, a double trigonometric expansion of each unknown field variable is assumed, following the expressions reported below:

$$
\begin{aligned}
u_1^{(\tau)}(s_1,s_2) &= \sum_{n=1}^{\tilde{N}}\sum_{m=1}^{\tilde{M}} \mathrm{U}_{1nm}^{(\tau)}\cos\left(\frac{n\pi}{L_1}s_1\right)\sin\left(\frac{m\pi}{L_2}s_2\right)\\
u_2^{(\tau)}(s_1,s_2) &= \sum_{n=1}^{\tilde{N}}\sum_{m=1}^{\tilde{M}} \mathrm{U}_{2nm}^{(\tau)}\sin\left(\frac{n\pi}{L_1}s_1\right)\cos\left(\frac{m\pi}{L_2}s_2\right)\\
u_3^{(\tau)}(s_1,s_2) &= \sum_{n=1}^{\tilde{N}}\sum_{m=1}^{\tilde{M}} \mathrm{U}_{3nm}^{(\tau)}\sin\left(\frac{n\pi}{L_1}s_1\right)\sin\left(\frac{m\pi}{L_2}s_2\right)\\
\psi^{(\tau)}(s_1,s_2) &= \sum_{n=1}^{\tilde{N}}\sum_{m=1}^{\tilde{M}} \Psi_{nm}^{(\tau)}\sin\left(\frac{n\pi}{L_1}s_1\right)\sin\left(\frac{m\pi}{L_2}s_2\right)\\
\xi^{(\tau)}(s_1,s_2) &= \sum_{n=1}^{\tilde{N}}\sum_{m=1}^{\tilde{M}} \Xi_{nm}^{(\tau)}\sin\left(\frac{n\pi}{L_1}s_1\right)\sin\left(\frac{m\pi}{L_2}s_2\right)\\
\kappa^{(\tau)}(s_1,s_2) &= \sum_{n=1}^{\tilde{N}}\sum_{m=1}^{\tilde{M}} \mathrm{K}_{nm}^{(\tau)}\sin\left(\frac{n\pi}{L_1}s_1\right)\sin\left(\frac{m\pi}{L_2}s_2\right)
\end{aligned}
\tag{61}
$$

with $\widetilde{N} = \widetilde{M} = +\infty$. Note that in the previous relations, the solution is expressed in terms of the curvilinear coordinates $s_i = s_1, s_2$ along α_1, α_2, which are defined in the closed interval $\left[s_i^0, s_i^1\right]$ for $i = 1,2$, with $L_i = s_i^1 - s_i^0$ being the length of the physical domain along α_i. Furthermore, the quantities $\mathrm{U}_{1nm}^{(\tau)}, \mathrm{U}_{2nm}^{(\tau)}, \mathrm{U}_{3nm}^{(\tau)}, \Psi_{nm}^{(\tau)}, \Xi_{nm}^{(\tau)}, \mathrm{K}_{nm}^{(\tau)}$ with $n = 1,\dots,\widetilde{N}$ and $m = 1,\dots,\widetilde{M}$ introduced for any $\tau = 0,\dots,N+1$, denote the amplitude of the configuration variables distribution along the physical domain. These quantities are conveniently arranged into the vector $\mathbf{U}_{nm}^{(\eta)} = \begin{bmatrix} \mathrm{U}_{1nm}^{(\tau)} & \mathrm{U}_{2nm}^{(\tau)} & \mathrm{U}_{3nm}^{(\tau)} & \Psi_{nm}^{(\tau)} & \Xi_{nm}^{(\tau)} & \mathrm{K}_{nm}^{(\tau)} \end{bmatrix}^T$. Similarly, generalized surface loads are expanded as follows [25]:

$$
\begin{aligned}
q_1^{(\tau)}(s_1,s_2) &= \sum_{n=1}^{\tilde{N}}\sum_{m=1}^{\tilde{M}} Q_{1snm}^{(\tau)}\cos\left(\frac{n\pi}{L_1}s_1\right)\sin\left(\frac{m\pi}{L_2}s_2\right)\\
q_2^{(\tau)}(s_1,s_2) &= \sum_{n=1}^{\tilde{N}}\sum_{m=1}^{\tilde{M}} Q_{2snm}^{(\tau)}\sin\left(\frac{n\pi}{L_1}s_1\right)\cos\left(\frac{m\pi}{L_2}s_2\right)\\
q_3^{(\tau)}(s_1,s_2) &= \sum_{n=1}^{\tilde{N}}\sum_{m=1}^{\tilde{M}} Q_{3snm}^{(\tau)}\sin\left(\frac{n\pi}{L_1}s_1\right)\sin\left(\frac{m\pi}{L_2}s_2\right)\\
q_{\mathrm{B}}^{(\tau)}(s_1,s_2) &= \sum_{n=1}^{\tilde{N}}\sum_{m=1}^{\tilde{M}} Q_{\mathrm{B}snm}^{(\tau)}\sin\left(\frac{n\pi}{L_1}s_1\right)\sin\left(\frac{m\pi}{L_2}s_2\right)\\
q_{\mathrm{T}}^{(\tau)}(s_1,s_2) &= \sum_{n=1}^{\tilde{N}}\sum_{m=1}^{\tilde{M}} Q_{\mathrm{T}snm}^{(\tau)}\sin\left(\frac{n\pi}{L_1}s_1\right)\sin\left(\frac{m\pi}{L_2}s_2\right)\\
q_{\mathrm{C}}^{(\tau)}(s_1,s_2) &= \sum_{n=1}^{\tilde{N}}\sum_{m=1}^{\tilde{M}} Q_{\mathrm{C}snm}^{(\tau)}\sin\left(\frac{n\pi}{L_1}s_1\right)\sin\left(\frac{m\pi}{L_2}s_2\right)
\end{aligned}
\tag{62}
$$

where the corresponding wave amplitudes are collected into the vector $\mathbf{Q}_{snm}^{(\tau)} = \begin{bmatrix} Q_{1snm}^{(\tau)} & Q_{2snm}^{(\tau)} & Q_{3snm}^{(\tau)} & Q_{\mathrm{B}snm}^{(\tau)} & Q_{\mathrm{T}snm}^{(\tau)} & Q_{\mathrm{C}snm}^{(\tau)} \end{bmatrix}^T$, defined for any wave number $n = 1,\dots,\widetilde{N}$ and $m = 1,\dots,\widetilde{M}$ at a given $\tau = 0,\dots,N+1$. These amplitudes, associated with generalized loads on the reference surface, are derived from the trigonometric expansion of the multifield surface loads applied at the top and bottom surfaces of the doubly-curved 3D solid. If $Q_{\alpha snm}^{(-)}$ and $Q_{\alpha snm}^{(+)}$ with $\alpha = 1,2,3,\mathrm{B},\mathrm{T},\mathrm{C}$ are the wave amplitudes of these external surface loads, the following expressions are derived for the generalized load amplitudes $Q_{\alpha snm}^{(\tau)}$ by using Eq. (48):

$$
\begin{aligned}
Q_{1snm}^{(\tau)} &= Q_{1snm}^{(-)}F_\tau^{(1)\alpha_1(-)}H_1^{(-)}H_2^{(-)} + Q_{1snm}^{(+)}F_\tau^{(l)\alpha_1(+)}H_1^{(+)}H_2^{(+)}\\
Q_{2snm}^{(\tau)} &= Q_{2snm}^{(-)}F_\tau^{(1)\alpha_2(-)}H_1^{(-)}H_2^{(-)} + Q_{2snm}^{(+)}F_\tau^{(l)\alpha_2(+)}H_1^{(+)}H_2^{(+)}\\
Q_{3snm}^{(\tau)} &= Q_{3snm}^{(-)}F_\tau^{(1)\alpha_3(-)}H_1^{(-)}H_2^{(-)} + Q_{3snm}^{(+)}F_\tau^{(l)\alpha_3(+)}H_1^{(+)}H_2^{(+)}\\
Q_{\mathrm{B}snm}^{(\tau)} &= Q_{\mathrm{B}snm}^{(-)}F_\tau^{(1)\alpha_4(-)}H_1^{(-)}H_2^{(-)} + Q_{\mathrm{B}snm}^{(+)}F_\tau^{(l)\alpha_4(+)}H_1^{(+)}H_2^{(+)}\\
Q_{\mathrm{T}snm}^{(\tau)} &= Q_{\mathrm{T}snm}^{(-)}F_\tau^{(1)\alpha_5(-)}H_1^{(-)}H_2^{(-)} + Q_{\mathrm{T}snm}^{(+)}F_\tau^{(l)\alpha_5(+)}H_1^{(+)}H_2^{(+)}\\
Q_{\mathrm{C}snm}^{(\tau)} &= Q_{\mathrm{C}snm}^{(-)}F_\tau^{(1)\alpha_6(-)}H_1^{(-)}H_2^{(-)} + Q_{\mathrm{C}snm}^{(+)}F_\tau^{(l)\alpha_6(+)}H_1^{(+)}H_2^{(+)}
\end{aligned}
\tag{63}
$$

The quantities $Q_{\alpha snm}^{(-)}$ and $Q_{\alpha snm}^{(+)}$, introduced for each n,m, are obtained from the double trigonometric expansion of surface loads directly applied at the top and bottom surfaces of the 3D solid, as shown below:

$$
\begin{aligned}
q_1^{(\pm)}(s_1,s_2) &= \sum_{n=1}^{\tilde{N}}\sum_{m=1}^{\tilde{M}} Q_{1snm}^{(\pm)}\cos\left(\frac{n\pi}{L_1}s_1\right)\sin\left(\frac{m\pi}{L_2}s_2\right)\\
q_2^{(\pm)}(s_1,s_2) &= \sum_{n=1}^{\tilde{N}}\sum_{m=1}^{\tilde{M}} Q_{2snm}^{(\pm)}\sin\left(\frac{n\pi}{L_1}s_1\right)\cos\left(\frac{m\pi}{L_2}s_2\right)\\
q_3^{(\pm)}(s_1,s_2) &= \sum_{n=1}^{\tilde{N}}\sum_{m=1}^{\tilde{M}} Q_{3snm}^{(\pm)}\sin\left(\frac{n\pi}{L_1}s_1\right)\sin\left(\frac{m\pi}{L_2}s_2\right)\\
q_{\mathrm{B}}^{(\pm)}(s_1,s_2) &= \sum_{n=1}^{\tilde{N}}\sum_{m=1}^{\tilde{M}} Q_{\mathrm{B}snm}^{(\pm)}\sin\left(\frac{n\pi}{L_1}s_1\right)\sin\left(\frac{m\pi}{L_2}s_2\right)\\
q_{\mathrm{T}}^{(\pm)}(s_1,s_2) &= \sum_{n=1}^{\tilde{N}}\sum_{m=1}^{\tilde{M}} Q_{\mathrm{T}snm}^{(\pm)}\sin\left(\frac{n\pi}{L_1}s_1\right)\sin\left(\frac{m\pi}{L_2}s_2\right)\\
q_{\mathrm{C}}^{(\pm)}(s_1,s_2) &= \sum_{n=1}^{\tilde{N}}\sum_{m=1}^{\tilde{M}} Q_{\mathrm{C}snm}^{(\pm)}\sin\left(\frac{n\pi}{L_1}s_1\right)\sin\left(\frac{m\pi}{L_2}s_2\right)
\end{aligned}
\tag{64}
$$

In the same way, it is useful to introduce the relation reported below, which contains the double trigonometric distribution of unknown configuration variables at the top and bottom surfaces. This relation can be enforced on the panel while ensuring the boundary conditions at the lateral surfaces. One gets for $\widetilde{N} = \widetilde{M} = 1$:

$$
\begin{aligned}
U_1^{(\pm)}(s_1,s_2) &= \sum_{n=1}^{\tilde{N}}\sum_{m=1}^{\tilde{M}} \overline{U}_{1s}^{(\pm)}\cos\left(\frac{n\pi}{L_1}s_1\right)\sin\left(\frac{m\pi}{L_2}s_2\right)\\
U_2^{(\pm)}(s_1,s_2) &= \sum_{n=1}^{\tilde{N}}\sum_{m=1}^{\tilde{M}} \overline{U}_{2s}^{(\pm)}\sin\left(\frac{n\pi}{L_1}s_1\right)\cos\left(\frac{m\pi}{L_2}s_2\right)\\
U_3^{(\pm)}(s_1,s_2) &= \sum_{n=1}^{\tilde{N}}\sum_{m=1}^{\tilde{M}} \overline{U}_{3s}^{(\pm)}\sin\left(\frac{n\pi}{L_1}s_1\right)\sin\left(\frac{m\pi}{L_2}s_2\right)\\
\Delta\psi^{(\pm)}(s_1,s_2) &= \sum_{n=1}^{\tilde{N}}\sum_{m=1}^{\tilde{M}} \Delta\overline{\Psi}_s^{(\pm)}\sin\left(\frac{n\pi}{L_1}s_1\right)\sin\left(\frac{m\pi}{L_2}s_2\right)\\
\Delta\mathrm{T}^{(\pm)}(s_1,s_2) &= \sum_{n=1}^{\tilde{N}}\sum_{m=1}^{\tilde{M}} \Delta\overline{\mathrm{T}}_s^{(\pm)}\sin\left(\frac{n\pi}{L_1}s_1\right)\sin\left(\frac{m\pi}{L_2}s_2\right)\\
\Delta\mathrm{C}^{(\pm)}(s_1,s_2) &= \sum_{n=1}^{\tilde{N}}\sum_{m=1}^{\tilde{M}} \Delta\overline{\mathrm{C}}_s^{(\pm)}\sin\left(\frac{n\pi}{L_1}s_1\right)\sin\left(\frac{m\pi}{L_2}s_2\right)
\end{aligned}
\tag{65}
$$

Once Eqs. (61) and (62) are introduced into Eq. (59), a closed-form solution is derived for an arbitrary n,m and $\tau = 0,\dots,N+1$ by introducing some geometric and material assumptions within the model. More specifically, a uniform value of curvatures and Lamé parameters is assumed throughout the entire parametric domain. In other words, the following relation is considered:

$$\begin{aligned} R_i = \mathrm{cost} \Rightarrow \frac{\partial^{n+m} R_i}{\partial s_1^n \partial s_2^m} = 0 \\ A_i = \mathrm{cost} \Rightarrow \frac{\partial^{n+m} A_i}{\partial s_1^n \partial s_2^m} = 0 \end{aligned} \tag{66}$$

Under these assumptions, three different geometries are selected for the analysis, namely a shallow spherical shell, a cylindrical panel, and a rectangular plate. Thus, the curvilinear coordinates s_1, s_2, introduced previously in their infinitesimal form, can be evaluated for a spherical panel as follows, along with the parametric lengths L_1, L_2:

$$\begin{aligned} s_1 = R(\varphi - \varphi_0) \quad &\Rightarrow L_1 = s_1^1 - s_1^0 = R(\varphi_1 - \varphi_0) \\ s_2 = R(\vartheta - \vartheta_0) \quad &\Rightarrow L_2 = s_2^1 - s_2^0 = R(\vartheta_1 - \vartheta_0) \end{aligned} \tag{67}$$

In the previous relation, the generalized coordinates α_1, α_2 vary within the rectangular parametric interval $\left[\alpha_1^0, \alpha_1^1\right] \times \left[\alpha_2^0, \alpha_2^1\right] = \left[\varphi_1^0, \varphi_1^1\right] \times \left[\vartheta_2^0, \vartheta_2^1\right]$. In the case of a circular cylinder with the generatrix along α_1 and the directrix along α_2, the definitions $s_1 = R(\varphi - \varphi_0)$ and $s_2 = y$ should be considered, and therefore the lengths in Eq. (67) are evaluated as $L_1 = s_1^1 - s_1^0 = R(\varphi_1 - \varphi_0)$ and $L_2 = s_2^1 - s_2^0$. On the other hand, if the generatrix is oriented along α_2 and the directrix identifies the α_1 principal direction, the relations $s_1 = y, s_2 = R(\vartheta - \vartheta_0)$ and $L_1 = s_1^1 - s_1^0, L_2 = s_2^1 - s_2^0 = R(\vartheta_1 - \vartheta_0)$ are considered. Finally, for a rectangular plate, with null curvature, the lengths quantities L_1, L_2 are the physical dimensions of the plate, and are evaluated as $L_1 = s_1^1 - s_1^0$, $L_2 = s_2^1 - s_2^0$, since the coordinates are defined as $s_1 = x, s_2 = y$. On the other hand, the Laplacian operator $\nabla^2_{(\pm)}$ of Eq. (46) is simplified under the assumptions of Eq. (66). Finally, a cross-ply constitutive relationship is assumed for the laminate, which means that the orthotropic layers are considered with the orientation angle equal to 0 or $\pm\pi/2$. The homogenized constitutive properties are derived using the analytical procedure detailed in Appendix 1. The following 3D matrices are considered for Eq. (21):

$$\overline{\boldsymbol{\Gamma}}_{\mathrm{C}}^{(k)} = \begin{bmatrix} \overline{C}_{11}^{(k)} & \overline{C}_{12}^{(k)} & 0 & 0 & 0 & \overline{C}_{13}^{(k)} \\ \overline{C}_{12}^{(k)} & \overline{C}_{22}^{(k)} & 0 & 0 & 0 & \overline{C}_{23}^{(k)} \\ 0 & 0 & \overline{C}_{66}^{(k)} & 0 & 0 & 0 \\ 0 & 0 & 0 & \overline{C}_{44}^{(k)} & 0 & 0 \\ 0 & 0 & 0 & 0 & \overline{C}_{55}^{(k)} & 0 \\ \overline{C}_{13}^{(k)} & \overline{C}_{23}^{(k)} & 0 & 0 & 0 & \overline{C}_{33}^{(k)} \end{bmatrix}$$

$$\overline{\boldsymbol{\Gamma}}_{\mathrm{M}}^{(k)} = \begin{bmatrix} \overline{m}_{11}^{(k)} & 0 & 0 \\ 0 & \overline{m}_{22}^{(k)} & 0 \\ 0 & 0 & \overline{m}_{33}^{(k)} \end{bmatrix}$$

$$\overline{\boldsymbol{\Gamma}}_{\mathrm{Q}}^{(k)} = \begin{bmatrix} 0 & 0 & 0 & \overline{q}_{14}^{(k)} & 0 & 0 \\ 0 & 0 & 0 & 0 & \overline{q}_{25}^{(k)} & 0 \\ \overline{q}_{31}^{(k)} & \overline{q}_{32}^{(k)} & 0 & 0 & 0 & \overline{q}_{33}^{(k)} \end{bmatrix}$$

$$\overline{\boldsymbol{\Gamma}}_{\mathrm{z}}^{(k)} = \begin{bmatrix} \overline{z}_{11}^{(k)} & \overline{z}_{22}^{(k)} & 0 & 0 & 0 & \overline{z}_{33}^{(k)} \end{bmatrix} \overline{\boldsymbol{\Gamma}}_{\mathrm{e}}^{(k)} = \begin{bmatrix} \overline{e}_{11}^{(k)} & \overline{e}_{22}^{(k)} & 0 & 0 & 0 & \overline{e}_{33}^{(k)} \end{bmatrix}$$

$$\overline{\boldsymbol{\Gamma}}_{\mathrm{w}}^{(k)} = \begin{bmatrix} 0 & 0 & \overline{w}_{33}^{(k)} \end{bmatrix}, \quad \overline{\boldsymbol{\Gamma}}_{\mathrm{f}}^{(k)} = \begin{bmatrix} 0 & 0 & \overline{f}_{33}^{(k)} \end{bmatrix}$$

$$\overline{\boldsymbol{\Gamma}}_{\mathrm{K}}^{(k)} = \begin{bmatrix} \overline{k}_{11}^{(k)} & 0 & 0 \\ 0 & \overline{k}_{22}^{(k)} & 0 \\ 0 & 0 & \overline{k}_{33}^{(k)} \end{bmatrix}, \quad \overline{\boldsymbol{\Gamma}}_{\mathrm{Y}}^{(k)} = \begin{bmatrix} \overline{y}_{11}^{(k)} & 0 & 0 \\ 0 & \overline{y}_{22}^{(k)} & 0 \\ 0 & 0 & \overline{y}_{33}^{(k)} \end{bmatrix}$$

$$\overline{\boldsymbol{\Gamma}}_{\mathrm{X}}^{(k)} = \begin{bmatrix} \overline{x}_{11}^{(k)} & 0 & 0 \\ 0 & \overline{x}_{22}^{(k)} & 0 \\ 0 & 0 & \overline{x}_{33}^{(k)} \end{bmatrix}, \quad \overline{\boldsymbol{\Gamma}}_{\mathrm{S}}^{(k)} = \begin{bmatrix} \overline{s}_{11}^{(k)} & 0 & 0 \\ 0 & \overline{s}_{22}^{(k)} & 0 \\ 0 & 0 & \overline{s}_{33}^{(k)} \end{bmatrix}$$

$$\overline{\boldsymbol{\Gamma}}_{\mathrm{TT}}^{(k)} = \overline{\xi}_{11}^{(k)}, \quad \overline{\boldsymbol{\Gamma}}_{\mathrm{TC}}^{(k)} = \overline{\xi}_{12}^{(k)}, \quad \overline{\boldsymbol{\Gamma}}_{\mathrm{CC}}^{(k)} = \overline{\xi}_{22}^{(k)} \tag{68}$$

Once the geometric, material, and kinematic relations are introduced into the fundamental governing equations (59), the following relation is obtained, where the unknown variables are collected, for each $n = 1, \ldots, \widetilde{N}$ and $m = 1, \ldots, \widetilde{M}$, into the vector $\mathbf{U}_{nm}^{(\eta)}$:

$$\sum_{n=1}^{\tilde{N}} \sum_{m=1}^{\tilde{M}} \left(\sum_{\eta=0}^{N+1} \widetilde{\mathbf{L}}_{nm}^{(\tau\eta)} \mathbf{U}_{nm}^{(\eta)} + \mathbf{Q}_{snm}^{(\tau)} \right) = \mathbf{0} \tag{69}$$

Note that, if $\widetilde{N} = \widetilde{M} = +\infty$, the solution of the linear algebraic system in Eq. (69) leads to the exact analytical solution of Eq. (61). However, if $\widetilde{N}, \widetilde{M}$ assume finite values, a semi-analytical solution is obtained, which becomes of engineering interest once a certain level of convergence is reached. Using an expanded notation, Eq. (69) takes the following form:

$$\sum_{n=1}^{\tilde{N}} \sum_{m=1}^{\tilde{M}} \left(\sum_{\eta=0}^{N+1} \begin{bmatrix} \widetilde{L}_{11nm}^{(\tau\eta)\alpha_1\alpha_1} - \widetilde{L}_{fm1nm}^{(\tau\eta)\alpha_1\alpha_1} & \widetilde{L}_{12nm}^{(\tau\eta)\alpha_1\alpha_2} & \widetilde{L}_{13nm}^{(\tau\eta)\alpha_1\alpha_3} & \widetilde{L}_{14nm}^{(\tau\eta)\alpha_1\alpha_4} & \widetilde{L}_{15nm}^{(\tau\eta)\alpha_1\alpha_5} & \widetilde{L}_{16nm}^{(\tau\eta)\alpha_1\alpha_6} \\ \widetilde{L}_{21nm}^{(\tau\eta)\alpha_2\alpha_1} & \widetilde{L}_{22nm}^{(\tau\eta)\alpha_2\alpha_2} - \widetilde{L}_{fm2nm}^{(\tau\eta)\alpha_2\alpha_2} & \widetilde{L}_{23nm}^{(\tau\eta)\alpha_2\alpha_3} & \widetilde{L}_{24nm}^{(\tau\eta)\alpha_2\alpha_4} & \widetilde{L}_{25nm}^{(\tau\eta)\alpha_2\alpha_5} & \widetilde{L}_{26nm}^{(\tau\eta)\alpha_2\alpha_6} \\ \widetilde{L}_{31nm}^{(\tau\eta)\alpha_3\alpha_1} & \widetilde{L}_{32nm}^{(\tau\eta)\alpha_3\alpha_2} & \widetilde{L}_{33nm}^{(\tau\eta)\alpha_3\alpha_3} - \widetilde{L}_{fm3nm}^{(\tau\eta)\alpha_3\alpha_3} & \widetilde{L}_{34nm}^{(\tau\eta)\alpha_3\alpha_4} & \widetilde{L}_{35nm}^{(\tau\eta)\alpha_3\alpha_5} & \widetilde{L}_{36nm}^{(\tau\eta)\alpha_3\alpha_6} \\ \widetilde{L}_{41nm}^{(\tau\eta)\alpha_4\alpha_1} & \widetilde{L}_{42nm}^{(\tau\eta)\alpha_4\alpha_2} & \widetilde{L}_{43nm}^{(\tau\eta)\alpha_4\alpha_3} & \widetilde{L}_{44nm}^{(\tau\eta)\alpha_4\alpha_4} & \widetilde{L}_{45nm}^{(\tau\eta)\alpha_4\alpha_5} & \widetilde{L}_{46nm}^{(\tau\eta)\alpha_4\alpha_6} \\ \widetilde{L}_{51nm}^{(\tau\eta)\alpha_5\alpha_1} & \widetilde{L}_{52nm}^{(\tau\eta)\alpha_5\alpha_2} & \widetilde{L}_{53nm}^{(\tau\eta)\alpha_5\alpha_3} & \widetilde{L}_{54nm}^{(\tau\eta)\alpha_5\alpha_4} & \widetilde{L}_{55nm}^{(\tau\eta)\alpha_5\alpha_5} & \widetilde{L}_{56nm}^{(\tau\eta)\alpha_5\alpha_6} \\ \widetilde{L}_{61nm}^{(\tau\eta)\alpha_6\alpha_1} & \widetilde{L}_{62nm}^{(\tau\eta)\alpha_6\alpha_2} & \widetilde{L}_{63nm}^{(\tau\eta)\alpha_6\alpha_3} & \widetilde{L}_{64nm}^{(\tau\eta)\alpha_6\alpha_4} & \widetilde{L}_{65nm}^{(\tau\eta)\alpha_6\alpha_5} & \widetilde{L}_{66nm}^{(\tau\eta)\alpha_6\alpha_6} \end{bmatrix} \begin{bmatrix} \mathrm{U}_{1nm}^{(\eta)} \\ \mathrm{U}_{2nm}^{(\eta)} \\ \mathrm{U}_{3nm}^{(\eta)} \\ \Psi_{nm}^{(\tau)} \\ \Xi_{nm}^{(\eta)} \\ \mathrm{K}_{nm}^{(\eta)} \end{bmatrix} + \begin{bmatrix} Q_{1snm}^{(\tau)} \\ Q_{2snm}^{(\tau)} \\ Q_{3snm}^{(\tau)} \\ Q_{\mathrm{B}snm}^{(\tau)} \\ Q_{\mathrm{T}snm}^{(\tau)} \\ Q_{\mathrm{C}snm}^{(\tau)} \end{bmatrix} \right) = \begin{bmatrix} 0 \\ 0 \\ 0 \\ 0 \\ 0 \\ 0 \end{bmatrix} \tag{70}$$

The expression of semi-analytical coefficients $\widetilde{L}_{ijnm}^{(\tau\eta)\alpha_i\alpha_j}$ with $i,j = 1,\ldots,6$ of the matrix $\widetilde{\mathbf{L}}_{nm}^{(\tau\eta)}$ in the previous relation is reported in Ref. [25]. Finally, it should be noted that, for geometries and materials assumed in Eq. (66) and Eq. (68), the expression in Eq. (41) leads to a uniform value of the generalized constitutive coefficients along the entire parametric domain.

3. Numerical evaluation of derivatives and integrals

In this section, some details regarding the numerical evaluation of derivatives and integrals are presented. More specifically, the GDQ and the T-GIQ methods are introduced for performing numerical derivation and integration, respectively, during the post-processing step to recover the 3D solution from the higher-order 2D semi-analytical solution. To this end, non-uniform computational grid of sample points is defined within a reference interval, based on the Chebyshev-Gauss-Lobatto (CGL) distribution. The following coordinate transformation is adopted, where I_Q is the total number of sample points [67]:

$$x_i = \frac{x_{I_Q} - x_1}{\overline{x}_{I_Q} - \overline{x}_1}\left(\overline{x}_i - \overline{x}_1\right) + x_1 \tag{71}$$

In the previous relation, x_i with $i = 1,\ldots,I_Q$ represents the arbitrary element of the discrete grid associated with an arbitrary interval $[a,b]$, while $\overline{x}_i$ is the corresponding CGL element defined within a reference interval $[-1,1]$. Referring to this reference interval, the CGL grid of I_Q sample points is defined as follows:

$$\overline{x}_i = -\cos\left(\frac{i-1}{I_Q - 1}\pi\right) \tag{72}$$

where $\overline{x}_i$ with $i = 1,\ldots,I_Q$ represents the arbitrary element of the grid. In this way, the $n-$th order derivative of a one-dimensional smooth function $f = f(x)$, defined over the interval $[a,b]$, at the sample point $x_i \in [a,b]$ is computed as [67]:

$$f^{(n)}(x_i) = \left.\frac{\partial^n f(x)}{\partial x^n}\right|_{x=x_i} \cong \sum_{j=1}^{I_Q} \varsigma_{ij}^{(n)} f(x_j) \tag{73}$$

Here, $\varsigma_{ij}^{(n)}$ are the quadrature coefficients for the $n-$th order derivative. These coefficients are derived in terms of the first-order derivatives of the Lagrange polynomials $\mathscr{L}^{(1)}(x_i)$ and $\mathscr{L}^{(1)}(x_j)$ at the sample points x_i and x_j with $i,j = 1,\ldots,I_Q$, as follows [67]:

$$\begin{aligned} &\varsigma_{ij}^{(1)} = \frac{\mathscr{L}^{(1)}(x_i)}{(x_i - x_j)\mathscr{L}^{(1)}(x_j)}, \quad \varsigma_{ij}^{(n)} = n\left(\varsigma_{ij}^{(1)}\varsigma_{ii}^{(n-1)} - \frac{\varsigma_{ij}^{(n-1)}}{x_i - x_j}\right) && i \neq j \\ &\varsigma_{ii}^{(n)} = -\sum\nolimits_{j=1\ j\neq i}^{I_Q} \varsigma_{ij}^{(n)} && i = j \end{aligned} \tag{74}$$

It is very likely that Eq. (74) is adopted for simplicity over the interval $[-1,1]$, with the corresponding weighting coefficients denoted by $\widetilde{\varsigma}_{ij}^{(n)}$. When an arbitrary interval $[a,b]$ is considered, the GDQ coefficients are transformed as follows:

$$\varsigma_{ij}^{(n)} = \left(\frac{\overline{x}_{I_Q} - \overline{x}_1}{x_{I_Q} - x_1}\right)^n \widetilde{\varsigma}_{ij}^{(n)} \tag{75}$$

Similarly to the GDQ rule in Eq. (73), the integral of the function $f = f(x)$ over an interval $[x_i, x_j] \subseteq [a,b]$ is computed numerically using the T-GIQ method as follows [67]:

$$\int_{x_i}^{x_j} f(x)dx \cong \sum_{k=1}^{I_Q} w_k^{ij} f(x_k) \tag{76}$$

In this way, the integral of f is approximated as the sum of the values taken by the function at a set of $I_Q \geq m$ discrete points, denoted by x_k. On the other hand, w_k^{ij} with $k = 1,\ldots,I_Q$ are the T-GIQ weighting coefficients corresponding to the integration interval $[x_i, x_j]$. To compute these coefficients, it is useful to express the integral in Eq. (76) as the sum of two distinct integrals over the intervals $[x_i, (x_i + x_j)/2]$ and $[(x_i + x_j)/2, x_j]$. These integrals are, then, expanded through Taylor's series near the sample points x_i and x_j, respectively, as follows:

$$\int_{x_i}^{x_j} f(x)dx = \sum_{r=0}^{m-1} \frac{\left(\frac{x_j + x_i}{2} - x_i\right)^{r+1}}{(r+1)!} \left.\frac{d^r f}{dx^r}\right|_{x_i} - \sum_{r=0}^{m-1} \frac{\left(\frac{x_j + x_i}{2} - x_j\right)^{r+1}}{(r+1)!} \left.\frac{d^r f}{dx^r}\right|_{x_j} \tag{77}$$

Employing the GDQ rule from Eq. (73) to compute the derivatives in Eq. (77), one gets:

$$\begin{aligned} \int_{x_i}^{x_j} f(x)dx &= \sum_{r=0}^{m-1} \frac{(x_j - x_i)^{r+1}}{2^{r+1}(r+1)!} \sum_{k=1}^{I_Q} \varsigma_{ik}^{(r)} f(x_k) - \sum_{r=0}^{m-1} \frac{(x_i - x_j)^{r+1}}{2^{r+1}(r+1)!} \sum_{k=1}^{I_Q} \varsigma_{jk}^{(r)} f(x_k) = \\ &= \sum_{k=1}^{I_Q} \left(\sum_{r=0}^{m-1} \left(\frac{(x_j - x_i)^{r+1}}{2^{r+1}(r+1)!} \varsigma_{ik}^{(r)} - \frac{(x_i - x_j)^{r+1}}{2^{r+1}(r+1)!} \varsigma_{jk}^{(r)} \right) \right) f(x_k) = \\ &= \sum_{k=1}^{I_Q} \left(\sum_{r=0}^{m-1} \frac{(x_j - x_i)^{r+1}}{2^{r+1}(r+1)!} \left(\varsigma_{ik}^{(r)} + (-1)^{r+2} \varsigma_{jk}^{(r)} \right) \right) f(x_k) = \sum_{k=1}^{I_Q} w_k^{ij} f(x_k) \end{aligned} \tag{78}$$

When the integration interval is $[a = x_1, b = x_{I_Q}]$, the integral of $f = f(x)$ can be expressed as the sum of the integrals associated with $[x_i, x_{i+1}]$, leading to the final form of the T-GIQ rule [67]:

$$\begin{aligned} \int_a^b f(x)dx &= \sum_{i=1}^{I_Q - 1} \int_{x_i}^{x_{i+1}} f(x)dx = \sum_{i=1}^{I_Q - 1} \left(\sum_{k=1}^{I_Q} w_k^{i(i+1)} f(x_k) \right) \\ &= \sum_{k=1}^{I_Q} \left(\sum_{i=1}^{I_Q - 1} w_k^{i(i+1)} \right) f(x_k) = \sum_{k=1}^{I_Q} w_k^{1I_Q} f(x_k) \end{aligned} \tag{79}$$

4. Recovery of primary and secondary variables

When the solution of Eq. (61) is derived using Navier's method as in Eq. (71), the distribution of configuration, primary, and secondary variables within the 3D solid is recovered starting from the 2D solution. To this end, the total thickness of the shell is discretized in each $k-$th layer, with $k = 1,\ldots,l$, using the CGL distribution defined in Eq. (72). A vector of size $I_T \times 1$ is introduced within each lamina, located within the interval $[\zeta_k, \zeta_{k+1}]$, being ζ_k and ζ_{k+1} the extreme heights of each layer along the thickness direction. The arbitrary element $\zeta_{\widetilde{m}}^{(k)}$ of the discrete grid with $\widetilde{m} = 1,\ldots,I_T$ within the $k-$th layer is, then, evaluated as follows:

$$\zeta_{\widetilde{m}}^{(k)} = \frac{\zeta_{k+1} - \zeta_k}{2}\overline{x}_{\widetilde{m}} + \frac{\zeta_{k+1} + \zeta_k}{2} = \frac{h_k}{2}\overline{x}_{\widetilde{m}} + \frac{\zeta_{k+1} + \zeta_k}{2} \tag{80}$$

All the discrete points derived from Eq. (80) are conveniently arranged into the vector $\boldsymbol{\zeta}^{(k)} = \begin{bmatrix} \zeta_1^{(k)} & \cdots & \zeta_{\widetilde{m}}^{(k)} & \cdots & \zeta_{I_T}^{(k)} \end{bmatrix}^T$. Then, another vector of size $lI_Q \times 1$ is introduced, which assembles those vectors $\boldsymbol{\zeta}^{(k)}$ defined in each lamina of the shell:

$$\begin{bmatrix} \zeta_1 & \cdots & \zeta_m & \cdots & \zeta_{lI_T} \end{bmatrix}^T = \begin{bmatrix} \boldsymbol{\zeta}^{(1)T} & \cdots & \boldsymbol{\zeta}^{(k)T} & \cdots & \boldsymbol{\zeta}^{(l)T} \end{bmatrix} \tag{81}$$

Here, the arbitrary element of this vector is denoted by ζ_m, where the index $m = (k-1)I_T + \widetilde{m}$ varies between 1 and lI_Q. Note that during the assembly in Eq. (81), the relation $\zeta_{I_T}^{(k)} = \zeta_1^{(k+1)} = \zeta_{kI_T} = \zeta_{(k+1)1}$ is considered. This means that the last element of the vector $\boldsymbol{\zeta}^{(k)}$ is equal to the first element of the vector $\boldsymbol{\zeta}^{(k+1)}$, namely the last sample point in the $k-$th lamina is located at the same height as the first sample point in the

$(k+1)$-th layer. In addition, the 2D parametric domain is discretized by identifying the sample points distribution of size $I_N \times I_M$, with the arbitrary element denoted by $\left(s_{1i}, s_{2j}\right)$ with $i = 1, \ldots, I_N$ and $j = 1, \ldots, I_M$. Following the CGL distribution of Eq. (72), the quantities $s_{1i} \in [0, L_1]$ and $s_{2j} \in [0, L_2]$ are evaluated as follows:

$$s_{1i} = \frac{L_1}{2}\left(1 - \cos\left(\frac{i-1}{I_N - 1}\pi\right)\right), \quad s_{2j} = \frac{L_2}{2}\left(1 - \cos\left(\frac{j-1}{I_M - 1}\pi\right)\right) \tag{82}$$

Starting from the higher-order kinematic expansion of Eq. (5), the vector $\boldsymbol{\Delta}^{(k)}_{(ijm)}$ is evaluated, for each $\left(s_{1i}, s_{2j}\right)$ within the parametric domain, at the height ζ_m, as defined in Eq. (81), by means of the quantities $\boldsymbol{\delta}^{(\tau)}_{(ij)}$ associated with the discrete points of the physical domain and $\tau = 0, \ldots, N+1$ as follows:

$$\boldsymbol{\Delta}^{(k)}_{(ijm)} = \sum_{\tau=0}^{N+1} \mathbf{F}^{(k)}_{\tau(m)} \boldsymbol{\delta}^{(\tau)}_{(ij)} \tag{83}$$

Similarly, the elements of the vector $\boldsymbol{\pi}^{(k)}_{(ijm)}$ are evaluated from the higher-order kinematic relations of Eq. (18) in terms of the generalized primary variables vector $\boldsymbol{\pi}^{(\tau)\alpha_i}_{(ij)}$, according to the relation reported below:

$$\boldsymbol{\pi}^{(k)}_{(ijm)} = \sum_{\tau=0}^{N+1} \sum_{i=1}^{6} \mathbf{Z}^{(k\tau)\alpha_i}_{(ijm)} \boldsymbol{\pi}^{(\tau)\alpha_i}_{(ij)} \tag{84}$$

At this point, the 3D primary variables derived in Eq. (84) are used to determine the in-plane components of vector $\boldsymbol{\chi}^{(k)}$ of secondary variables through Eq. (20), while keeping in mind the material assumptions adopted for the Navier solution as outlined in Eq. (68). After performing some matrix multiplications, the following expressions are obtained:

$$\begin{aligned}
\sigma^{(k)}_{1(ijm)} &= \overline{C}^{(k)}_{11(ijm)} \varepsilon^{(k)}_{1(ijm)} + \overline{C}^{(k)}_{12(ijm)} \varepsilon^{(k)}_{2(ijm)} + \overline{C}^{(k)}_{13(ijm)} \varepsilon^{(k)}_{3(ijm)} - \overline{q}^{(k)}_{31(ijm)} \mathcal{H}^{(k)}_{3(ijm)} - \overline{\Xi}^{(k)}_{11(ijm)} \widehat{\Delta \mathrm{T}}^{(k)}_{(ijm)} - \overline{e}^{(k)}_{11(ijm)} \widehat{\Delta \mathrm{C}}^{(k)}_{(ijm)} \\
\sigma^{(k)}_{2(ijm)} &= \overline{C}^{(k)}_{12(ijm)} \varepsilon^{(k)}_{1(ijm)} + \overline{C}^{(k)}_{22(ijm)} \varepsilon^{(k)}_{2(ijm)} + \overline{C}^{(k)}_{23(ijm)} \varepsilon^{(k)}_{3(ijm)} - \overline{q}^{(k)}_{32(ijm)} \mathcal{H}^{(k)}_{3(ijm)} - \overline{\Xi}^{(k)}_{22(ijm)} \widehat{\Delta \mathrm{T}}^{(k)}_{(ijm)} - \overline{e}^{(k)}_{22(ijm)} \widehat{\Delta \mathrm{C}}^{(k)}_{(ijm)} \\
\tau^{(k)}_{12(ijm)} &= \overline{C}^{(k)}_{66(ijm)} \gamma^{(k)}_{12(ijm)} \\
\mathcal{B}^{(k)}_{1(ijm)} &= \overline{q}^{(k)}_{14(ijm)} \gamma^{(k)}_{13(ijm)} + \overline{l}^{(k)}_{11(ijm)} \mathcal{H}^{(k)}_{1(ijm)} \\
\mathcal{B}^{(k)}_{2(ijm)} &= \overline{q}^{(k)}_{25(ijm)} \gamma^{(k)}_{23(ijm)} + \overline{l}^{(k)}_{22(ijm)} \mathcal{H}^{(k)}_{2(ijm)} \\
h^{(k)}_{1(ijm)} &= \overline{k}^{(k)}_{11(ijm)} \theta^{(k)}_{1(ijm)} + \overline{y}^{(k)}_{11(ijm)} \lambda^{(k)}_{1(ijm)} \\
h^{(k)}_{2(ijm)} &= \overline{k}^{(k)}_{22(ijm)} \theta^{(k)}_{2(ijm)} + \overline{y}^{(k)}_{22(ijm)} \lambda^{(k)}_{2(ijm)} \\
c^{(k)}_{1(ijm)} &= \overline{x}^{(k)}_{11(ijm)} \theta^{(k)}_{1(ijm)} + \overline{s}^{(k)}_{11(ijm)} \lambda^{(k)}_{1(ijm)} \\
c^{(k)}_{2(ijm)} &= \overline{x}^{(k)}_{22(ijm)} \theta^{(k)}_{2(ijm)} + \overline{s}^{(k)}_{22(ijm)} \lambda^{(k)}_{2(ijm)}
\end{aligned} \tag{85}$$

The out-of-plane secondary variables are derived from the multifield balance equations along the thickness direction, expressed in curvilinear principal coordinates. More specifically, the following equations are used for the shear stresses $\tau^{(k)}_{13}$ and $\tau^{(k)}_{23}$ [25]:

$$\begin{aligned}
&\frac{\partial \tau^{(k)}_{13}}{\partial \zeta} + \tau^{(k)}_{13}\left(\frac{2}{R_1+\zeta} + \frac{1}{R_2+\zeta}\right) = -\frac{1}{A_1(1+\zeta/R_1)} \frac{\partial \sigma^{(k)}_1}{\partial \alpha_1} + \\
&+ \frac{\sigma^{(k)}_2 - \sigma^{(k)}_1}{A_1 A_2 (1+\zeta/R_2)} \frac{\partial A_2}{\partial \alpha_1} - \frac{1}{A_2(1+\zeta/R_2)} \frac{\partial \tau^{(k)}_{12}}{\partial \alpha_2} - \frac{2\tau^{(k)}_{12}}{A_1 A_2 (1+\zeta/R_1)} \frac{\partial A_1}{\partial \alpha_2} \\
&\frac{\partial \tau^{(k)}_{23}}{\partial \zeta} + \tau^{(k)}_{23}\left(\frac{1}{R_1+\zeta} + \frac{2}{R_2+\zeta}\right) = -\frac{1}{A_2(1+\zeta/R_2)} \frac{\partial \sigma^{(k)}_2}{\partial \alpha_2} + \\
&+ \frac{\sigma^{(k)}_1 - \sigma^{(k)}_2}{A_1 A_2 (1+\zeta/R_1)} \frac{\partial A_1}{\partial \alpha_2} - \frac{1}{A_1(1+\zeta/R_1)} \frac{\partial \tau^{(k)}_{12}}{\partial \alpha_1} - \frac{2\tau^{(k)}_{12}}{A_1 A_2 (1+\zeta/R_2)} \frac{\partial A_2}{\partial \alpha_1}
\end{aligned} \tag{86}$$

Note that the in-plane stress components are determined from Eq. (85) at each point of the discrete grid. Therefore, their derivatives in Eq. (86) are computed numerically using the GDQ method, as outlined in Eq. (73). These first-order differential equations are solved for each $k-$th layer. More specifically, the following boundary conditions set is considered for $k = 1$ at the first sample point, located at $\zeta = -h/2$:

$$\begin{cases} \overline{\tau}^{(1)}_{13(ij1)} = q^{(-)}_{1s(ij)} \\ \overline{\tau}^{(1)}_{23(ij1)} = q^{(-)}_{2s(ij)} \end{cases} \tag{87}$$

For the other laminae, characterized by $k \neq 1$, the boundary conditions are traced through the stress compatibility at each interface between adjacent layers:

$$\begin{cases} \overline{\tau}^{(k)}_{13\left(ij\left((k-1)I_Q+1\right)\right)} = \overline{\tau}^{(k-1)}_{13\left(ij\left((k-1)I_Q\right)\right)} \\ \overline{\tau}^{(k)}_{23\left(ij\left((k-1)I_Q+1\right)\right)} = \overline{\tau}^{(k-1)}_{23\left(ij\left((k-1)I_Q\right)\right)} \end{cases} \tag{88}$$

Finally, the loading conditions at the top surface, namely $\overline{\tau}^{(l)}_{13(ij(lI_Q))} = q^{(+)}_{1(ij)}$ and $\overline{\tau}^{(l)}_{23(ij(lI_Q))} = q^{(+)}_{2(ij)}$, are satisfied by correcting the shear stress profile along the entire thickness of the shell through the following linear transformation, where $\overline{\tau}^{(k)}_{13(ijm)}$ and $\overline{\tau}^{(k)}_{23(ijm)}$ are the shear stresses obtained from the solution of Eq. (86) [25]:

$$\begin{aligned}
\tau^{(k)}_{13(ijm)} &= \overline{\tau}^{(k)}_{13(ijm)} + \frac{q^{(+)}_{1s(ij)} - \overline{\tau}^{(l)}_{13\left(ij\left(l I_Q\right)\right)}}{h}\left(\zeta_m + \frac{h}{2}\right) \\
\tau^{(k)}_{23(ijm)} &= \overline{\tau}^{(k)}_{23(ijm)} + \frac{q^{(+)}_{2s(ij)} - \overline{\tau}^{(l)}_{23\left(ij\left(l I_Q\right)\right)}}{h}\left(\zeta_m + \frac{h}{2}\right)
\end{aligned} \tag{89}$$

In the same way, the actual profile of the $\sigma^{(k)}_3$ stress component and of the out-of-plane multifield secondary variables $\mathscr{A}^{(k)}_3 = \mathscr{B}^{(k)}_3, h^{(k)}_3, c^{(k)}_3$ are evaluated from the following differential equations, setting $\mathscr{A}_1^{(k)} = \mathscr{B}_1^{(k)}, h_1^{(k)}, c_1^{(k)}$ and $\mathscr{A}_2^{(k)} = \mathscr{B}_2^{(k)}, h_2^{(k)}, c_2^{(k)}$:

$$\begin{aligned}
&\frac{\partial \sigma_3^{(k)}}{\partial \zeta} + \sigma_3^{(k)}\left(\frac{1}{R_1+\zeta} + \frac{1}{R_2+\zeta}\right) = -\frac{1}{A_1(1+\zeta/R_1)}\frac{\partial \tau_{13}^{(k)}}{\partial \alpha_1} - \frac{\tau_{13}^{(k)}}{A_1A_2(1+\zeta/R_2)}\frac{\partial A_2}{\partial \alpha_1} + \\
&\qquad -\frac{1}{A_2(1+\zeta/R_2)}\frac{\partial \tau_{23}^{(k)}}{\partial \alpha_2} - \frac{\tau_{23}^{(k)}}{A_1A_2(1+\zeta/R_1)}\frac{\partial A_1}{\partial \alpha_2} + \frac{\sigma_1^{(k)}}{R_1+\zeta} + \frac{\sigma_2^{(k)}}{R_2+\zeta} \\
&\frac{\partial \mathscr{A}_3^{(k)}}{\partial \zeta} + \mathscr{A}_3^{(k)}\left(\frac{1}{R_1+\zeta} + \frac{1}{R_2+\zeta}\right) = -\frac{1}{A_1(1+\zeta/R_1)}\frac{\partial \mathscr{A}_1^{(k)}}{\partial \alpha_1} - \frac{\mathscr{A}_1^{(k)}}{A_1A_2(1+\zeta/R_2)}\frac{\partial A_2}{\partial \alpha_1} + \\
&\qquad -\frac{1}{A_2(1+\zeta/R_2)}\frac{\partial \mathscr{A}_2^{(k)}}{\partial \alpha_2} - \frac{\mathscr{A}_2^{(k)}}{A_1A_2(1+\zeta/R_1)}\frac{\partial A_1}{\partial \alpha_2}
\end{aligned} \tag{90}$$

The boundary conditions associated with Eq. (90) are given below:

$$\begin{aligned}
&k = 1 \;\Rightarrow\; \begin{cases} \overline{\sigma}_{3(ij1)}^{(1)} = q_{3s(ij)}^{(-)} \\ \overline{\mathscr{B}}_{3(ij1)}^{(1)} = q_{\mathrm{B}(ij)}^{(-)} \\ \overline{h}_{3(ij1)}^{(1)} = q_{\mathrm{T}(ij)}^{(-)} \\ \overline{c}_{3(ij1)}^{(1)} = q_{\mathrm{C}(ij)}^{(-)} \end{cases} \\
&k \neq 1 \;\Rightarrow\; \begin{cases} \overline{\sigma}_{3(ij((k-1)I_T+1))}^{(k)} = \overline{\sigma}_{3(ij((k-1)I_T))}^{(k-1)} \\ \overline{\mathscr{B}}_{3(ij((k-1)I_T+1))}^{(k)} = \overline{\mathscr{B}}_{3(ij((k-1)I_T))}^{(k-1)} \\ \overline{h}_{3(ij((k-1)I_T+1))}^{(k)} = \overline{h}_{3(ij((k-1)I_T))}^{(k-1)} \\ \overline{c}_{3(ij((k-1)I_T+1))}^{(k)} = \overline{c}_{3(ij((k-1)I_T))}^{(k-1)} \end{cases}
\end{aligned} \tag{91}$$

The solution of Eq. (90) through Eq. (91) is denoted by $\overline{\sigma}_{3(ijm)}^{(k)}, \overline{\mathscr{B}}_{3(ijm)}^{(k)}, \overline{h}_{3(ijm)}^{(k)}, \overline{c}_{3(ijm)}^{(k)}$. Finally, the multifield conditions at the top surface are satisfied by means of the following relations, and the secondary variables $\sigma_{3(ijm)}^{(k)}, \mathscr{B}_{3(ijm)}^{(k)}, h_{3(ijm)}^{(k)}, c_{3(ijm)}^{(k)}$ are, thus, obtained [25]:

$$\begin{aligned}
\sigma_{3(ijm)}^{(k)} &= \overline{\sigma}_{3(ijm)}^{(k)} + \frac{q_{3s(ij)}^{(+)} - \overline{\sigma}_{3(ij(lI_Q))}^{(l)}}{h}\left(\zeta_m + \frac{h}{2}\right) \\
\mathscr{B}_{3(ijm)}^{(k)} &= \overline{\mathscr{B}}_{3(ijm)}^{(k)} + \frac{q_{\mathrm{B}(ij)}^{(+)} - \overline{\mathscr{B}}_{3(ij(lI_Q))}^{(l)}}{h}\left(\zeta_m + \frac{h}{2}\right) \\
h_{3(ijm)}^{(k)} &= \overline{h}_{3(ijm)}^{(k)} + \frac{q_{\mathrm{T}(ij)}^{(+)} - \overline{h}_{3(ij(lI_Q))}^{(l)}}{h}\left(\zeta_m + \frac{h}{2}\right) \\
c_{3(ijm)}^{(k)} &= \overline{c}_{3(ijm)}^{(k)} + \frac{q_{\mathrm{C}(ij)}^{(+)} - \overline{c}_{3(ij(lI_Q))}^{(l)}}{h}\left(\zeta_m + \frac{h}{2}\right)
\end{aligned} \tag{92}$$

It should be noted that the external load considered for the mechanical case is the sum of the surface loads applied to the structure and the surface tractions from the elastic foundation. The solution of each first-order differential equations of Eqs. (86) and (90) is generally denoted by $y^{(k)} = y^{(k)}(\zeta^{(k)})$, where $\zeta^{(k)} \in [\zeta_k, \zeta_{k+1}]$ for $k = 1, \ldots, l$. These equations can be expressed in their general form as:

$$\frac{\partial y^{(k)}}{\partial \zeta^{(k)}} + a^{(k)}(\zeta^{(k)})y^{(k)}(\zeta^{(k)}) = b^{(k)}(\zeta^{(k)}) \tag{93}$$

The coefficients $a^{(k)} = a^{(k)}(\zeta^{(k)})$ and $b^{(k)} = b^{(k)}(\zeta^{(k)})$ in the differential equation can be expressed employing the following relations, setting c, $d = 1, 2$, and $B_1^{(k)}(\zeta^{(k)}), B_2^{(k)}(\zeta^{(k)})$ proper quantities:

$$\begin{aligned}
a^{(k)}(\zeta^{(k)}) &= \frac{c}{R_1 + \zeta^{(k)}} + \frac{d}{R_2 + \zeta^{(k)}} \\
b^{(k)}(\zeta^{(k)}) &= \frac{B_1^{(k)}(\zeta^{(k)})}{R_1 + \zeta^{(k)}} + \frac{B_2^{(k)}(\zeta^{(k)})}{R_2 + \zeta^{(k)}}
\end{aligned} \tag{94}$$

The solution of Eq. (93) is, thus, provided in closed-form within each $k-$th layer of the structure, for $k = 1, \ldots, l$, by means of the thickness coordinate $\zeta^{(k)} \in [\zeta_k, \zeta_{k+1}]$ as follows:

$$\begin{aligned}
y^{(k)}(\zeta^{(k)}) &= e^{-A^{(k)}(\zeta^{(k)})}\int_{\zeta_1^{(k)}}^{\zeta^{(k)}} e^{A^{(k)}(\zeta^{(k)})}b^{(k)}(\zeta^{(k)})d\zeta^{(k)} + y_1^{(k)} \\
&= e^{-A^{(k)}(\zeta^{(k)})}\int_{\zeta_1^{(k)}}^{\zeta^{(k)}} f(\zeta^{(k)})d\zeta^{(k)} + y_1^{(k)}
\end{aligned} \tag{95}$$

The term $A^{(k)} = A^{(k)}(\zeta^{(k)})$ represents the integral of the coefficient $a^{(k)} = a^{(k)}(\zeta^{(k)})$ from Eq. (94). The closed-form expression of this integral is evaluated as follows:

$$\begin{aligned}
A^{(k)}(\zeta^{(k)}) &= \int a^{(k)}(\zeta^{(k)})d\zeta^{(k)} \\
&= \begin{cases} \log\left((R_1 + \zeta^{(k)})^c (R_2 + \zeta^{(k)})^d\right) & R_1 \neq \infty, R_2 \neq \infty \\ \log\left((R_2 + \zeta^{(k)})^d\right) & R_1 = \infty, R_2 \neq \infty \\ \log\left((R_1 + \zeta^{(k)})^c\right) & R_1 \neq \infty, R_2 = \infty \\ 0 & R_1 = R_2 = \infty \end{cases}
\end{aligned} \tag{96}$$

The quantity $f^{(k)} = f^{(k)}(\zeta^{(k)})$ in Eq. (95) takes the following expression:

$$f^{(k)}(\zeta^{(k)}) = \begin{cases} (R_1 + \zeta^{(k)})^c (R_2 + \zeta^{(k)})^d b^{(k)}(\zeta^{(k)}) & R_1 \neq \infty, R_2 \neq \infty \\ (R_2 + \zeta^{(k)})^d b^{(k)}(\zeta^{(k)}) & R_1 = \infty, R_2 \neq \infty \\ (R_1 + \zeta^{(k)})^c b^{(k)}(\zeta^{(k)}) & R_1 \neq \infty, R_2 = \infty \\ b^{(k)}(\zeta^{(k)}) & R_1 = R_2 = \infty \end{cases} \tag{97}$$

Since Eq. (97) is evaluated at each discrete point $\zeta_{\tilde{m}}^{(k)} \in [\zeta_k, \zeta_{k+1}]$ along the thickness direction, a vector $\mathbf{f}^{(k)}$ of size $I_T \times 1$ is introduced to contain the discrete values of $f^{(k)}$. This vector is expressed as follows:

$$\mathbf{f}^{(k)} = \mathbf{g}^{(k)} \odot \mathbf{b}^{(k)} = \mathrm{diag}(\mathbf{g}^{(k)})\mathbf{b}^{(k)} = \mathbf{G}^{(k)}\mathbf{b}^{(k)} \tag{98}$$

In the previous equation, $\mathbf{b}^{(k)}$ is a vector of size $I_T \times 1$ containing the discrete values of the quantity b at each height $\zeta_m^{(k)}$ with $m = 1, \ldots, I_T$, while $\odot$ denotes the Hadamard product. The arbitrary element of $\mathbf{g}^{(k)}$, denoted by $g_m^{(k)}$, takes the following expression:

$$g_m^{(k)} = \begin{cases} \left(R_1 + \zeta_m^{(k)}\right)^c \left(R_2 + \zeta_m^{(k)}\right)^d & R_1 \neq \infty, R_2 \neq \infty \\ \left(R_2 + \zeta_m^{(k)}\right)^d & R_1 = \infty, R_2 \neq \infty \\ \left(R_1 + \zeta_m^{(k)}\right)^c & R_1 \neq \infty, R_2 = \infty \\ 1 & R_1 = R_2 = \infty \end{cases} \tag{99}$$

Finally, the integral of $f^{(k)}$ occurring in Eq. (95) is evaluated along the entire thickness of the laminate by considering the interval $[\zeta_k, \zeta_{k+1}]$, with $k = 1, \ldots, l$, and employing the T-GIQ rule as shown in Eq. (79), resulting in the following expression:

$$\begin{aligned} \int_{\zeta_1^{(k)}}^{\zeta_i^{(k)}} e^{-A^{(k)}\left(\zeta^{(k)}\right)} b^{(k)}\left(\zeta^{(k)}\right) d\zeta^{(k)} &= \int_{\zeta_1^{(k)}}^{\zeta_i^{(k)}} f^{(k)}\left(\zeta^{(k)}\right) d\zeta^{(k)} \\ &= \sum_{\tilde{m}=1}^{I_T} \left(w_{i\tilde{m}} - w_{1\tilde{m}}\right) f^{(k)}\left(\zeta_{\tilde{m}}^{(k)}\right) \\ &= \sum_{\tilde{m}=1}^{I_T} w_k^{1i} f^{(k)}\left(\zeta_{\tilde{m}}^{(k)}\right) \end{aligned} \tag{100}$$

where a local thickness coordinate $\zeta_{\tilde{m}}^{(k)}$ has been conveniently adopted. In this way, the solution of Eq. (95), consisting of the values $y^{(k)}\left(\zeta_{\tilde{m}}^{(k)}\right)$ collected within the vector $\mathbf{y}^{(k)}$, can be computed numerically as follows:

$$\begin{aligned} y^{(k)}\left(\zeta_{\tilde{m}}^{(k)}\right) &= \frac{1}{g_{\tilde{m}}^{(k)}} \sum_{i=1}^{I_T} w_i^{1\tilde{m}} g_i^{(k)} b^{(k)}\left(\zeta_i^{(k)}\right) + y_1^{(k)} \Rightarrow \mathbf{y}^{(k)} \\ &= \left(\mathbf{G}^{(k)}\right)^{-1} \mathbf{W}^{(k)} \mathbf{G}^{(k)} \mathbf{b}^{(k)} + y_1^{(k)} \end{aligned} \tag{101}$$

The previous expression can be simplified by assuming $\mathbf{G}^{(k)} \cong \mathbf{I}$, since for a doubly-curved panel, the geometric relation $\zeta_i^{(k)}, \zeta_l^{(k)} \ll R_1, R_2$ can be assumed. In this way, Eq. (101) becomes:

$$y^{(k)}\left(\zeta_{\tilde{m}}^{(k)}\right) = \sum_{i=1}^{I_T} w_i^{1\tilde{m}} b\left(\zeta_i^{(k)}\right) + y_1^{(k)} \Rightarrow \mathbf{y}^{(k)} = \mathbf{W}^{(k)} \mathbf{b}^{(k)} + y_1^{(k)} \tag{102}$$

Once the secondary variables are recovered using the balance-equation-based recovery procedure, the out-of-plane primary variables of the model are determined from the inverse form of the constitutive relationship in Eq. (20), resulting in the following linear system at each discrete point of the solid [25]:

$$\mathbf{A}_{(ijm)}^{(k)} \mathbf{x}_{(ijm)}^{(k)} = \mathbf{B}_{(ijm)}^{(k)} \quad \Leftrightarrow \quad \begin{bmatrix} \mathbf{A}_{11(ijm)}^{(k)} & \mathbf{0} \\ \mathbf{0} & \mathbf{A}_{22(ijm)}^{(k)} \end{bmatrix} \begin{bmatrix} \mathbf{x}_{1(ijm)}^{(k)} \\ \mathbf{x}_{2(ijm)}^{(k)} \end{bmatrix} = \begin{bmatrix} \mathbf{B}_{1(ijm)}^{(k)} \\ \mathbf{B}_{2(ijm)}^{(k)} \end{bmatrix} \tag{103}$$

where

$$\mathbf{A}_{11(ijm)}^{(k)} = \begin{bmatrix} \overline{C}_{44(ijm)}^{(k)} & \overline{C}_{45(ijm)}^{(k)} & \overline{C}_{34(ijm)}^{(k)} & -\overline{q}_{34(ijm)}^{(k)} \\ \overline{C}_{45(ijm)}^{(k)} & \overline{C}_{55(ijm)}^{(k)} & \overline{C}_{35(ijm)}^{(k)} & -\overline{q}_{35(ijm)}^{(k)} \\ \overline{C}_{34(ijm)}^{(k)} & \overline{C}_{35(ijm)}^{(k)} & \overline{C}_{33(ijm)}^{(k)} & -\overline{q}_{33(ijm)}^{(k)} \\ \overline{q}_{34(ijm)}^{(k)} & \overline{q}_{35(ijm)}^{(k)} & \overline{q}_{33(ijm)}^{(k)} & \overline{m}_{33(ijm)}^{(k)} \end{bmatrix} \tag{104}$$

$$\mathbf{A}_{22(ijm)}^{(k)} = \begin{bmatrix} \overline{k}_{33(ijm)}^{(k)} & \overline{y}_{33(ijm)}^{(k)} \\ \overline{x}_{33(ijm)}^{(k)} & \overline{s}_{33(ijm)}^{(k)} \end{bmatrix}$$

The unknown vector in Eq. (103), denoted by $\mathbf{x}_{(ijm)}^{(k)}$, is conveniently split into the sub-vectors $\mathbf{x}_{1(ijm)}^{(k)} = \begin{bmatrix} \gamma_{13(ijm)}^{(k)} & \gamma_{23(ijm)}^{(k)} & \varepsilon_{3(ijm)}^{(k)} & \mathscr{H}_{3(ijm)}^{(k)} \end{bmatrix}^T$ and $\mathbf{x}_{2(ijm)}^{(k)} = \begin{bmatrix} \theta_{3(ijm)}^{(k)} & \lambda_{3(ijm)}^{(k)} \end{bmatrix}^T$. Similarly, the vector $\mathbf{B}_{(ijm)}^{(k)}$ is divided into the vectors $\mathbf{B}_{1(ijm)}^{(k)} = \begin{bmatrix} b_{1(ijm)}^{(k)} & b_{2(ijm)}^{(k)} & b_{3(ijm)}^{(k)} & b_{4(ijm)}^{(k)} \end{bmatrix}^T$ and $\mathbf{B}_{2(ijm)}^{(k)} = \begin{bmatrix} b_{5(ijm)}^{(k)} & b_{6(ijm)}^{(k)} \end{bmatrix}^T$, whose elements are expressed as follows:

$$\begin{aligned} b_{1(ijm)}^{(k)} &= \tau_{13(ijm)}^{(k)} - \overline{C}_{14(ijm)}^{(k)} \varepsilon_{1(ijm)}^{(k)} - \overline{C}_{24(ijm)}^{(k)} \varepsilon_{2(ijm)}^{(k)} - \overline{C}_{46(ijm)}^{(k)} \gamma_{12(ijm)}^{(k)} + \overline{q}_{14(ijm)}^{(k)} \mathcal{H}_{1(ijm)}^{(k)} + \overline{q}_{24(ijm)}^{(k)} \mathcal{H}_{2(ijm)}^{(k)} + \\ &\quad + \overline{\Xi}_{13(ijm)}^{(k)} \widehat{\Delta\mathrm{T}}_{(ijm)}^{(k)} + \overline{e}_{13(ijm)}^{(k)} \widehat{\Delta\mathrm{C}}_{(ijm)}^{(k)} \\ b_{2(ijm)}^{(k)} &= \tau_{23(ijm)}^{(k)} - \overline{C}_{15(ijm)}^{(k)} \varepsilon_{1(ijm)}^{(k)} - \overline{C}_{25(ijm)}^{(k)} \varepsilon_{2(ijm)}^{(k)} - \overline{C}_{56(ijm)}^{(k)} \gamma_{12(ijm)}^{(k)} + \overline{q}_{15(ijm)}^{(k)} \mathcal{H}_{1(ijm)}^{(k)} + \overline{q}_{25(ijm)}^{(k)} \mathcal{H}_{2(ijm)}^{(k)} + \\ &\quad + \overline{\Xi}_{23(ijm)}^{(k)} \widehat{\Delta\mathrm{T}}_{(ijm)}^{(k)} + \overline{e}_{23(ijm)}^{(k)} \widehat{\Delta\mathrm{C}}_{(ijm)}^{(k)} \\ b_{3(ijm)}^{(k)} &= \sigma_{3(ijm)}^{(k)} - \overline{C}_{13(ijm)}^{(k)} \varepsilon_{1(ijm)}^{(k)} - \overline{C}_{23(ijm)}^{(k)} \varepsilon_{2(ijm)}^{(k)} - \overline{C}_{36(ijm)}^{(k)} \gamma_{12(ijm)}^{(k)} + \overline{q}_{13(ijm)}^{(k)} \mathcal{H}_{1(ijm)}^{(k)} + \overline{q}_{23(ijm)}^{(k)} \mathcal{H}_{2(ijm)}^{(k)} + \\ &\quad + \overline{\Xi}_{33(ijm)}^{(k)} \widehat{\Delta\mathrm{T}}_{(ijm)}^{(k)} + \overline{e}_{33(ijm)}^{(k)} \widehat{\Delta\mathrm{C}}_{(ijm)}^{(k)} \\ b_{4(ijm)}^{(k)} &= \mathcal{B}_{3(ijm)}^{(k)} - \overline{p}_{31(ijm)}^{(k)} \varepsilon_{1(ijm)}^{(k)} - \overline{q}_{32(ijm)}^{(k)} \varepsilon_{2(ijm)}^{(k)} - \overline{q}_{36(ijm)}^{(k)} \gamma_{12(ijm)}^{(k)} - \overline{m}_{13(ijm)}^{(k)} \mathcal{H}_{1(ijm)}^{(k)} - \overline{m}_{23(ijm)}^{(k)} \mathcal{H}_{2(ijm)}^{(k)} + \\ &\quad - \overline{w}_{33(ijm)}^{(k)} \widehat{\Delta\mathrm{T}}_{(ijm)}^{(k)} - \overline{f}_{33(ijm)}^{(k)} \widehat{\Delta\mathrm{C}}_{(ijm)}^{(k)} \\ b_{5(ijm)}^{(k)} &= h_{3(ijm)}^{(k)} - \overline{k}_{13(ijm)}^{(k)} \theta_{1(ijm)}^{(k)} - \overline{k}_{23(ijm)}^{(k)} \theta_{2(ijm)}^{(k)} - \overline{y}_{13(ijm)}^{(k)} \lambda_{1(ijm)}^{(k)} - \overline{y}_{23(ijm)}^{(k)} \lambda_{2(ijm)}^{(k)} \\ b_{6(ijm)}^{(k)} &= c_{3(ijm)}^{(k)} - \overline{x}_{13(ijm)}^{(k)} \theta_{1(ijm)}^{(k)} - \overline{x}_{23(ijm)}^{(k)} \theta_{2(ijm)}^{(k)} - \overline{s}_{13(ijm)}^{(k)} \lambda_{1(ijm)}^{(k)} - \overline{s}_{23(ijm)}^{(k)} \lambda_{2(ijm)}^{(k)} \end{aligned} \tag{105}$$

This procedure for reconstructing the primary and secondary variables is iterated until convergence is achieved between two successive iterations. The recovery procedure is essential for an accurate reconstruction of the profiles for the various quantities, as higher-order theories alone do not inherently ensure equilibrium along the thickness direction.

5. Applications and results

In this section, the higher-order 2D formulation is applied to some numerical examples to investigate the multifield response of panels of various sizes and curvatures under mechanical, hygro-thermal, and magnetic external fields. These investigations aim to evaluate the coupled multifield behavior of these structures, accounting for various coupling effects that are not contemplated in commercial software, while maintaining a reduced computational effort. In addition, it is demonstrated that the results align well with those obtained from 3D finite element simulations. A preliminary example is provided to validate the formulation. A simply-supported rectangular plate is considered, consisting of four layers with thicknesses $h_1 = 4 \times 10^{-3}$ m, $h_2 = h_4 = 3 \times 10^{-3}$ m and $h_3 = 5 \times 10^{-3}$ m. The equation for the reference surface is given below, where $(x, y) \in [0, L_1] \times [0, L_2]$ represents the rectangular parametric domain:

$$\mathbf{r}(s_1, s_2) = \mathbf{r}(x, y) = -x\,\mathbf{e}_2 + y\,\mathbf{e}_3 \tag{106}$$

According to Eq. (3), the relations $A_1 = A_2 = 1$ and $1/R_1 = 1/R_2 = 0$ can be assumed for the rectangular plate. The geometric dimensions of the physical domain are $L_1 = 1.2 \times 10^{-1}$ m and $L_2 = 2.2 \times 10^{-1}$ m, while the lamination scheme is $(\text{MAT - I}\backslash \text{CoFe}_2\text{O}_4\backslash \text{MAT - III}\backslash \text{CoFe}_2\text{O}_4)$, and the material orientation is $(0\backslash 0\backslash 0\backslash 0)$, following a cross-ply arrangement. The materials MAT-I, MAT-II, and MAT-III are characterized by fiber volume fractions of $V_f = 0.2$, $V_f = 0.4$ and $V_f = 0.6$, respectively. The homogenized properties of these materials are derived using the analytical expressions provided in Appendix 1, considering barium titanate ($BaTiO_3$) and cobalt ferrite ($CoFe_2O_4$) as raw materials. For simplicity, these properties are summarized in Table 1. A sinusoidally-distributed mechanical surface traction is applied at the top surface ($\zeta = h/2$). The mechanical response of the panel is evaluated at $(0.25L_1, 0.75L_2)$ within the physical domain. Three simulations are conducted: magneto-mechanical (M–D), thermo-mechanical (T-D), and hygro-mechanical (H-D) analysis. The loading conditions for each case are illustrated in Fig. 1, and the results are presented in Tables 2-5, Tables 6-9, and Tables 10-13, which include the distributions along the thickness direction of unknown variables, primary variables, and secondary variables. The simulations are performed using the ELDZL7

Table 1

Homogenized properties of smart materials with hygro-thermo-magneto-mechanical properties employed in the simulations. These materials are obtained from the combination with proper volume fraction of barium titanate and cobalt ferrite, according to the procedure detailed in Appendix 1.

Material	$CoFe_2O_4$	MAT - I	MAT - II	MAT - III	$BaTiO_3$
V_f	0	0.2	0.4	0.6	1
T_0[K]	297	297	297	297	297
$\rho\,[\text{kg/m}^3]$	5300	5400	5500	5600	5800
$M_\infty\,[\%]$	0.01	0.01	0.02	0.01	0.03
$c\ [\text{J/kgK}]$	377.36	414.58	450.45	357.14	550.62
$C_{11} = C_{22}\,[\times 10^9\ \text{N/m}^2]$	286	252.38	224.95	202.08	166
$C_{12}\,[\times 10^9\ \text{N/m}^2]$	173	144.72	122.34	104.26	77
$C_{13} = C_{23}\,[\times 10^9\ \text{N/m}^2]$	170.5	143.99	122.66	105.13	78
$C_{66} = (C_{11} - C_{12})/2\,[\times 10^9\ \text{N/m}^2]$	56.5	53.83	51.30	48.91	44.5
$C_{44} = C_{55}\,[\times 10^9\ \text{N/m}^2]$	45.3	47.15	48.99	50.81	43
$C_{33}\,[\times 10^9\ \text{N/m}^2]$	269.5	24.11	217.22	196.54	162
$p_{14} = p_{25}\,[\text{C/m}^2]$	0	0.04	0.10	0.23	11.6
$p_{31} = p_{32}\,[\text{C/m}^2]$	0	−1.26	−2.28	−3.11	−4.4
$p_{33}\,[\text{C/m}^2]$	0	3.39	6.99	10.76	18.6
$q_{14} = q_{25}\,[\text{Wb/m}^2]$	550	367.81	237.00	138.50	0
$q_{31} = q_{32}\,[\text{Wb/m}^2]$	580.3	414.00	280.18	170.17	0
$q_{33}\,[\text{Wb/m}^2]$	−699.7	−602.79	−478.06	–332.94	0
$a_{11} = a_{22}\,[\times 10^{-6}\ 1/\text{K}]$	10	11.02	12.09	13.22	15.7
$a_{33}\,[\times 10^{-6}\ 1/\text{K}]$	5	5.17	5.39	5.65	6.4
$b_{11} = b_{22}\,[\times 10^{-4}\ \text{m}^3/\text{kg}]$	1.1	0.90	0.70	0.48	0
$b_{33}\,[\times 10^{-4}\ \text{m}^3/\text{kg}]$	0	0.01	0.02	0.02	0
$l_{11} = l_{22}\,[\times 10^{-9}\ \text{F/m}]$	0.08	11.94	18.44	0.31	11.2
$l_{33}\,[\times 10^{-9}\ \text{F/m}]$	0.093	26.10	5.11	7.62	12.6
$d_{11} = d_{22}\,[\times 10^{-12}\ \text{s/m}]$	0	−2.56	−4.46	−5.91	0
$d_{33}\,[\times 10^{-9}\ \text{s/m}]$	0	2.05	2.77	2.52	0
$m_{11} = m_{22}\,[\times 10^{-6}\ \text{H/m}]$	590	396.10	0.06	152.2	5
$m_{33}\,[\times 10^{-6}\ \text{H/m}]$	157	127.87	1.71	69.1	10
$o_{33}\,[\times 10^{-5}\ \text{C/m}^2\text{K}]$	0	3.60	7.46	11.51	20
$g_{33}\,[\times 10^{-4}\ \text{Cm/kg}]$	0	−1.78	−2.41	−2.20	0
$w_{33}\,[\times 10^{-4}\ \text{T/K}]$	3.2	−2.69	−5.18	−5.19	0
$f_{33}\,[\text{Tm}^3/\text{kg}]$	0	−0.02	−0.03	−0.03	0
$k_{11} = k_{22}[\text{J/mK}]$	3.2	3.03	2.88	2.74	2.5
$k_{33}[\text{J/mK}]$	3.2	3.06	2.92	2.78	2.5
$s_{11} = s_{22}\,[\times 10^{-8}\ \text{m}^2](u_d = 0.1,\ \lambda\nu = 0.25)$	16	13.24	11.29	9.84	7.83
$s_{33}\,[\times 10^{-8}\ \text{m}^2](u_d = 0.1,\ \lambda\nu = 0.25)$	16	14.37	12.73	11.1	7.83
$x_{11} = x_{22}\,[\times 10^{-8}\ \text{kg/mK}](u_d = 0.1,\ \lambda\nu = 0.25)$	4.08	4.46	4.61	4.66	4.57
$x_{33}\,[\times 10^{-8}\ \text{kg/mK}](u_d = 0.1,\ \lambda\nu = 0.25)$	4.08	4.50	4.68	4.73	4.57
$y_{11} = y_{22}\,[\text{J/m}^2\text{K}](u_d = 0.1,\ \lambda\nu = 0.25)$	3.14	2.25	1.76	1.45	1.07
$y_{33}\,[\text{J/m}^2\text{K}](u_d = 0.1,\ \lambda\nu = 0.25)$	3.14	2.44	1.99	1.63	1.07

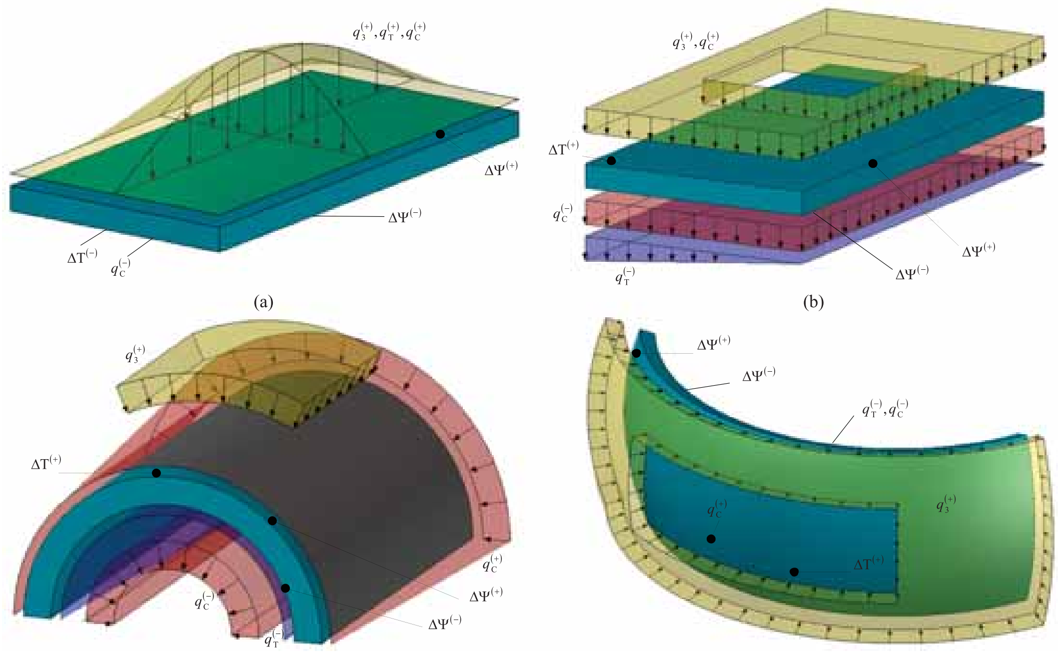

(a) (b)

(c) (d)

Fig. 1. Load shapes and combinations for multifield analysis in examples of investigation. Rectangular plate with sinusoidally-distributed mechanical loads and prescribed configuration variables (a), rectangular plate under multifield uniform and hydrostatic surface loads and mechanical ring pressure (b), cylindrical panel with hydrostatic and patch loads (c), spherical shell with mechanical ring load (d).

Table 2
Numerical prediction of the distribution along the thickness direction of the 3D displacement field components and magnetic potential variation of a simply-supported rectangular plate employing higher-order ELW theories for M−D analysis. The results are provided at $(0.25L_1, 0.75L_2)$ within the 2D physical domain. The reference solution is derived by using 3D FEM commercial software.

	$U_1\ [\times 10^{-7}\text{m}]$		$U_2\ [\times 10^{-7}\text{m}]$		$U_3\ [\times 10^{-6}\text{m}]$		$\Delta\psi\ [\times 10^{1}\text{A}]$	
$\zeta\ [10^{-3}\text{m}]$	3D FEM	ELDZL7	3D FEM	ELDZL7	3D FEM	ELDZL7	3D FEM	ELDZL7
−7.5	−2.51	−2.51	1.37	1.37	−1.36	−1.36	0.00	0.00
−6.3	−2.09	−2.30	1.14	1.26	−1.36	−1.36	1.00	0.81
−5.5	−1.82	−2.16	0.99	1.18	−1.37	−1.36	1.59	1.29
−4.3	−1.41	−1.95	0.77	1.07	−1.37	−1.37	2.36	1.96
−3.5	−1.14	−1.82	0.62	0.99	−1.37	−1.37	2.81	2.40
−3.5	−1.14	−1.82	0.62	0.99	−1.37	−1.37	2.81	2.40
−2.0	−0.64	−0.64	0.35	0.35	−1.38	−1.38	3.49	2.91
−0.5	−0.15	−0.15	0.08	0.08	−1.38	−1.38	4.00	3.40
−0.5	−0.15	−0.15	0.08	0.08	−1.38	−1.38	4.00	3.40
0.7	0.27	0.27	−0.14	−0.14	−1.38	−1.38	4.64	4.03
2.0	0.68	0.68	−0.37	−0.37	−1.38	−1.38	5.18	4.62
3.2	1.10	1.10	−0.60	−0.60	−1.37	−1.37	5.63	5.11
4.5	1.52	1.52	−0.83	−0.83	−1.37	−1.37	5.97	5.43
4.5	1.52	1.52	−0.83	−0.83	−1.37	−1.37	5.97	5.43
6.0	2.03	2.03	−1.11	−1.11	−1.37	−1.37	5.58	5.32
7.5	2.55	2.55	−1.39	−1.39	−1.36	−1.36	5.00	5.00

kinematic model. In other words, higher-order polynomials with $\gamma = \delta = 0$ and $N = 7$ are employed in Eq. (6), while the ELW zigzag function from Eq. (8) is used for $\tau = N + 1$. In addition, a 3D FEM solution is obtained using a commercial software. The 3D mesh consists of 536268 nodes with parabolic brick elements. For the M−D case, a sinusoidal distribution of magnetic potential with $n = m = 1$ and magnitude $\Delta\overline{\Psi}_s^{(+)} = 1\,\text{A}$ is applied at the top surface, while a null value ($\Delta\overline{\Psi}_s^{(-)} = 0\,\text{A}$) is maintained at the bottom surface ($\zeta = -h/2$). Furthermore, a sinusoidal distribution ($\widetilde{N} = \widetilde{M} = 1$) of mechanical pressure is applied at the top surface with a magnitude of $\overline{q}_3^{(+)} = 1 \times 10^5\ \text{N/m}^2$. The same mechanical load is applied in the H-D simulation, where sinusoidal mass fluxes are enforced at the top and bottom surfaces, with magnitudes $\overline{q}_C^{(+)} = 2.8 \times 10^{-7}\ \text{kg/m}^2$ and $\overline{q}_C^{(-)} = 1.6 \times 10^{-7}\ \text{kg/m}^2$, respectively. Finally, in the T-D simulation, a temperature variation with $\Delta\overline{T}_s^{(-)} = -1\,\text{K}$ is applied at $\zeta = -h/2$, while a sinusoidal thermal flux with magnitude $\overline{q}_T^{(+)} = 1\ \text{J/m}^2$ and $\widetilde{N} = \widetilde{M} = 1$ is enforced at the top surface. In addition, a sinusoidal mechanical pressure with $\overline{q}_3^{(+)} = 1 \times 10^5\ \text{N/m}^2$ is considered at the top surface. As shown in Table 2, the in-plane displacement field components exhibit typical linear profiles, while U_3 shows a parabolic distribution. The ELW predictions are perfectly aligned with the results from 3D finite elements. In addition, the through-the-thickness distribution of magnetic potential displays a slope change at each interface of the panel, highlighting the importance of the zigzag function in the multifield kinematic model. The in-plane strain components in Table 3 follow linear distributions, while the out-of-plane components exhibit more complex profiles, particularly when the stiffness of adjacent laminae varies significantly. However, the recovery procedure ensures

Table 3
Numerical prediction of the distribution along the thickness direction of the 3D strain components of a simply-supported rectangular plate employing higher-order ELW theories for M−D analysis. The results are provided at $(0.25L_1, 0.75L_2)$ within the 2D physical domain. The reference solution is derived by using 3D FEM commercial software.

	$\varepsilon_1\ [\times 10^{-6}\mathrm{m/m}]$		$\varepsilon_2\ [\times 10^{-6}\mathrm{m/m}]$		$\gamma_{12}\ [\times 10^{-5}\mathrm{m/m}]$		$\gamma_{13}\ [\times 10^{-6}\mathrm{m/m}]$		$\gamma_{23}\ [\times 10^{-6}\mathrm{m/m}]$		$\varepsilon_3\ [\times 10^{-6}\mathrm{m/m}]$	
$\zeta\ [10^{-3}\mathrm{m}]$	3D FEM	ELDZL7	3D FEM	ELDZL7	3D FEM	ELDZL7	3D FEM	ELDZL7	3D FEM	ELDZL7	3D FEM	ELDZL7
−7.5	6.58	6.58	1.96	1.96	7.18	7.18	−0.01	0.00	0.00	0.00	−4.92	−4.91
−6.3	5.48	5.48	1.63	1.63	5.98	5.98	−0.92	−0.92	0.50	0.50	−4.09	−4.08
−5.5	4.76	4.75	1.41	1.41	5.19	5.19	−1.45	−1.44	0.79	0.79	−3.55	−3.54
−4.3	3.69	3.68	1.10	1.10	4.02	4.02	−2.10	−2.09	1.14	1.14	−2.75	−2.74
−3.5	2.98	2.98	0.89	0.89	3.25	3.25	−2.44	−2.43	1.33	1.32	−2.23	−2.22
−3.5	2.98	2.98	0.89	0.89	3.25	3.25	−2.57	−2.57	−0.22	1.40	−2.37	−2.37
−2.0	1.68	1.68	0.50	0.50	1.83	1.83	−3.08	−3.07	1.68	1.67	−1.34	−1.34
−0.5	0.39	0.39	0.12	0.12	0.43	0.43	−3.32	−3.31	1.81	1.80	−0.34	−0.32
−0.5	0.39	0.39	0.12	0.12	0.43	0.43	−3.32	−2.89	−0.12	1.57	−0.29	−0.29
0.7	−0.69	−0.69	−0.21	−0.21	−0.76	−0.76	−2.87	−2.86	1.56	1.56	0.42	0.44
2.0	−1.78	−1.78	−0.53	−0.53	−1.94	−1.94	−2.73	−2.71	1.48	1.48	1.13	1.15
3.2	−2.87	−2.87	−0.86	−0.86	−3.14	−3.14	−2.44	−2.43	1.33	1.33	1.85	1.87
4.5	−3.98	−3.98	−1.18	−1.18	−4.34	−4.34	−2.02	−2.02	1.10	1.10	2.59	2.60
4.5	−3.98	−3.98	−1.18	−1.18	−4.34	−4.34	−2.40	−2.39	−0.39	1.31	3.08	3.09
6.0	−5.31	−5.31	−1.58	−1.58	−5.79	−5.79	−1.43	−1.41	0.78	0.77	4.13	4.15
7.5	−6.68	−6.68	−1.99	−1.99	−7.28	−7.28	−0.17	−0.16	0.09	0.09	5.23	5.24

Table 4
Numerical prediction of the distribution along the thickness direction of the 3D stress components of a simply-supported rectangular plate employing higher-order ELW theories for M−D analysis. The results are provided at $(0.25L_1, 0.75L_2)$ within the 2D physical domain. The reference solution is derived by using 3D FEM commercial software.

	$\sigma_1\ [\times 10^{6}\,\mathrm{N/m^2}]$		$\sigma_2\ [\times 10^{6}\,\mathrm{N/m^2}]$		$\tau_{12}\ [\times 10^{5}\,\mathrm{N/m^2}]$		$\tau_{13}\ [\times 10^{5}\,\mathrm{N/m^2}]$		$\tau_{23}\ [\times 10^{4}\,\mathrm{N/m^2}]$		$\sigma_3\ [\times 10^{4}\,\mathrm{N/m^2}]$	
$\zeta\ [10^{-3}\mathrm{m}]$	3D FEM	ELDZL7	3D FEM	ELDZL7	3D FEM	ELDZL7	3D FEM	ELDZL7	3D FEM	ELDZL7	3D FEM	ELDZL7
−7.5	1.27	1.25	7.68	7.57	3.87	3.87	−0.01	0.00	0.02	0.00	0.03	0.00
−6.3	1.06	1.06	6.42	6.47	3.22	3.22	−0.43	−0.43	2.32	2.32	−0.08	−0.09
−5.5	0.92	0.92	5.58	5.58	2.79	2.79	−0.67	−0.67	3.63	3.64	−0.23	−0.24
−4.3	0.71	0.71	4.35	4.28	2.16	2.16	−0.97	−0.96	5.28	5.26	−0.55	−0.57
−3.5	0.58	0.57	3.53	3.47	1.75	1.75	−1.13	−1.12	6.14	6.11	−0.83	−0.86
−3.5	0.63	0.63	3.91	3.96	1.84	1.84	−1.13	−1.12	6.14	6.11	−0.84	−0.86
−2.0	0.36	0.36	2.24	2.30	1.04	1.04	−1.35	−1.35	7.36	7.35	−1.48	−1.49
−0.5	0.09	0.09	0.59	0.58	0.24	0.24	−1.45	−1.45	7.92	7.91	−2.20	−2.21
−0.5	0.07	0.06	0.43	0.37	0.21	0.21	−1.45	−1.45	7.92	7.91	−2.21	−2.21
0.7	−0.11	−0.11	−0.62	−0.65	−0.37	−0.37	−1.44	−1.44	7.86	7.86	−2.83	−2.83
2.0	−0.29	−0.29	−1.66	−1.69	−0.95	−0.95	−1.37	−1.36	7.45	7.43	−3.43	−3.42
3.2	−0.47	−0.46	−2.71	−2.66	−1.53	−1.53	−1.22	−1.22	6.64	6.64	−3.98	−3.97
4.5	−0.65	−0.62	−3.77	−3.49	−2.12	−2.12	−1.01	−1.01	5.48	5.49	−4.47	−4.45
4.5	−0.82	−0.85	−5.06	−5.38	−2.45	−2.45	−1.01	−1.01	5.48	5.49	−4.48	−4.45
6.0	−1.10	−1.09	−6.74	−6.71	−3.27	−3.27	−0.57	−0.56	3.09	3.07	−4.89	−4.85
7.5	−1.38	−1.39	−8.46	−8.63	−4.12	−4.12	−0.01	0.00	0.02	0.00	−5.03	−5.00

Table 5
Numerical prediction of the distribution along the thickness direction of the 3D magnetic primary and secondary variables of a simply-supported rectangular plate employing higher-order ELW theories for M−D analysis. The results are provided at $(0.25L_1, 0.75L_2)$ within the 2D physical domain. The reference solution is derived by using 3D FEM commercial software.

	$\mathscr{H}_1\ [\times 10^{1}\mathrm{A/m}]$		$\mathscr{H}_2\ [\mathrm{A/m}]$		$\mathscr{H}_3\ [\times 10^{1}\mathrm{A/m}]$		$\mathscr{B}_1\ [\times 10^{-3}\mathrm{Wb/m^2}]$		$\mathscr{B}_2\ [\times 10^{-3}\mathrm{Wb/m^2}]$		$\mathscr{B}_3\ [\times 10^{-3}\mathrm{Wb/m^2}]$	
$\zeta\ [10^{-3}\mathrm{m}]$	3D FEM	ELDZL7	3D FEM	ELDZL7	3D FEM	ELDZL7	3D FEM	ELDZL7	3D FEM	ELDZL7	3D FEM	ELDZL7
−7.5	0.00	0.00	0.00	0.00	−7.16	−7.49	0.00	0.00	0.00	0.00	−2.66	−3.08
−6.3	−0.21	−0.21	1.16	1.15	−6.33	−6.68	−1.18	−1.18	0.64	0.64	−2.69	−3.14
−5.5	−0.34	−0.34	1.85	1.84	−5.80	−6.17	−1.87	−1.86	1.02	1.02	−2.73	−3.20
−4.3	−0.51	−0.51	2.78	2.80	−5.05	−5.45	−2.79	−2.80	1.52	1.53	−2.82	−3.33
−3.5	−0.61	−0.63	3.33	3.42	−4.57	−4.99	−3.32	−3.38	1.81	1.84	−2.90	−3.44
−3.5	−0.61	−0.63	3.33	3.42	−4.33	−4.67	−5.01	−5.10	2.73	2.78	−2.90	−3.44
−2.0	−0.76	−0.76	4.16	4.16	−3.44	−3.80	−6.19	−6.19	3.38	3.37	−3.19	−3.77
−0.5	−0.88	−0.89	4.80	4.85	−2.59	−2.98	−7.02	−7.07	3.83	3.86	−3.53	−4.15
−0.5	−0.88	−0.89	4.80	4.85	−5.37	−6.26	−1.74	−1.75	0.95	0.96	−3.53	−4.15
0.7	−1.05	−1.06	5.71	5.76	−4.80	−5.74	−1.99	−2.00	1.09	1.09	−3.61	−4.26
2.0	−1.20	−1.21	6.52	6.60	−4.23	−5.23	−2.20	−2.22	1.20	1.21	−3.70	−4.39
3.2	−1.32	−1.34	7.22	7.29	−3.68	−4.72	−2.35	−2.37	1.28	1.29	−3.80	−4.52
4.5	−1.44	−1.42	7.83	7.75	−3.12	−4.21	−2.47	−2.44	1.34	1.33	−3.90	−4.66
4.5	−1.44	−1.42	7.83	7.75	0.80	0.32	−9.79	−9.63	5.34	5.25	−3.90	−4.66
6.0	−1.39	−1.39	7.58	7.60	1.60	1.10	−8.98	−9.01	4.90	4.91	−4.38	−5.18
7.5	−1.31	−1.31	7.14	7.14	2.47	1.94	−7.82	−7.77	4.26	4.24	−4.81	−5.65

Table 6
Numerical prediction of the distribution along the thickness direction of the 3D displacement field components and temperature variation of a simply-supported rectangular plate employing higher-order ELW theories for T-D analysis. The results are provided at $(0.25L_1, 0.75L_2)$ within the 2D physical domain. The reference solution is derived by using 3D FEM commercial software.

	$U_1\ [\times 10^{-7}\mathrm{m}]$		$U_2\ [\times 10^{-7}\mathrm{m}]$		$U_3\ [\times 10^{-6}\mathrm{m}]$		$\Delta T\ [\times 10^{-1}\mathrm{K}]$	
$\zeta\ [10^{-3}\mathrm{m}]$	3D FEM	ELDZL7	3D FEM	ELDZL7	3D FEM	ELDZL7	3D FEM	ELDZL7
−7.5	−0.43	−0.43	0.23	0.23	−1.31	−1.32	−5.00	−5.00
−6.3	−0.02	−0.02	0.01	0.01	−1.32	−1.33	−4.93	−4.93
−5.5	0.25	0.25	−0.14	−0.14	−1.33	−1.34	−4.88	−4.89
−4.3	0.65	0.65	−0.35	−0.36	−1.34	−1.35	−4.82	−4.83
−3.5	0.91	0.92	−0.50	−0.50	−1.35	−1.35	−4.78	−4.79
−3.5	0.91	0.92	−0.50	−0.50	−1.35	−1.35	−4.78	−4.79
−2.0	1.40	1.41	−0.77	−0.77	−1.36	−1.36	−4.72	−4.74
−0.5	1.89	1.90	−1.03	−1.04	−1.36	−1.37	−4.67	−4.69
−0.5	1.89	1.90	−1.03	−1.04	−1.36	−1.37	−4.67	−4.69
0.7	2.31	2.32	−1.26	−1.26	−1.37	−1.37	−4.63	−4.65
2.0	2.72	2.74	−1.49	−1.49	−1.38	−1.38	−4.59	−4.62
3.2	3.14	3.16	−1.71	−1.72	−1.38	−1.39	−4.56	−4.60
4.5	3.56	3.58	−1.94	−1.95	−1.38	−1.39	−4.54	−4.58
4.5	3.56	3.58	−1.94	−1.95	−1.38	−1.39	−4.54	−4.58
6.0	4.08	4.10	−2.23	−2.23	−1.38	−1.39	−4.53	−4.57
7.5	4.61	4.63	−2.52	−2.53	−1.38	−1.39	−4.52	−4.57

Table 7
Numerical prediction of the distribution along the thickness direction of the 3D strain components of a simply-supported rectangular plate employing higher-order ELW theories for T-D analysis. The results are provided at $(0.25L_1, 0.75L_2)$ within the 2D physical domain. The reference solution is derived by using 3D FEM commercial software.

	$\varepsilon_1\ [\times 10^{-5}\mathrm{m/m}]$		$\varepsilon_2\ [\times 10^{-6}\mathrm{m/m}]$		$\gamma_{12}\ [\times 10^{-5}\mathrm{m/m}]$		$\gamma_{13}\ [\times 10^{-6}\mathrm{m/m}]$		$\gamma_{23}\ [\times 10^{-6}\mathrm{m/m}]$		$\varepsilon_3\ [\times 10^{-5}\mathrm{m/m}]$	
$\zeta\ [10^{-3}\mathrm{m}]$	3D FEM	ELDZL7	3D FEM	ELDZL7	3D FEM	ELDZL7	3D FEM	ELDZL7	3D FEM	ELDZL7	3D FEM	ELDZL7
−7.5	0.11	0.11	0.33	0.33	0.12	0.12	−0.01	0.00	0.00	0.00	−1.00	−1.00
−6.3	0.00	0.00	0.01	0.01	0.01	0.00	−0.91	−0.90	0.49	0.49	−0.91	−0.91
−5.5	−0.07	−0.07	−0.20	−0.20	−0.07	−0.07	−1.42	−1.42	0.77	0.77	−0.84	−0.85
−4.3	−0.17	−0.17	−0.51	−0.51	−0.19	−0.19	−2.06	−2.04	1.12	1.11	−0.75	−0.75
−3.5	−0.24	−0.24	−0.71	−0.72	−0.26	−0.26	−2.39	−2.35	1.30	1.28	−0.69	−0.70
−3.5	−0.24	−0.24	−0.71	−0.72	−0.26	−0.26	−2.48	−2.45	1.35	1.34	−0.65	−0.65
−2.0	−0.37	−0.37	−1.09	−1.10	−0.40	−0.40	−2.87	−2.87	1.56	1.56	−0.54	−0.54
−0.5	−0.50	−0.50	−1.48	−1.48	−0.54	−0.54	−2.99	−2.97	1.63	1.62	−0.43	−0.43
−0.5	−0.50	−0.50	−1.48	−1.48	−0.54	−0.54	−2.66	−2.65	1.45	1.45	−0.59	−0.59
0.7	−0.60	−0.61	−1.80	−1.81	−0.66	−0.66	−2.75	−2.74	1.50	1.50	−0.51	−0.51
2.0	−0.71	−0.72	−2.12	−2.13	−0.78	−0.78	−2.70	−2.68	1.47	1.46	−0.43	−0.44
3.2	−0.82	−0.83	−2.45	−2.46	−0.90	−0.90	−2.50	−2.49	1.36	1.36	−0.35	−0.36
4.5	−0.93	−0.94	−2.78	−2.79	−1.02	−1.02	−2.18	−2.19	1.18	1.19	−0.27	−0.28
4.5	−0.93	−0.94	−2.78	−2.79	−1.02	−1.02	−2.44	−2.46	1.33	1.34	−0.05	−0.06
6.0	−1.07	−1.07	−3.18	−3.19	−1.17	−1.17	−1.37	−1.34	0.74	0.73	0.06	0.06
7.5	−1.21	−1.21	−3.59	−3.61	−1.32	−1.32	−0.01	0.00	0.00	0.00	0.18	0.17

Table 8
Numerical prediction of the distribution along the thickness direction of the 3D stress components of a simply-supported rectangular plate employing higher-order ELW theories for T-D analysis. The results are provided at $(0.25L_1, 0.75L_2)$ within the 2D physical domain. The reference solution is derived by using 3D FEM commercial software.

	$\sigma_1\ [\times 10^{6}\,\mathrm{N/m^2}]$		$\sigma_2\ [\times 10^{6}\,\mathrm{N/m^2}]$		$\tau_{12}\ [\times 10^{5}\,\mathrm{N/m^2}]$		$\tau_{13}\ [\times 10^{5}\,\mathrm{N/m^2}]$		$\tau_{23}\ [\times 10^{4}\,\mathrm{N/m^2}]$		$\sigma_3\ [\times 10^{4}\,\mathrm{N/m^2}]$	
$\zeta\ [10^{-3}\mathrm{m}]$	3D FEM	ELDZL7	3D FEM	ELDZL7	3D FEM	ELDZL7	3D FEM	ELDZL7	3D FEM	ELDZL7	3D FEM	ELDZL7
−7.5	1.45	1.41	1.36	1.33	0.66	0.65	−0.01	0.00	0.02	0.00	0.05	0.00
−6.3	1.23	1.25	1.23	1.24	0.03	0.02	−0.43	−0.43	2.32	2.33	−0.04	−0.09
−5.5	1.09	1.09	1.14	1.14	−0.39	−0.39	−0.67	−0.67	3.64	3.65	−0.19	−0.24
−4.3	0.88	0.85	1.01	0.98	−1.00	−1.01	−0.97	−0.96	5.28	5.25	−0.51	−0.57
−3.5	0.74	0.69	0.92	0.87	−1.40	−1.41	−1.13	−1.11	6.13	6.05	−0.79	−0.86
−3.5	0.69	0.75	0.88	0.94	−1.47	−1.48	−1.13	−1.11	6.13	6.05	−0.80	−0.86
−2.0	0.41	0.43	0.71	0.72	−2.27	−2.28	−1.30	−1.30	7.08	7.09	−1.43	−1.48
−0.5	0.14	0.11	0.54	0.50	−3.06	−3.07	−1.35	−1.35	7.37	7.35	−2.11	−2.16
−0.5	0.39	0.40	0.73	0.74	−2.65	−2.66	−1.35	−1.35	7.37	7.35	−2.12	−2.16
0.7	0.20	0.20	0.62	0.62	−3.22	−3.24	−1.40	−1.39	7.60	7.60	−2.70	−2.74
2.0	0.02	0.01	0.51	0.50	−3.80	−3.82	−1.37	−1.36	7.47	7.44	−3.30	−3.33
3.2	−0.17	−0.15	0.40	0.42	−4.39	−4.41	−1.27	−1.27	6.92	6.91	−3.86	−3.89
4.5	−0.35	−0.28	0.29	0.37	−4.98	−5.00	−1.11	−1.11	6.02	6.07	−4.38	−4.40
4.5	−0.77	−0.87	−0.03	−0.12	−5.75	−5.78	−1.11	−1.11	6.02	6.07	−4.40	−4.40
6.0	−1.04	−1.03	−0.19	−0.18	−6.58	−6.61	−0.62	−0.61	3.36	3.32	−4.85	−4.84
7.5	−1.32	−1.37	−0.36	−0.40	−7.45	−7.47	−0.01	0.00	0.02	0.00	−5.02	−5.00

Table 9

Numerical prediction of the distribution along the thickness direction of the 3D thermal primary and secondary variables of a simply-supported rectangular plate employing higher-order ELW theories for T-D analysis. The results are provided at $(0.25L_1, 0.75L_2)$ within the 2D physical domain. The reference solution is derived by using 3D FEM commercial software.

	$\vartheta_1\ [\times 10^1 \mathrm{K/m}]$		$\vartheta_2\ [\mathrm{K/m}]$		$\vartheta_3\ [\mathrm{K/m}]$		$h_1\ [\times 10^1 \mathrm{J/m^2}]$		$h_2\ [\times 10^1 \mathrm{J/m^2}]$		$h_3\ [\times 10^1 \mathrm{J/m^2}]$	
$\zeta\ [10^{-3}\mathrm{m}]$	3D FEM	ELDZL7	3D FEM	ELDZL7	3D FEM	ELDZL7	3D FEM	ELDZL7	3D FEM	ELDZL7	3D FEM	ELDZL7
−7.5	1.31	1.31	−7.14	−7.14	−6.12	−6.00	3.96	3.97	−2.16	−2.16	−1.87	−1.84
−6.3	1.29	1.29	−7.04	−7.04	−5.77	−5.47	3.91	3.91	−2.13	−2.13	−1.77	−1.68
−5.5	1.28	1.28	−6.97	−6.98	−5.43	−5.13	3.87	3.88	−2.11	−2.12	−1.66	−1.57
−4.3	1.26	1.26	−6.88	−6.90	−4.91	−4.61	3.82	3.83	−2.09	−2.09	−1.50	−1.41
−3.5	1.25	1.26	−6.83	−6.85	−4.74	−4.28	3.79	3.80	−2.07	−2.07	−1.45	−1.31
−3.5	1.25	1.26	−6.83	−6.85	−4.22	−4.09	4.00	4.02	−2.19	−2.19	−1.35	−1.31
−2.0	1.24	1.24	−6.74	−6.77	−3.74	−3.45	3.95	3.97	−2.16	−2.17	−1.20	−1.10
−0.5	1.22	1.23	−6.67	−6.70	−3.27	−2.82	3.91	3.93	−2.13	−2.14	−1.05	−0.90
−0.5	1.22	1.23	−6.67	−6.70	−3.42	−3.25	3.35	3.36	−1.83	−1.84	−0.95	−0.90
0.7	1.21	1.22	−6.61	−6.65	−3.08	−2.74	3.32	3.34	−1.81	−1.82	−0.86	−0.76
2.0	1.20	1.21	−6.56	−6.60	−2.57	−2.23	3.29	3.32	−1.80	−1.81	−0.71	−0.62
3.2	1.19	1.20	−6.52	−6.57	−2.07	−1.73	3.27	3.30	−1.79	−1.80	−0.58	−0.48
4.5	1.19	1.20	−6.49	−6.54	−1.74	−1.22	3.26	3.28	−1.78	−1.79	−0.48	−0.34
4.5	1.19	1.20	−6.49	−6.54	−1.21	−1.06	3.80	3.84	−2.08	−2.09	−0.39	−0.34
6.0	1.18	1.20	−6.46	−6.52	−0.76	−0.45	3.79	3.83	−2.07	−2.09	−0.24	−0.14
7.5	1.18	1.20	−6.45	−6.52	−0.31	0.16	3.78	3.83	−2.07	−2.09	−0.10	0.05

Table 10

Numerical prediction of the distribution along the thickness direction of the 3D displacement field components and moisture concentration variation of a simply-supported rectangular plate employing higher-order ELW theories for H-D analysis. The results are provided at $(0.25L_1, 0.75L_2)$ within the 2D physical domain. The reference solution is derived by using 3D FEM commercial software.

	$U_1\ [\times 10^{-7}\mathrm{m}]$		$U_2\ [\times 10^{-7}\mathrm{m}]$		$U_3\ [\times 10^{-6}\mathrm{m}]$		$\Delta C\ [\times 10^1 \mathrm{kg/m^3}]$	
$\zeta\ [10^{-3}\mathrm{m}]$	3D FEM	ELDZL7	3D FEM	ELDZL7	3D FEM	ELDZL7	3D FEM	ELDZL7
−7.5	−2.17	−2.17	1.19	1.19	−1.04	−1.04	−1.00	−1.00
−6.3	−1.85	−1.85	1.01	1.01	−1.05	−1.04	−0.74	−0.74
−5.5	−1.64	−1.64	0.90	0.90	−1.05	−1.05	−0.56	−0.56
−4.3	−1.33	−1.33	0.73	0.73	−1.05	−1.05	−0.30	−0.30
−3.5	−1.13	−1.13	0.62	0.62	−1.06	−1.05	−0.12	−0.11
−3.5	−1.13	−1.13	0.62	0.62	−1.06	−1.05	−0.12	−0.11
−2.0	−0.75	−0.75	0.41	0.41	−1.06	−1.06	0.17	0.17
−0.5	−0.38	−0.38	0.21	0.21	−1.06	−1.06	0.47	0.47
−0.5	−0.38	−0.38	0.21	0.21	−1.06	−1.06	0.47	0.47
0.7	−0.07	−0.07	0.04	0.04	−1.06	−1.06	0.82	0.82
2.0	0.24	0.24	−0.13	−0.13	−1.06	−1.06	1.18	1.18
3.2	0.56	0.55	−0.30	−0.30	−1.06	−1.06	1.53	1.54
4.5	0.87	0.87	−0.48	−0.47	−1.06	−1.05	1.89	1.88
4.5	0.87	0.87	−0.48	−0.47	−1.06	−1.05	1.89	1.88
6.0	1.26	1.25	−0.69	−0.68	−1.05	−1.05	2.19	2.20
7.5	1.66	1.65	−0.90	−0.90	−1.04	−1.04	2.50	2.50

that kinematic conditions are always satisfied at the top and bottom surfaces. Similar observations apply to the stress components presented in Table 4. However, in-plane stresses maintain linear distributions with minor variations between layers, while out-of-plane shear stresses exhibit parabolic profiles. Finally, the σ_3 distribution perfectly satisfies the loading conditions at the top and bottom surfaces. Table 5 presents the through-the-thickness distributions of the magnetic primary and secondary variables. Similarly to the magnetic potential in Table 2, the in-plane magnetic field components exhibit characteristic zigzag profiles, while $\mathscr{H}_3$ shows a stepwise linear distribution. In Table 6, the results for the T-D analysis demonstrate that the in-plane displacement field components are distributed linearly along the thickness direction, whereas the U_3 component exhibits a more complex profile. A polynomial distribution is observed in the temperature variation profile. A perfect agreement is achieved at the bottom surface between the ELDZL7 model and 3D FEM results, since a specific value of temperature variation is enforced at this location through a kinematic constraint. At the top surface, however, where a thermal flux is applied, a lower accuracy is observed for the thermal configuration variable. Table 7 shows that $\varepsilon_1, \varepsilon_2$ and γ_{12} are linearly distributed along the thickness direction, while ε_3 exhibits some discontinuities at the interface between adjacent laminae. The out-of-plane distortions γ_{13} and γ_{23} assume null values at the top and bottom surfaces, while their profile exhibit interfacial steps across the thickness. Regarding the 3D stress components, Table 8 shows that, at the selected points, the in-plane strain components are linearly distributed, whereas the in-plane stresses exhibit some discontinuous linear profiles due to the varying stiffness of each layer in the lamination scheme. On the other hand, the recovered profiles for the out-of-plane shear stresses τ_{13} and τ_{23} display parabolic distributions with characteristic zigzag patterns at each interfaces, while σ_3 follows a polynomial distribution. The ELDZL7 model aligns consistently with the reference solution, reflecting accurately the loading conditions. The distributions of the in-plane temperature gradient components ϑ_1 and ϑ_2, as reported in Table 9, closely reflect that one of the temperature variation profile, whereas ϑ_3 exhibits a discontinuous linear distribution. On the contrary, in-plane thermal flux components h_1 and h_2 show discontinuous distributions, while h_3 presents a linear profile. The final validation is conducted for an H-D analysis on the same plate. As shown in Table 10, which presents the results at $(0.25L_1, 0.75L_2)$ in terms of unknown variables of the formulation, the in-plane displacement field components exhibit linear distributions, while U_3 displays a parabolic dispersion with a zigzag profile near the reference surface. In contrast, ΔC is linear along the thickness direction, with slope changes at each interface. These numerical predictions match well with the 3D FEM

Table 11

Numerical prediction of the distribution along the thickness direction of the 3D strain components of a simply-supported rectangular plate employing higher-order ELW theories for H-D analysis. The results are provided at $(0.25L_1, 0.75L_2)$ within the 2D physical domain. The reference solution is derived by using 3D FEM commercial software.

	$\varepsilon_1\ [\times 10^{-6}\mathrm{m/m}]$		$\varepsilon_2\ [\times 10^{-6}\mathrm{m/m}]$		$\gamma_{12}\ [\times 10^{-6}\mathrm{m/m}]$		$\gamma_{13}\ [\times 10^{-6}\mathrm{m/m}]$		$\gamma_{23}\ [\times 10^{-6}\mathrm{m/m}]$		$\varepsilon_3\ [\times 10^{-6}\mathrm{m/m}]$	
$\zeta\ [10^{-3}\mathrm{m}]$	3D FEM	ELDZL7	3D FEM	ELDZL7	3D FEM	ELDZL7	3D FEM	ELDZL7	3D FEM	ELDZL7	3D FEM	ELDZL7
−7.5	5.69	5.69	1.69	1.69	6.21	6.21	−0.01	0.00	0.00	0.00	−5.50	−5.50
−6.3	4.85	4.85	1.44	1.44	5.29	5.29	−0.88	−0.88	0.48	0.48	−4.56	−4.56
−5.5	4.30	4.30	1.28	1.28	4.69	4.69	−1.38	−1.38	0.75	0.75	−3.95	−3.95
−4.3	3.49	3.49	1.04	1.04	3.81	3.80	−2.00	−1.99	1.09	1.08	−3.05	−3.05
−3.5	2.96	2.95	0.88	0.88	3.22	3.22	−2.33	−2.30	1.27	1.25	−2.46	−2.44
−3.5	2.96	2.95	0.88	0.88	3.22	3.22	−2.42	−2.39	1.32	1.30	−2.63	−2.61
−2.0	1.97	1.97	0.59	0.59	2.15	2.15	−2.90	−2.89	1.58	1.58	−1.44	−1.44
−0.5	1.00	1.00	0.30	0.30	1.09	1.10	−3.12	−3.12	1.70	1.70	−0.25	−0.25
−0.5	1.00	1.00	0.30	0.30	1.09	1.10	−2.78	−2.78	1.51	1.52	−0.56	−0.56
0.7	0.19	0.19	0.06	0.06	0.20	0.21	−2.80	−2.80	1.52	1.53	0.16	0.16
2.0	−0.63	−0.63	−0.19	−0.19	−0.69	−0.69	−2.71	−2.69	1.47	1.47	0.89	0.89
3.2	−1.46	−1.45	−0.43	−0.43	−1.59	−1.58	−2.48	−2.47	1.35	1.35	1.62	1.62
4.5	−2.29	−2.28	−0.68	−0.68	−2.49	−2.48	−2.14	−2.16	1.17	1.18	2.36	2.35
4.5	−2.29	−2.28	−0.68	−0.68	−2.49	−2.48	−2.40	−2.43	1.31	1.32	4.34	4.33
6.0	−3.29	−3.28	−0.98	−0.98	−3.59	−3.58	−1.35	−1.32	0.73	0.72	5.57	5.57
7.5	−4.34	−4.33	−1.29	−1.29	−4.73	−4.72	−0.01	0.00	0.00	0.00	6.85	6.85

Table 12

Numerical prediction of the distribution along the thickness direction of the 3D stress components of a simply-supported rectangular plate employing higher-order ELW theories for H-D analysis. The results are provided at $(0.25L_1, 0.75L_2)$ within the 2D physical domain. The reference solution is derived by using 3D FEM commercial software.

	$\sigma_1\ [\times 10^{6}\,\mathrm{N/m^2}]$		$\sigma_2\ [\times 10^{6}\,\mathrm{N/m^2}]$		$\tau_{12}\ [\times 10^{5}\,\mathrm{N/m^2}]$		$\tau_{13}\ [\times 10^{5}\,\mathrm{N/m^2}]$		$\tau_{23}\ [\times 10^{4}\,\mathrm{N/m^2}]$		$\sigma_3\ [\times 10^{4}\,\mathrm{N/m^2}]$	
$\zeta\ [10^{-3}\mathrm{m}]$	3D FEM	ELDZL7	3D FEM	ELDZL7	3D FEM	ELDZL7	3D FEM	ELDZL7	3D FEM	ELDZL7	3D FEM	ELDZL7
−7.5	1.25	1.21	0.82	0.78	3.34	3.34	0.00	0.00	0.02	0.00	0.03	0.00
−6.3	1.04	1.06	0.67	0.69	2.85	2.85	−0.41	−0.41	2.25	2.26	−0.08	−0.09
−5.5	0.90	0.91	0.58	0.58	2.53	2.52	−0.65	−0.65	3.53	3.55	−0.22	−0.23
−4.3	0.70	0.67	0.44	0.41	2.05	2.05	−0.94	−0.94	5.13	5.11	−0.53	−0.56
−3.5	0.56	0.52	0.34	0.30	1.74	1.73	−1.10	−1.08	5.97	5.91	−0.81	−0.83
−3.5	0.61	0.64	0.38	0.41	1.82	1.82	−1.10	−1.08	5.97	5.91	−0.81	−0.83
−2.0	0.33	0.36	0.18	0.20	1.22	1.22	−1.31	−1.31	7.16	7.15	−1.44	−1.45
−0.5	0.06	0.05	−0.02	−0.03	0.62	0.62	−1.41	−1.41	7.69	7.70	−2.14	−2.15
−0.5	0.11	0.09	0.04	0.02	0.53	0.54	−1.41	−1.41	7.69	7.70	−2.15	−2.15
0.7	−0.06	−0.07	−0.07	−0.09	0.10	0.10	−1.42	−1.42	7.74	7.75	−2.75	−2.75
2.0	−0.23	−0.24	−0.18	−0.19	−0.34	−0.34	−1.38	−1.37	7.49	7.46	−3.35	−3.35
3.2	−0.40	−0.37	−0.30	−0.28	−0.78	−0.77	−1.26	−1.26	6.86	6.85	−3.91	−3.90
4.5	−0.56	−0.46	−0.41	−0.31	−1.22	−1.22	−1.09	−1.10	5.93	6.00	−4.43	−4.41
4.5	−0.99	−1.12	−0.80	−0.94	−1.41	−1.40	−1.09	−1.10	5.93	6.00	−4.45	−4.41
6.0	−1.27	−1.25	−1.01	−0.99	−2.03	−2.02	−0.61	−0.60	3.31	3.26	−4.89	−4.84
7.5	−1.56	−1.63	−1.21	−1.28	−2.67	−2.67	0.00	0.00	0.02	0.00	−5.04	−5.00

Table 13

Numerical prediction of the distribution along the thickness direction of the3D hygrometric primary and secondary variables of a simply-supported rectangular plate employing higher-order ELW theories for H-D analysis. The results are provided at $(0.25L_1, 0.75L_2)$ within the 2D physical domain. The reference solution is derived by using 3D FEM commercial software.

	$\lambda_1\ [\times 10^{1}\mathrm{kg/m^4}]$		$\lambda_2\ [\mathrm{kg/m^4}]$		$\lambda_3\ [\mathrm{kg/m^4}]$		$c_1\ [\times 10^{-7}\mathrm{kg/m^2}]$		$c_2\ [\times 10^{-8}\mathrm{kg/m^2}]$		$c_3\ [\times 10^{-7}\mathrm{kg/m^2}]$	
$\zeta\ [10^{-3}\mathrm{m}]$	3D FEM	ELDZL7	3D FEM	ELDZL7	3D FEM	ELDZL7	3D FEM	ELDZL7	3D FEM	ELDZL7	3D FEM	ELDZL7
−7.5	0.26	0.26	−0.14	−0.14	−2.20	−2.28	0.35	0.35	−1.89	−1.89	−3.16	−3.27
−6.3	0.19	0.19	−0.11	−0.11	−2.19	−2.27	0.26	0.26	−1.39	−1.39	−3.15	−3.26
−5.5	0.15	0.15	−0.08	−0.08	−2.19	−2.27	0.19	0.20	−1.06	−1.06	−3.15	−3.26
−4.3	0.08	0.08	−0.04	−0.04	−2.19	−2.27	0.10	0.10	−0.56	−0.56	−3.14	−3.26
−3.5	0.03	0.03	−0.02	−0.02	−2.19	−2.27	0.04	0.04	−0.23	−0.21	−3.14	−3.26
−3.5	0.03	0.03	−0.02	−0.02	−1.96	−2.03	0.05	0.05	−0.28	−0.25	−3.14	−3.26
−2.0	−0.04	−0.04	0.02	0.02	−1.96	−2.04	−0.07	−0.07	0.39	0.38	−3.14	−3.26
−0.5	−0.12	−0.12	0.07	0.07	−1.96	−2.05	−0.19	−0.20	1.06	1.08	−3.14	−3.27
−0.5	−0.12	−0.12	0.07	0.07	−2.84	−2.95	−0.12	−0.12	0.65	0.66	−3.15	−3.27
0.7	−0.21	−0.22	0.12	0.12	−2.84	−2.96	−0.21	−0.21	1.15	1.15	−3.15	−3.28
2.0	−0.31	−0.31	0.17	0.17	−2.85	−2.97	−0.30	−0.30	1.65	1.66	−3.16	−3.30
3.2	−0.40	−0.40	0.22	0.22	−2.86	−2.99	−0.39	−0.40	2.15	2.16	−3.18	−3.32
4.5	−0.50	−0.49	0.27	0.27	−2.88	−3.01	−0.49	−0.48	2.66	2.64	−3.19	−3.34
4.5	−0.50	−0.49	0.27	0.27	−2.00	−2.09	−0.79	−0.79	4.32	4.30	−3.21	−3.34
6.0	−0.57	−0.58	0.31	0.31	−2.03	−2.12	−0.92	−0.92	5.01	5.02	−3.24	−3.39
7.5	−0.65	−0.65	0.36	0.36	−2.05	−2.15	−1.05	−1.05	5.71	5.71	−3.28	−3.44

Table 14

Static deflection two-layered square plates of various sizes under thermal temperature loads. Comparison and validation against existing literature and effect of the maximum polynomial order in the kinematic expansion. The maximum vertical deflection U_3 is presented in 10^{-3} m.

$L_1 = L_2$ [m]	2	5	10	50	100
LD4-L – [17]	0.0014	0.0141	0.0587	1.4857	5.9448
LD4-T – [17]	0.0009	0.0137	0.0585	1.4855	5.9446
LD4-TD – [17]	0.0012	0.0116	0.0553	1.4818	5.9409
ELD4	0.0014	0.0117	0.0553	1.4818	5.9407
ELDZL4	0.0014	0.0116	0.0551	1.4816	5.9407
ELD5	0.0012	0.0117	0.0554	1.4818	5.9408
ELDZL5	0.0012	0.0116	0.0552	1.4817	5.9408
ELD6	0.0012	0.0117	0.0553	1.4818	5.9408
ELDZL6	0.0011	0.0116	0.0552	1.4817	5.9408
ELD7	0.0012	0.0117	0.0554	1.4818	5.9408
ELDZL7	0.0012	0.0116	0.0553	1.4818	5.9409

reference solution, demonstrating a high accuracy. Similarly, an excellent agreement is observed between ELW results and the 3D FEM reference solution for the strain components reported in Table 11. The in-plane strains $\varepsilon_1, \varepsilon_2$ and γ_{12} exhibit a linear through-the-thickness distribution. Regarding the out-of-plane components, ε_3 shows a linear dispersion along the thickness direction within each layer, with step variations at the interfaces but without any slope change. On the other hand, γ_{13} and γ_{23} display some parabolic distributions within each lamina, with stepwise profiles. Finally, ε_3 exhibits a stepwise linear distribution along the thickness direction. Due to the variation in the material properties along the thickness, the in-plane strain components are linearly distributed, but Table 12 reveals that in-plane stress components σ_1 and σ_2 are characterized by linear distributions with stepwise variations between adjacent layers. A similar behavior is observed for the in-plane shear stress component τ_{12}. In contrast, a continuous smooth profile is observed for σ_3, starting from a null value at $\zeta = -h/2$ to approximately $-5 \times 10^4\ \mathrm{N/m^2}$ at $\zeta = -h/2$, consistently with the mechanical loading conditions. Similarly, the out-of-plane shear stresses τ_{13} and τ_{13} are continuously distributed along the thickness direction, with a slope change at the interface among layers within the laminate. Finally, Table 13 presents the simulation results in terms of mass concentration gradient components and mass flux components. A linear distribution with slope variation is found for the in-plane primary variables λ_1 and λ_2, while a stepwise distribution characterizes λ_3. Note, also, that the in-plane components predicted using the ELDZL7 simulation match those from the reference solution, with highly comparable results also for λ_3.

To further validate the model, some comparisons with the results from existing literature are considered. To this end, a thermo-mechanical analysis is conducted on a simply-supported square mechanical plate of dimensions $L_1 = L_2$ under thermo-mechanical loads. The structure consists of two layers of equal thickness $h_1 = h_2 = 0.5\ \mathrm{m}$ made of a composite material with density $\rho^{(k)} = 1500\ \mathrm{kg/m^3}$, whose orthotropic mechanical properties are expressed in terms of the engineering constants reported in the following:

$$\begin{gathered} E_1^{(k)} = 172.37\ \mathrm{GPa}, \quad E_2^{(k)} = E_3^{(k)} = 6.895\ \mathrm{GPa} \\ G_{12}^{(k)} = G_{13}^{(k)} = 3.447\ \mathrm{GPa}, \quad G_{23}^{(k)} = 1.379\ \mathrm{GPa} \\ \nu_{12}^{(k)} = \nu_{13}^{(k)} = \nu_{23}^{(k)} = 0.25 \end{gathered} \tag{107}$$

In addition, the thermal expansion coefficients are set as $a_{11}^{(k)} = 1\ 1/\mathrm{K}$ and $a_{22}^{(k)} = a_{33}^{(k)} = 1125\ 1/\mathrm{K}$. The lamination scheme is $(0/90)$. The two-layered panel is subjected to a sinusoidal distribution of temperature variation at the top surface, located at $\zeta = h/2$, with magnitude $\Delta\overline{\mathrm{T}}_s^{(+)} = 1\ \mathrm{K}$ for $\widetilde{M} = \widetilde{M} = 1$. On the other hand, a null temperature variation is prescribed at the bottom surface, namely $\Delta\overline{\mathrm{T}}_s^{(-)} = 0\ \mathrm{K}$. The vertical deflection at the center of the plate is evaluated by using various kinematic models for different dimensions of the plate, ranging from $L_1 = L_2 = 2\ \mathrm{m}$ which corresponds to a very thick plate, to $L_1 = L_2 = 100\ \mathrm{m}$, associated with a very thin laminate. The results are successfully compared in Table 14 to those derived from 3D simulations carried out in Ref. [17]. In particular, the simulation identified with “LD4-L” is evaluated with a layer-wise magneto-mechanical model with a fourth-order polynomial, which assumes a linear distribution of the temperature variation along the thickness direction. Furthermore, “LD4-T” results are taken from the same reference starting from a through-the-thickness temperature profile derived from the solution of the one-dimensional Fourier equation. Finally, solution “LD4-TD” is derived from a Layer-Wise simulation with complete thermo-mechanical coupling. As can be seen, for each geometric size of the plate, the results from higher-order kinematic field perfectly match those from “LD4-TD” simulation, while some discrepancies are seen between the results from the present model and those ones from “LD4-L” and “LD4-T”, because the model proposed in this research is fully coupled. At this point, an additional simulation is conducted on a single layered rectangular plate with magneto-mechanical properties. The single layer is made up of cobalt ferrite, whose multifield properties are reported in Table 1. The total thickness of the plate is $h_1 = h = 0.3\ \mathrm{m}$, and the dimensions are $L_1 = L_2 = 1\ \mathrm{m}$. The plate is simply-supported, and it is under magnetic sensor configuration. In other words, no external magnetic fields are applied at the top and bottom surface, and a sinusoidal mechanical pressure with magnitude $\overline{q}_3^{(+)} = 1\ \mathrm{N/m^2}$ and wave numbers $\widetilde{M} = \widetilde{M} = 1$ is applied from the top surface. The magneto-mechanical response of the plate is evaluated with various higher-order theories, considering both ESL and ELW kinematic assumptions. The results are provided in Table 15 in terms of the through-the-thickness distribution of displacement field components U_1, U_3 and scalar magnetic potential variation $\Delta\psi$. In particular, the in-plane component U_1 is taken at $(0, 0.5L_2)$, while U_3 and $\Delta\Psi$ are evaluated $(0.5L_1, 0.5L_2)$ within the 2D physical domain. The simulation is validated against the results taken from literature. Refs. [14] and [15] contain the results from 3D simulations based on exponential matrix method and discrete layer approximation method, respectively. The present 2D refined theory can predict well the through-the-thickness distribution of the magneto-mechanical configuration variables derived from 3D simulations. In particular, a very high accuracy level is observed for displacement field components, and the predictions in terms of temperature variation agree with those from literature at both the upper and lower surface region, as well as in the mid-thickness of the panel.

Once the semi-analytical formulation has been validated against the 3D FEM results and those from literature, further investigations are conducted on a rectangular plate to study the convergence of results for different load shapes. In addition, the effect of multifield coupling is examined by selectively activating the terms within the constitutive matrix that couple primary and secondary variables of the various

Table 15
Magneto-mechanical response of a single layered thick rectangular plate employing various higher-order equivalent layer-wise and equivalent single layer kinematic model. Comparison against literature results from 3D analysis.

$U_1\ [10^{-12}\ \mathrm{m}]$										
$(\zeta+h/2)/h$	3D [14]	3D [15]	ED4	ELD4	ED5	ELD5	ED6	ELD6	ED7	ELD7
0	3.20	3.20	3.20	3.20	3.20	3.20	3.20	3.20	3.20	3.20
1/3	1.08	1.08	1.09	1.09	1.10	1.10	1.10	1.10	1.10	1.09
2/3	−0.47	−0.47	−0.43	−0.43	−0.43	−0.43	−0.43	−0.43	−0.43	−0.44
1	−2.77	−2.77	−2.77	−2.77	−2.77	−2.77	−2.77	−2.77	−2.77	−2.76
$U_3\ [10^{-11}\ \mathrm{m}]$										
$(\zeta+h/2)/h$	3D [14]	3D [15]	ED4	ELD4	ED5	ELD5	ED6	ELD6	ED7	ELD7
0	0.92	0.92	0.92	0.92	0.92	0.92	0.92	0.92	0.92	0.92
1/3	1.01	1.01	1.01	1.01	1.01	1.01	1.01	1.01	1.01	1.01
2/3	1.04	1.04	1.04	1.04	1.04	1.04	1.04	1.04	1.04	1.04
1	1.01	1.01	1.01	1.01	1.01	1.01	1.01	1.01	1.01	1.01
$\Delta\Psi [10^{-6}\ \mathrm{A}]$										
$(\zeta+h/2)/h$	3D [14]	3D [15]	ED4	ELD4	ED5	ELD5	ED6	ELD6	ED7	ELD7
0	−5.20	−5.20	−5.20	−5.20	−5.20	−5.20	−5.20	−5.20	−5.20	−5.20
1/3	−4.91	−4.91	−4.91	−4.91	−4.92	−4.92	−4.92	−4.92	−4.92	−4.92
2/3	−2.66	−2.66	−2.72	−2.72	−2.71	−2.71	−2.71	−2.71	−2.71	−2.71
1	0.04	0.04	0.04	0.04	0.04	0.04	0.04	0.04	0.04	0.04

physical problems. For these analyses, a simply-supported rectangular plate consisting of four layers with thicknesses $h_1 = 4\times10^{-3}$ m, $h_2 = h_4 = 3\times10^{-3}$ m and $h_3 = 5\times10^{-3}$ m is considered. The lamination scheme is identical to the previous example, and the geometric dimensions of the plate along α_1 and α_2 directions are $L_1 = 1.2\times10^{-1}$ m and $L_2 = 2.2\times10^{-1}$ m, respectively. At the top surface of the plate, a mechanical load with magnitude $\overline{q}_3^{(+)} = -1\times10^5\ \mathrm{N/m^2}$ is applied. The surface load distribution is referred to as a ring load, since it is applied near the boundaries of the plate, leaving the central part of the panel unloaded. This distribution is achieved by superimposing a uniform load

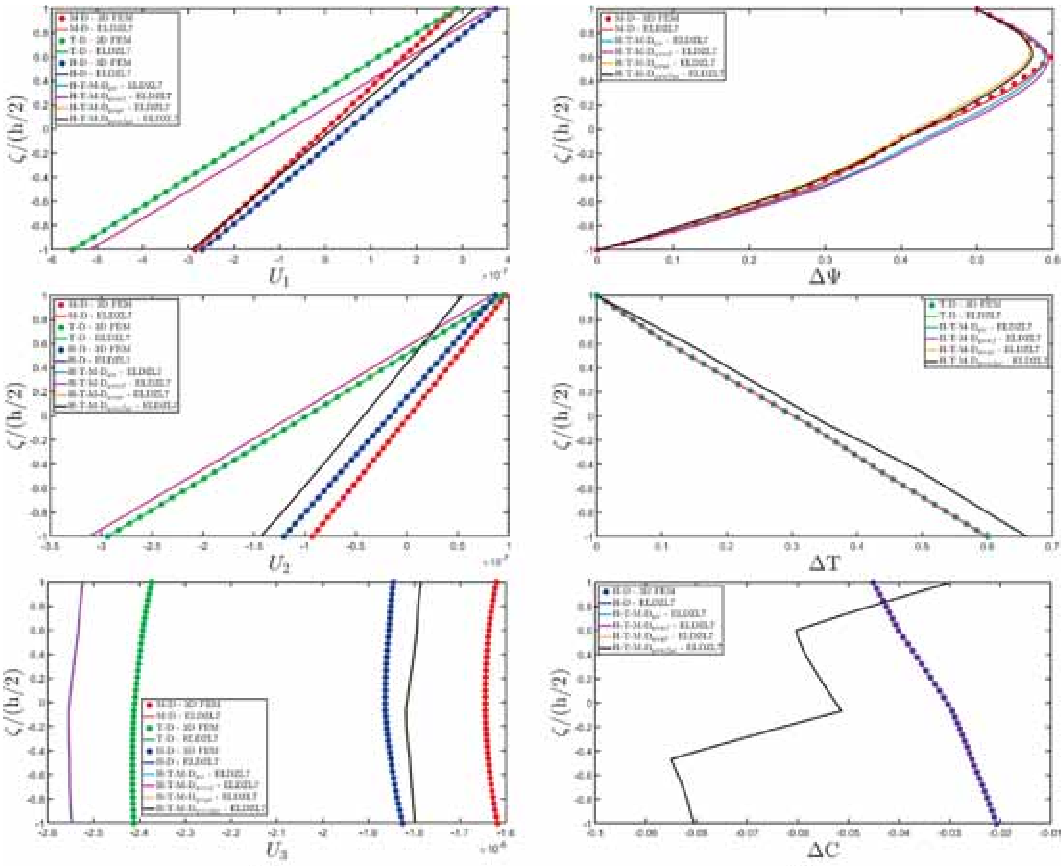

(a) (b)

Fig. 2. Through-the-thickness distribution of displacement field components (a) and multifield configuration variables (b) of a rectangular plate subjected to hygrometric, thermal, magnetic, and mechanical loading conditions with various surface distributions for the point located at $(s_1, s_2) = (0.25L_1, 0.25L_2)$. Effect of multiphysics coupling and comparison against numerical predictions from 3D FEM.

and a patch load with equal magnitude but opposite direction. A similar load distribution is applied at the top surface for the mass flux, with the corresponding load magnitude equal to $\overline{q}_{\mathrm{C}}^{(+)} = 2.8 \times 10^{-7}\,\mathrm{kg/m^2}$. The semi-analytical coefficient $Q_{\alpha snm}^{(\pm)}$ with $\alpha = 3, \mathrm{C}$ for each $n = 1, \ldots, \widetilde{N}$ and $m = 1, \ldots, \widetilde{M}$ for the uniform load is expressed as follows:

$$Q_{\alpha snm}^{(\pm)} = \frac{4\overline{q}_{\alpha}^{(\pm)}}{\pi^2 nm}(1 - \cos(n\pi))(1 - \cos(m\pi)) \tag{108}$$

On the other hand, the patch load distribution is defined as follows:

$$q_{\alpha}^{(\pm)}(s_1, s_2) = \begin{cases} -\overline{q}_{\alpha}^{(\pm)} \quad \text{for} & \begin{array}{l} s_1 \in [(s_{10} - c_{10}), (s_{10} + c_{10})] \\ s_2 \in [(s_{20} - c_{20}), (s_{20} + c_{20})] \end{array} \\ \quad 0 \quad \text{otherwise} \end{cases} \tag{109}$$

As can be seen, this load distribution is centered at $(s_{10}, s_{20}) = (0.5L_1, 0.5L_2)$, and the corresponding shape parameters are $c_{10} = 3/8L_1$ and $c_{20} = 1/8L_2$, which define the extension of the loaded area along α_1 and α_2 directions, respectively. The semi-analytical coefficient for Eq. (109) is reported in the following for any n, m:

$$Q_{\alpha snm}^{(\pm)} = -\frac{16\overline{q}_{\alpha}^{(\pm)}}{\pi^2 nm}\sin\left(\frac{n\pi s_{10}}{L_1}\right)\sin\left(\frac{m\pi s_{20}}{L_2}\right)\sin\left(\frac{n\pi c_{10}}{L_1}\right)\sin\left(\frac{m\pi c_{20}}{L_2}\right) \tag{110}$$

On the other hand, a uniform distribution of mass flux is applied to the bottom of the plate, assuming $\overline{q}_{\mathrm{C}}^{(-)} = 1.6 \times 10^{-7}\,\mathrm{kg/m^2}$. Regarding the magnetic field, the loading condition consists of prescribed values of the magnetic potential at the top and bottom surfaces with sinusoidal distributions. In particular, the magnitude of magnetic potential is given by $\Delta\overline{\Psi}_s^{(+)} = 1\,\mathrm{A}$ and $\Delta\overline{\Psi}_s^{(-)} = 0\,\mathrm{A}$. Finally, a null temperature variation is assumed at the top surface by setting $\Delta\overline{\mathrm{T}}_s^{(+)} = 0\,\mathrm{K}$, while a hydrostatic thermal flux oriented along α_2 is applied at the bottom surface with magnitude $\overline{q}_{\mathrm{T}}^{(+)} = 5 \times 10^2\,\mathrm{J/m^2}$. The thermal flux follows the distribution $q_{\alpha}^{(\pm)}(s_1, s_2) = \overline{q}_{\alpha}^{(\pm)}(s_2/L_2)$ with $\alpha = \mathrm{T}$. The corresponding semi-analytical coefficients for trigonometric expansion are:

$$Q_{\alpha snm}^{(\pm)} = -\frac{4\overline{q}_{\alpha}^{(\pm)}}{\pi^2 nm}(1 - \cos(n\pi))\cos(m\pi) \tag{111}$$

The numerical investigations on this structure are conducted using the ELDZL7 kinematic model, and the results are provided in Figs. 2-7, **showing the thickness plots of multifield configuration, primary, and secondary variables at** $(s_1, s_2) = (0.25L_1, 0.25L_2)$. The semi-analytical solution is derived by assuming $\widetilde{N} = \widetilde{M} = 150$. These parameters are selected to ensure the convergence of results for M−D, T-D, and H-D simulations. Furthermore, for these cases, a comparison with 3D FEM numerical predictions is performed to validate the results. The finite element model is developed using a commercial software, employing parabolic brick elements, and consists of a structured mesh with 576695 nodes. In addition, H-T-M−D coupled simulations are conducted using higher-order theories, with different couplings between the involved physical phenomena to observe the influence of the various multifield interactions on the overall structural response. In particular, the acronym H - T - M - D$_{qze}$ accounts for thermal and hygroscopic expansion phenomena, along with the piezomagnetic effect, while the relation $\overline{\boldsymbol{\Gamma}}_{\mathrm{w}}^{(k)} = \overline{\boldsymbol{\Gamma}}_{\mathrm{f}}^{(k)} = \overline{\boldsymbol{\Gamma}}_{\mathrm{TC}}^{(k)} = \overline{\boldsymbol{\Gamma}}_{\mathrm{Y}}^{(k)} = \overline{\boldsymbol{\Gamma}}_{\mathrm{X}}^{(k)} = \mathbf{0}$ is assumed. Furthermore, H - T - M - D$_{qzewf}$ simulation considers also pyromagnetic and

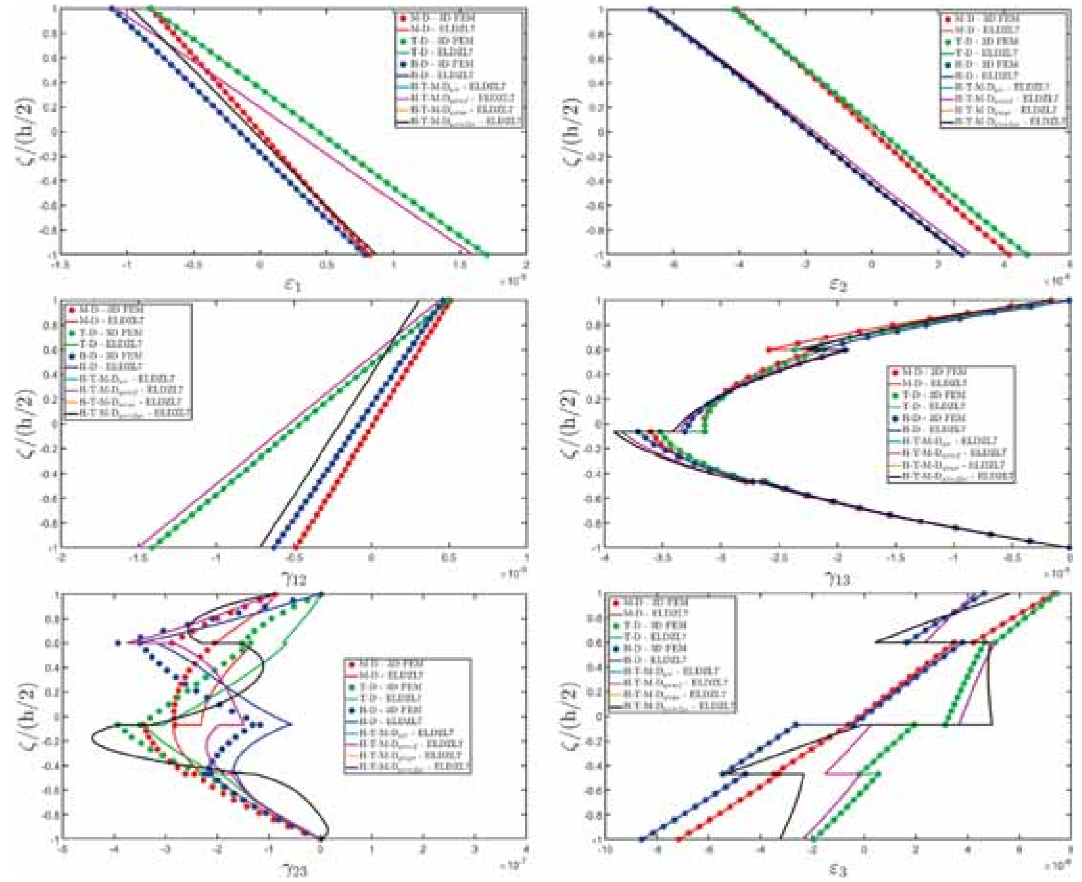

Fig. 3. Through-the-thickness distribution of 3D strain components of a rectangular plate subjected to hygrometric, thermal, magnetic, and mechanical loading conditions with various surface distributions for the point located at $(s_1, s_2) = (0.25L_1, 0.25L_2)$. Effect of multiphysics coupling and comparison against numerical predictions from 3D FEM.

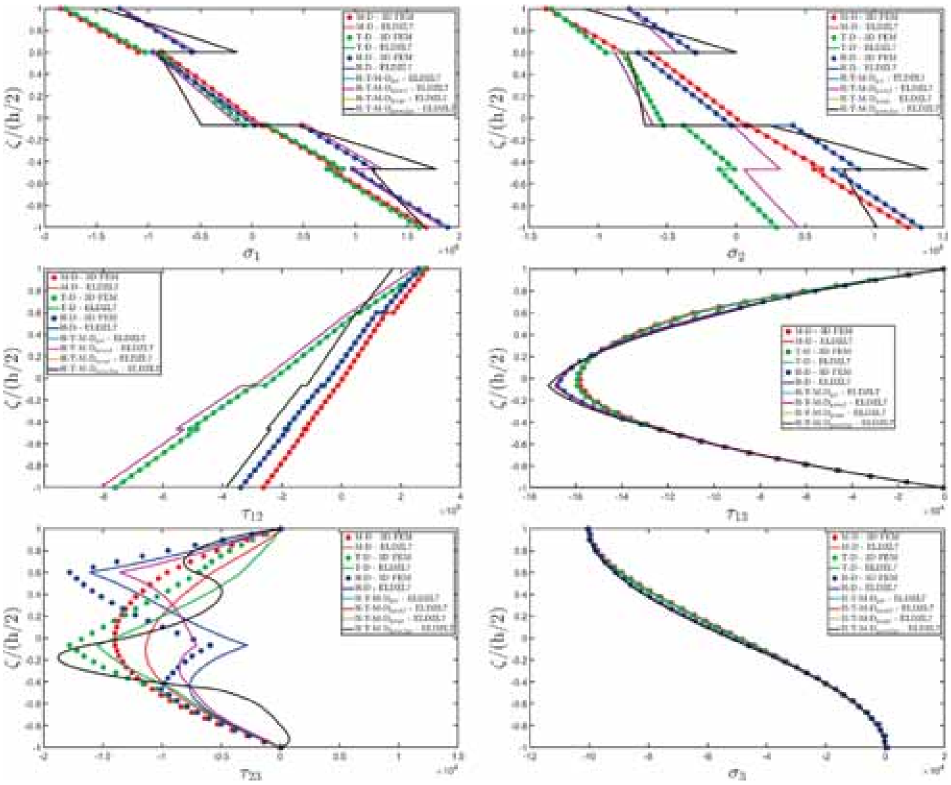

Fig. 4. Through-the-thickness distribution of 3D stress components of a rectangular plate subjected to hygrometric, thermal, magnetic, and mechanical loading conditions with various surface distributions for the point located at $(s_1, s_2) = (0.25L_1, 0.25L_2)$. Effect of multiphysics coupling and comparison against numerical predictions from 3D FEM.

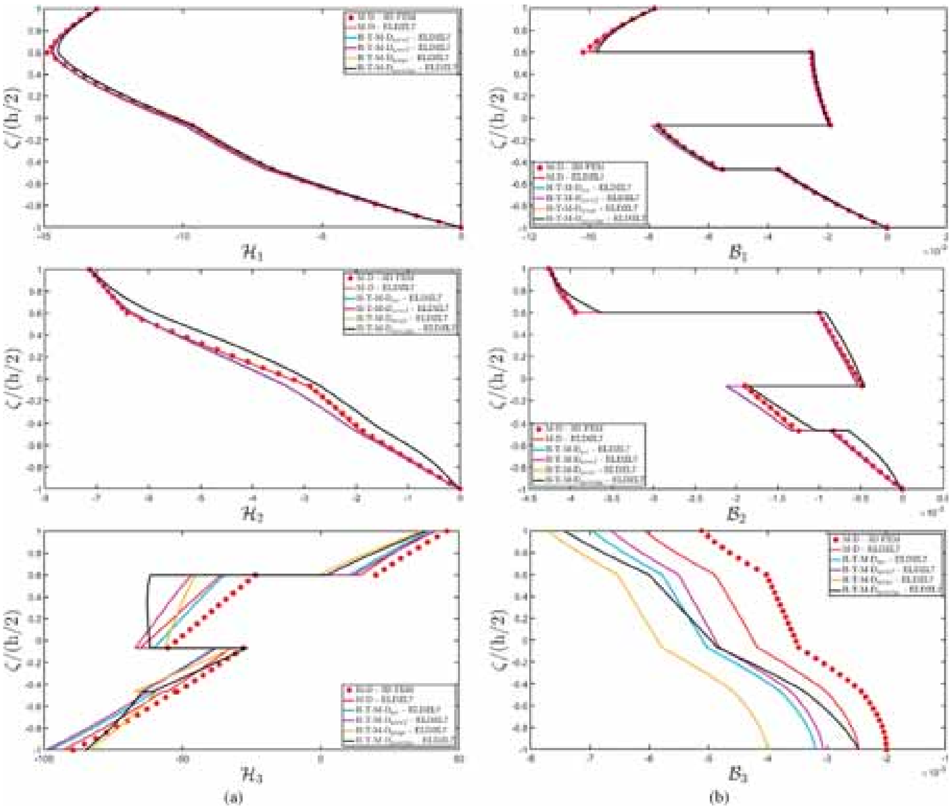

Fig. 5. Through-the-thickness distribution of magnetic primary (a) and secondary (b) variables of a rectangular plate subjected to hygrometric, thermal, magnetic, and mechanical loading conditions with various surface distributions for the point located at $(s_1, s_2) = (0.25L_1, 0.25L_2)$. Effect of multiphysics coupling and comparison against numerical predictions from 3D FEM.

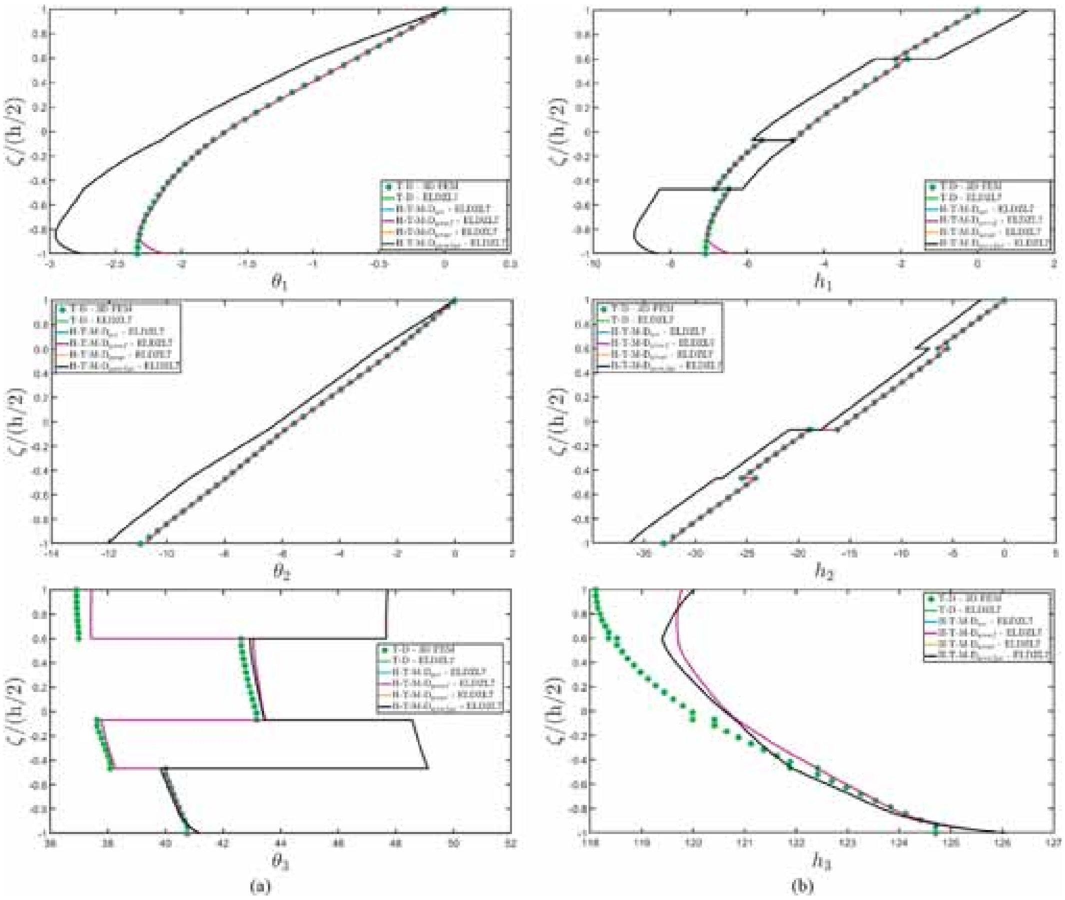

(a)
(b)

Fig. 6. Through-the-thickness distribution of thermal primary (a) and secondary (b) variables of a rectangular plate subjected to hygrometric, thermal, magnetic, and mechanical loading conditions with various surface distributions for the point located at $(s_1, s_2) = (0.25L_1, 0.25L_2)$. Effect of multiphysics coupling and comparison against numerical predictions from 3D FEM.

hygromagnetic coefficients, and assumes $\overline{\boldsymbol{\Gamma}}_{TC}^{(k)} = \overline{\boldsymbol{\Gamma}}_{Y}^{(k)} = \overline{\boldsymbol{\Gamma}}_{X}^{(k)} = \mathbf{0}$. On the other hand, in $\text{H - T - M - D}_{qzeyx}$ analysis, thermal and hygrometric fields are coupled with the Dufour and Soret effects, while pyromagnetic and hygromagnetic terms are neglected ($\overline{\boldsymbol{\Gamma}}_{w}^{(k)} = \overline{\boldsymbol{\Gamma}}_{f}^{(k)}$). Finally, $\text{H - T - M - D}_{qzewfyx}$ accounts for all the multifield coupling effects as introduced in Eq. (20). As can be seen from Fig. 2, for each case, a linear distribution is found for in-plane displacement field components, while U_3 exhibits non-uniform dispersions with slope variations. It is evident that classical theories like FSDT and TSDT could not have predicted these profiles with sufficient accuracy, as they account for uniform out-of-plane displacement field components. Furthermore, these theories are not suitable when zigzag effects occur. A zigzag profile is also observed for variations in magnetic potential and moisture concentration, whereas the through-the-thickness temperature distribution remains approximately linear. It should be noted that the zigzag profile is observed in the simulation when the multifield material properties are different from one layer to its adjacent one. Furthermore, the zigzag behavior is not automatically observed in all multifield quantities. For example, in the present simulation, the temperature and the moisture concentration variation are linearly distributed along the thickness in uncoupled simulations. However, in multifield coupled investigations the same curves may exhibit zigzag profiles, since the coupling coefficients are different from one layer to another. Note that the hygro-thermal coupling effect is more evident in the moisture profile, with only a slight change observed in the temperature distribution. In Fig. 3, which presents the 3D strain components, linear profiles are found for the in-plane components $\varepsilon_1, \varepsilon_2$ and γ_{12}, while ε_3 exhibits a stepwise linear distribution, due to the variation in mechanical stiffness across the lamination scheme. The influence of multifield coupling is particularly evident in terms of stretching in the first and second laminae, whereas the other layers experience minimal influence from these coupling terms in the constitutive relation. Finally, discontinuous parabolic distributions are observed for γ_{13} in all simulations, while γ_{23} is continuous but characterized by significant slope variations between adjacent layers. A similar trend is observed in Fig. 4, which shows the through-the-thickness distributions of 3D stress components. Due to the heterogeneity of the laminate, σ_1, σ_2 and τ_{12} exhibit discontinuous profiles across the thickness, whereas τ_{13} follows a parabolic distribution, with a pronounced slope variation between the second and the third laminae. Finally, σ_3, assumes a polynomial distribution that ensures that the loading conditions are satisfied at both the top and bottom surfaces. Similar profiles for the out-of-plane stress components τ_{13} and σ_3 are observed in all multifield simulations. The dispersion of τ_{23} shows some characteristics in each simulation, while consistently satisfying the external loading conditions. In the M−D analysis, both the higher-order theories and 3D FEM yield a parabolic profile. However, a significant zigzag behavior is observed in the T-D and H-D analyses. Furthermore, in all H-T-M−D simulations, the same curve is obtained since the multifield coupling terms have a minimal impact on the out-of-plane stress state of the solid. Conversely, the inclusion of various multifield terms in the simulation results in different profiles for the in-plane stress components σ_1, σ_2 and τ_{12}. In particular, the greatest sensitivity is observed when accounting for the hygro-thermal coupling with thermophoretic and thermal mass transfer effects. On the contrary, the hygro-thermo-electric coupling does not introduce additional stresses into the

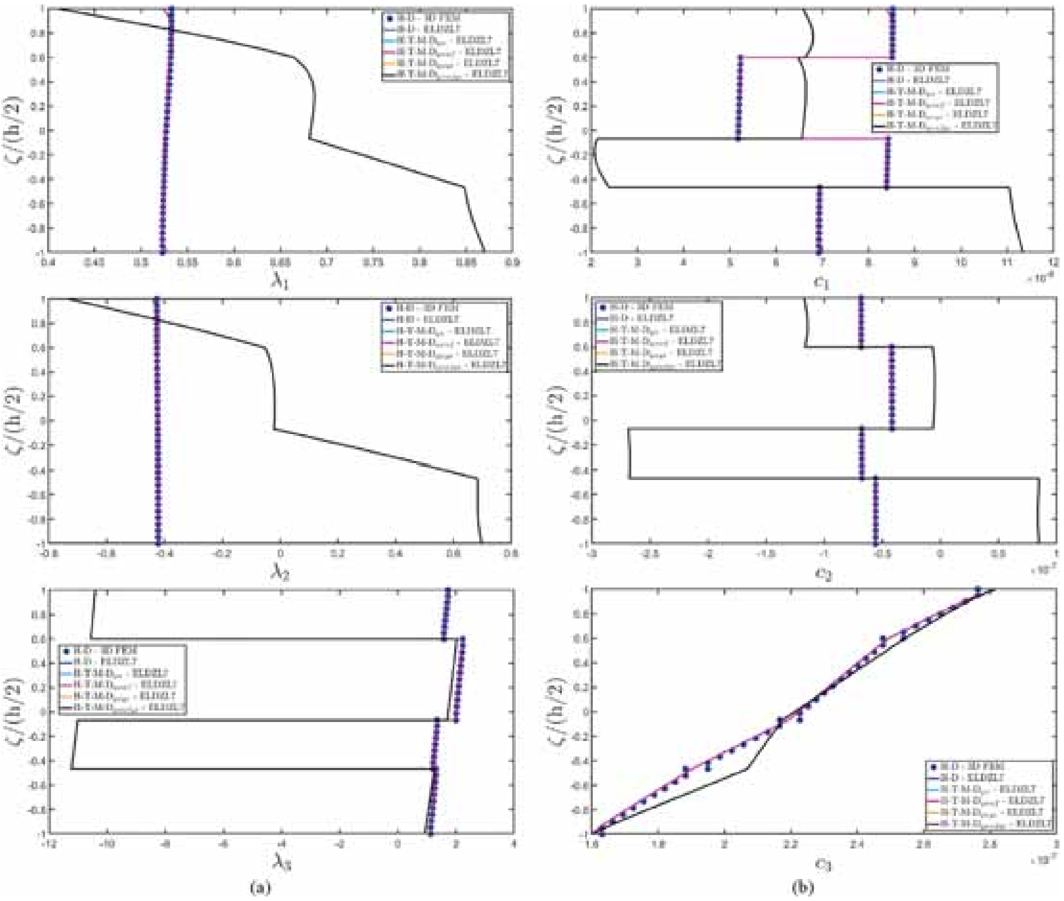

Fig. 7. Through-the-thickness distribution of hygrometric primary (a) and secondary (b) variables of a rectangular plate subjected to hygrometric, thermal, magnetic, and mechanical loading conditions with various surface distributions for the point located at $(s_1, s_2) = (0.25L_1, 0.25L_2)$. Effect of multiphysics coupling and comparison against numerical predictions from 3D FEM.

structure. The influence of these terms is more evident in the magnetic primary and secondary variables, as shown in Fig. 5. Here, the out-of-plane magnetic field component $\mathscr{H}_3$ exhibits a variation as the number of coupling terms increases, especially within the third lamina. In any case, a very good agreement is observed between the ELDZL7 theory and 3D FEM simulations in the M−D analysis. The magnetic flux components are also sensible to multifield coupling, especially $\mathscr{B}_3$. The greatest deviation from M−D results is observed in the $\mathrm{H-T-M-D}_{qzeyx}$ simulation. In fact, the introduction of magnetic, thermal, and hygrometric coupling in the $\mathrm{H-T-M-D}_{qzewfyx}$ analysis results in a reduced variation of the magnetic flux. Nevertheless, both primary and secondary magnetic variables can be accurately studied only by using a higher-order kinematic model and zigzag functions, due to the complexity of their through-the-thickness distributions, as observed in the 3D simulations. The thermal primary and secondary variables, namely the temperature gradient components and thermal flux components, are shown in Fig. 6. A parabolic distribution, without zigzag effects, is observed for θ_1 in the T-D analysis using both 3D FEM and the present formulation, while θ_2 is characterized by a linear dispersion. Finally, a discontinuous distribution is observed for θ_3. Similar results are obtained in the $\mathrm{H-T-M-D}_{qze}$ and $\mathrm{H-T-M-D}_{qzewf}$ simulations, indicating that the mechanical deformation does not affect the temperature gradient components profiles. However, a significative variation is observed in all temperature gradient components when the hygro-thermal coupling terms are considered in the analysis. As far as the thermal flux components is concerned, the in-plane components are discontinuous along the thickness direction, while the out-of-plane thermal flux h_3 is continuous. All h_3 curves converge at the bottom surface to the same value, thus balancing the external thermal loads. In contrast, the profiles diverge near the top surface, where a fixed temperature value is assigned. Furthermore, the zigzag effect is most evident in $\mathrm{H-T-M-D}_{qzewfyx}$ analysis, while a smoother profile is observed in the other simulations. The most significant effects of multifield coupling are shown in Fig. 7, which presents the primary and secondary hygrometric variables. More specifically, pyromagnetic and hygromagnetic coupling terms have minimal impact on both in-plane and out-of-plane primary variables, whereas the Dufour and Soret effects lead to substantial variations in the final distribution. This is particularly evident in c_1 and c_2 through-the-thickness dispersions. On the other hand, limited variations are observed in c_3, where the multifield analysis induces slight changes in the curve slope at each interface.

Next example primarily focuses on the coupling between thermal conduction and moisture diffusion. For this purpose, a cylindrical panel with radius $R = 2.5 \times 10^{-1}$ m and length $L_1 = 3 \times 10^{-2}$ m is considered. According to Eq. (1), the reference surface equation $\mathbf{r}(\alpha_1, \alpha_2)$ is expressed in the appropriate principal coordinates as follows:

$$\mathbf{r}(\alpha_1, \alpha_2) = \mathbf{r}(x, \vartheta) = R\cos\vartheta\mathbf{e}_1 - R\sin\vartheta\mathbf{e}_2 + x\mathbf{e}_3 \tag{112}$$

More specifically, the α_1 direction is designated as the longitudinal axis, while the circumferential direction aligns with α_2. The 2D parametric domain is defined as $[\alpha_1^0, \alpha_1^1] \times [\alpha_2^0, \alpha_2^1] = [0, L_1] \times [-\pi/2, \pi/6]$. The cylindrical panel under consideration consists in three layers with thicknesses $h_1 = h_3 = 5 \times 10^{-3}$ m and $h_2 = 1.5 \times 10^{-2}$ m, arranged according to the lamination scheme $(\mathrm{MAT-I}\backslash\mathrm{MAT-II}\backslash\mathrm{MAT-III})$. The material orientations for the various layers are $(0\backslash0\backslash0)$. The loading conditions include a mechanical surface pressure of magnitude $\overline{q}_3^{(+)} = -1\times10^5\ \mathrm{N/m^2}$ applied to the top surface, modelled as a patch load, as described in Eq. (109), by assuming $\alpha = 3$, centered as $(s_{10}, s_{20}) = (0.5L_1, 0.5L_2)$ and with shape parameters $c_{10} = 1/8L_1$ and $c_{20} = 1/8L_2$. In addition, the magnetic loading condition involves a sinusoidal distribution of magnetic potential at the top surface with magnitude $\Delta\overline{\Psi}_s^{(+)} = 1\,\mathrm{A}$, while a null magnetic potential variation is prescribed at the bottom surface, namely $\Delta\overline{\Psi}_s^{(-)} = 0\,\mathrm{A}$. A hybrid thermal loading condition is also applied. More specifically, a null temperature variation ($\Delta\overline{T}_s^{(+)} = 0\,\mathrm{K}$) is enforced at the top surface, whereas the bottom surface is subjected to a hydrostatic distribution of out-of-plane thermal flux, oriented along α_1, with a reference magnitude $\overline{q}_{\mathrm{T}}^{(-)} = 5\times10^2\ \mathrm{J/m^2}$. The corresponding distribution for $\alpha = \mathrm{T}$, is defined as $q_\alpha^{(\pm)}(s_1, s_2) = \overline{q}_\alpha^{(\pm)}(s_1/L_1)$. The corresponding semi-analytical coefficients for the trigonometric expansion are expressed as:

$$Q_{\alpha snm}^{(\pm)} = -\frac{4\overline{q}_\alpha^{(\pm)}}{\pi^2 nm}\cos(n\pi)(1-\cos(m\pi)) \tag{113}$$

Regarding the hygrometric loading condition, a hydrostatic distribution of moisture flux along α_1 with $\alpha = \mathrm{C}$, is applied at the top surface, and at the same time, a uniformly distributed mass flux is enforced at the bottom of the cylinder. The moisture flux magnitudes are $\overline{q}_{\mathrm{C}}^{(+)} = 2.8\times10^{-7}\ \mathrm{kg/m^2}$ and $\overline{q}_{\mathrm{C}}^{(-)} = 1.6\times10^{-7}\ \mathrm{kg/m^2}$, respectively. The results are computed using the ELDZL7 kinematic model and presented as thickness plots of mechanical, magnetic, thermal, and hygrometric variables, as well as primary and secondary variables. These results are shown in Figs. 8-13 for a point located at $(s_1, s_2) = (0.25L_1, 0.75L_2)$ within the physical domain. Semi-analytical solutions are derived by assuming $\widetilde{N} = \widetilde{M} = 150$. In addition, a 3D FEM model is developed using commercial software for M–D, T-D, and H-D analyses, where 3D structures have been discretized with parabolic brick elements for a total number of 410751 nodes. As illustrated in Fig. 8, the displacement field components, magnetic potential, temperature, and mass concentration variations for M–D, T-D, and H-D cases obtained with the proposed formulation align perfectly with the reference 3D FEM solution. For uncoupled H-T-M–D analysis, the elements of the hygro-thermal constitutive sub-matrices $\overline{\boldsymbol{\Gamma}}_{\mathrm{Y}}^{(k)}$ and $\overline{\boldsymbol{\Gamma}}_{\mathrm{X}}^{(k)}$ are set to zero, therefore the multiphysic coupling arises solely from piezomagnetic, pyromagnetic, and hygromagnetic effects. Thus, the displacement field components exhibit different profiles compared to preliminary investigations, while temperature and moisture concentration variations maintain similar distributions. On the contrary, the magnetic potential dispersion differs due to the additional strains induced by thermal and moisture loads. The inclusion of hygro-thermal coupling terms induces a minor variation in magnetic potential, while the temperature variation remains unaffected. On the other hand, a significative change is observed in the moisture concentration variation, particularly near the bottom surface, due to the non-zero temperature variation along the thickness direction. At the top surface, however, no variation is noticed in the profile since the temperature variation is assumed to be null in this region. For the 3D strain components reported in Fig. 9, a gradual deviation from the results of the uncoupled simulation is observed as the magnitude of the product $\lambda\nu$ increases. More specifically, in fully-coupled analyses, the magnitudes of the 3D strains increase, with a noticeable translation of the profile in ε_1,

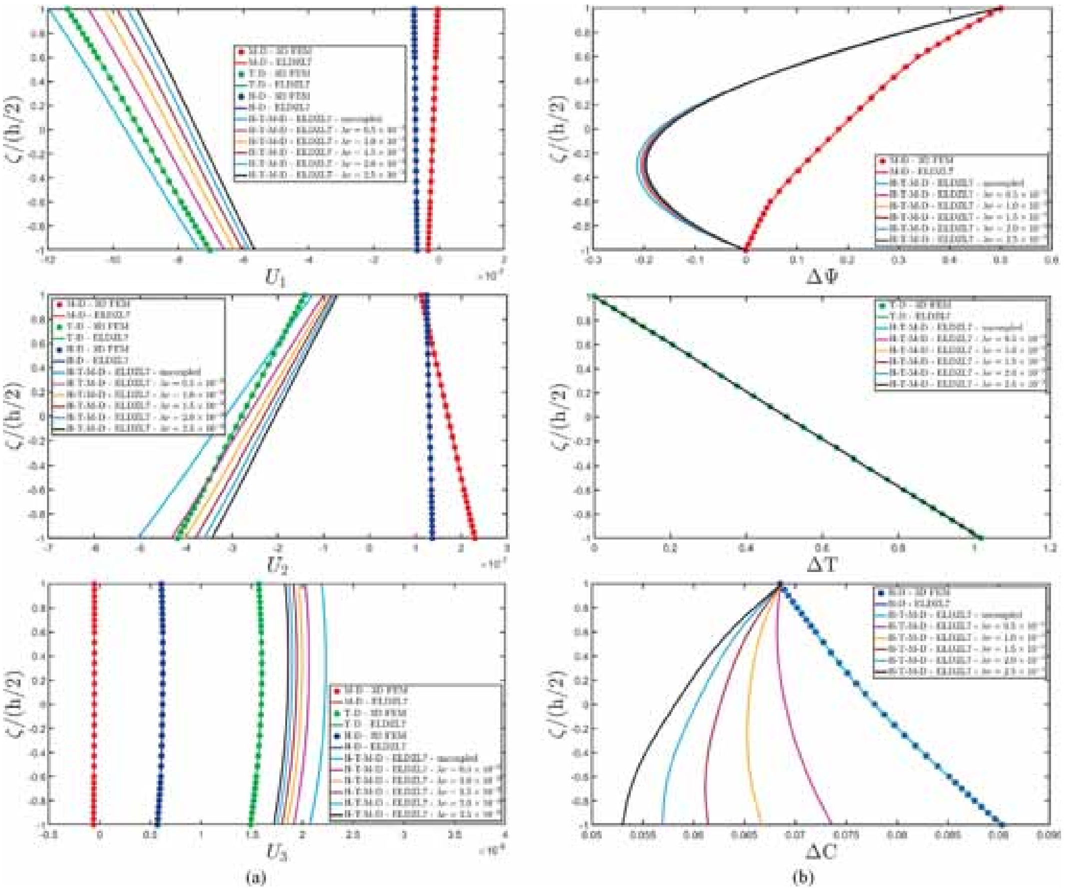

Fig. 8. Through-the-thickness distribution of displacement field components (a) and multifield configuration variables (b) of a circular cylinder subjected to hygrometric, thermal, magnetic, and mechanical loading conditions with various surface distributions for the point located at $(s_1, s_2) = (0.25L_1, 0.75L_2)$. Effect of multiphysics coupling and comparison against numerical predictions from 3D FEM.

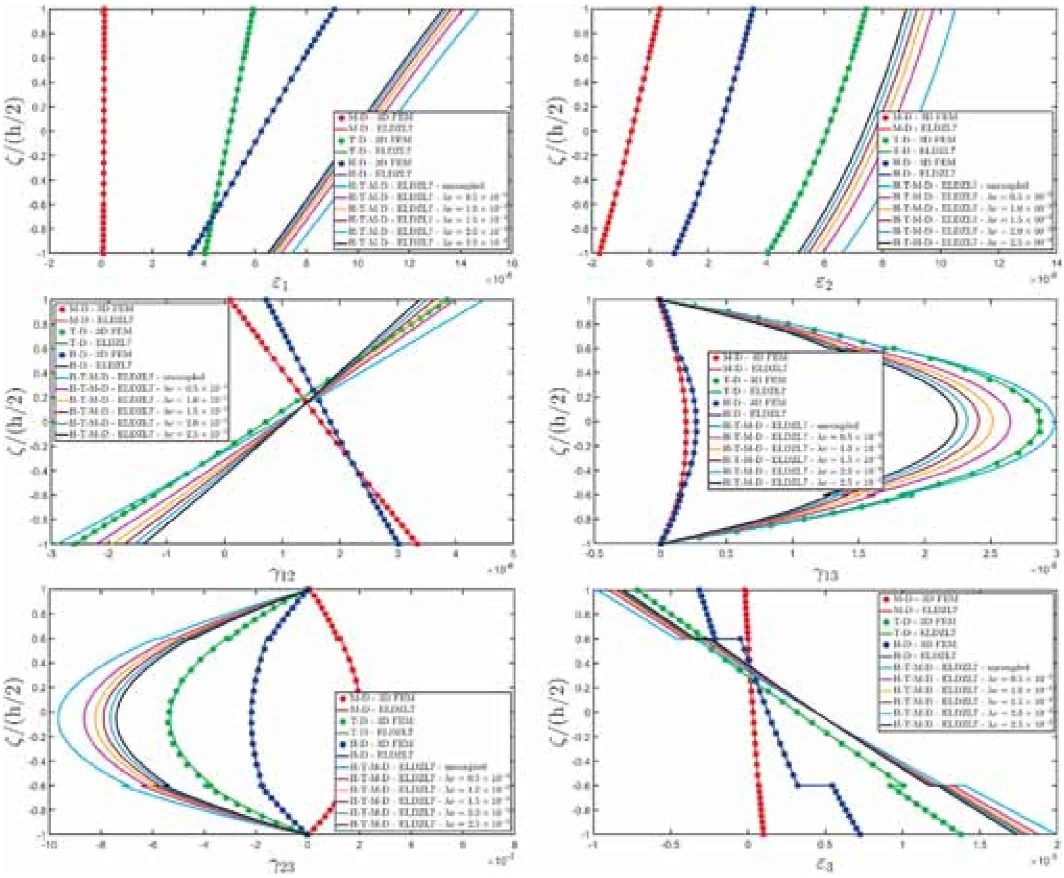

Fig. 9. Through-the-thickness distribution of 3D strain components of a circular cylinder subjected to hygrometric, thermal, magnetic, and mechanical loading conditions with various surface distributions for the point located at $(s_1, s_2) = (0.25L_1, 0.75L_2)$. Effect of multiphysics coupling and comparison against numerical predictions from 3D FEM.

ε_2. Variations are also evident in γ_{13} and γ_{23}, with the most pronounced changes occurring in the mid-thickness of the laminate. Finally, the ε_3 strain component shows a minimal sensitivity to coupling effects. Similar observations can be repeated for the 3D stress components illustrated in Fig. 10. Unlike the strain components, the stress distributions exhibit discontinuities, as the panel is made by three laminae. It should be noted that the out-of-plane normal stress σ_3 displays a smooth, continuous profile in M−D and T-D simulations, while the H-D analysis results are characterized by a pronounced zigzag effect. On the contrary, multifield analyses yield some smooth stress profiles. This aspect is important because it remarks the importance of using specific thickness functions in the kinematic model to arbitrarily select the multiphysic coupling without any loss of accuracy. In addition, the recovery procedure ensures the structural equilibrium under external mechanical pressures, in line with finite element predictions. After detailing the mechanical response of the cylindrical shell, a special attention is given to the magnetic primary and secondary variables, whose distributions in the thickness direction are shown in Fig. 11. In the M−D analysis, both 3D FEM and ELDZL7 simulations predict a zigzag effect for the in-plane magnetic field components, while multifield analyses yield smooth distributions. Regarding the out-of-plane component $\mathscr{H}_3$, the introduction of additional physical phenomena primarily increases its magnitude due to the piezomagnetic effect within the solid. Similar observations are made for the magnetic in-plane flux components $\mathscr{B}_1$ and $\mathscr{B}_2$. On the other hand, the profile of $\mathscr{B}_3$ rotates as the hygro-thermal coupling effect becomes higher. The thermal conduction primary and secondary variables are presented in Fig. 12. Here, the additional thermal effect due to moisture concentration is minimal, with results close to 3D FEM-based predictions for the T-D case. In particular, it is observed a linear distribution for θ_1, a parabolic profile for θ_2, and a discontinuous distribution along the laminate thickness for θ_3. In addition, h_3 follows a linear distribution. The influence of hygro-thermal coupling is evident in Fig. 13, which collects the components of the moisture concentration gradient vector and those of the moisture diffusion flux. Notable deviations are observed in λ_1 and c_1 distributions near the bottom surface, whereas λ_2 and c_2 remain unaffected by hygro-thermal coupling. These deviations near the top and bottom surfaces are observed because the structure is subjected to non-sinusoidal surface loads. For this reason, a Fourier trigonometric expansion of the solution is assumed, and the solution for $\widetilde{N} = \widetilde{M} = 150$ is not converged to stable results in those regions. The obtained profiles have been considered acceptable because the complete convergence of the solution would have requested additional computational effort with small sensitivity of the results. The out-of-plane flux component c_3 shows a small variation, while its corresponding gradient component, denoted by λ_3, is translated, since the mass diffusion driven by temperature gradients becomes significant. In addition, an increased value of the product $\lambda\nu$ leads to more pronounced variations and discontinuities in the curves at each interface.

The final example investigates the coupled multifield response of a shallow spherical panel subjected to mechanical, magnetic, thermal, and hygrometric loads. The geometry of the panel is described by Eq. (1), with the reference surface $\mathbf{r}(\alpha_1, \alpha_2)$ satisfying the geometric constraints of the Navier solution detailed in Eq. (66), where $R_1 = R_2 = R = 2.5 \times 10^{-1}$ m and $A_1 = A_2$. The 2D physical domain is defined as $\left[\alpha_1^0, \alpha_1^1\right] \times \left[\alpha_2^0, \alpha_2^1\right] = [7\pi/18, 11\pi/18] \times [-\pi/3, \pi/3]$. The panel consists of three layers with the same lamination scheme as in the previous example, namely (MAT - I\MAT - II\MAT - III), and layer thicknesses $h_1 = h_3 = 3 \times 10^{-3}$ m and $h_2 = 4 \times 10^{-3}$ m. The material orientation is set to

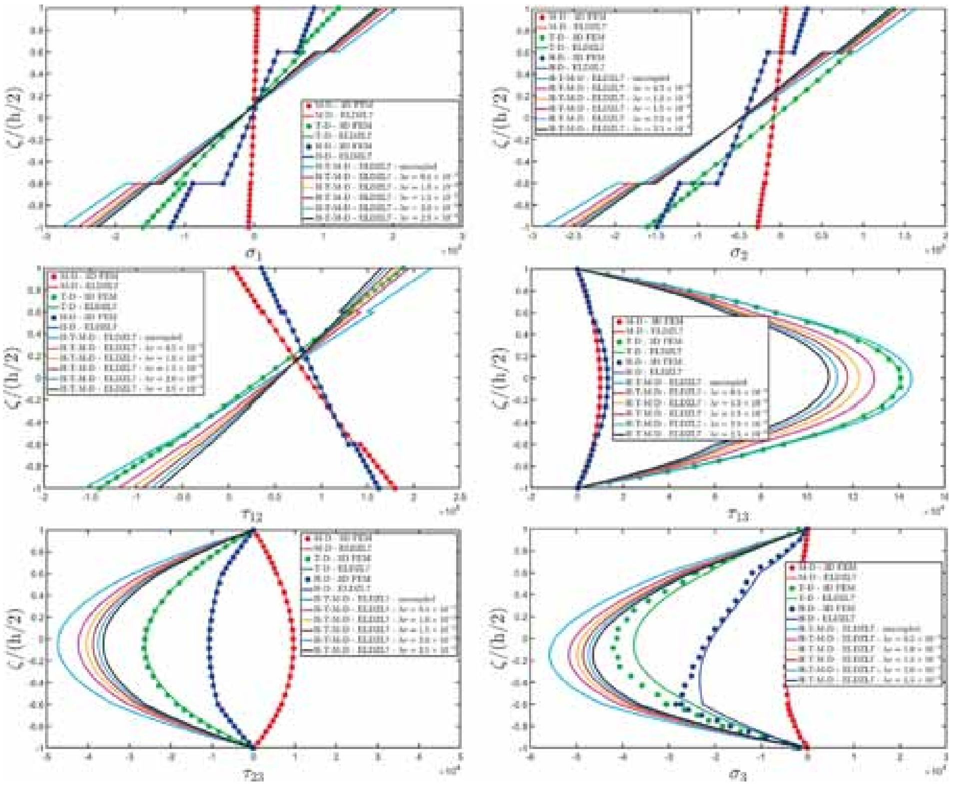

Fig. 10. Through-the-thickness distribution of 3D stress components of a circular cylinder subjected to hygrometric, thermal, magnetic, and mechanical loading conditions with various surface distributions for the point located at $(s_1, s_2) = (0.25L_1, 0.75L_2)$. Effect of multiphysics coupling and comparison against numerical predictions from 3D FEM.

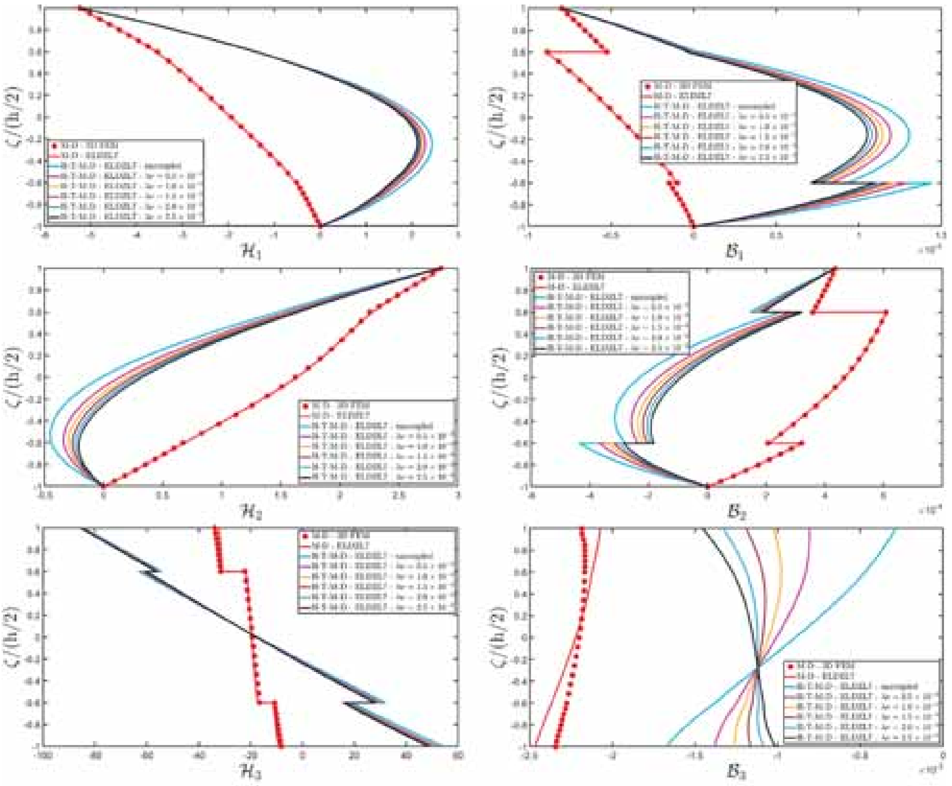

(a)   (b)

Fig. 11. Through-the-thickness distribution of magnetic primary (a) and secondary variables (b) of a circular cylinder subjected to hygrometric, thermal, magnetic, and mechanical loading conditions with various surface distributions for the point located at $(s_1, s_2) = (0.25L_1, 0.75L_2)$. Effect of multiphysics coupling and comparison against numerical predictions from 3D FEM.

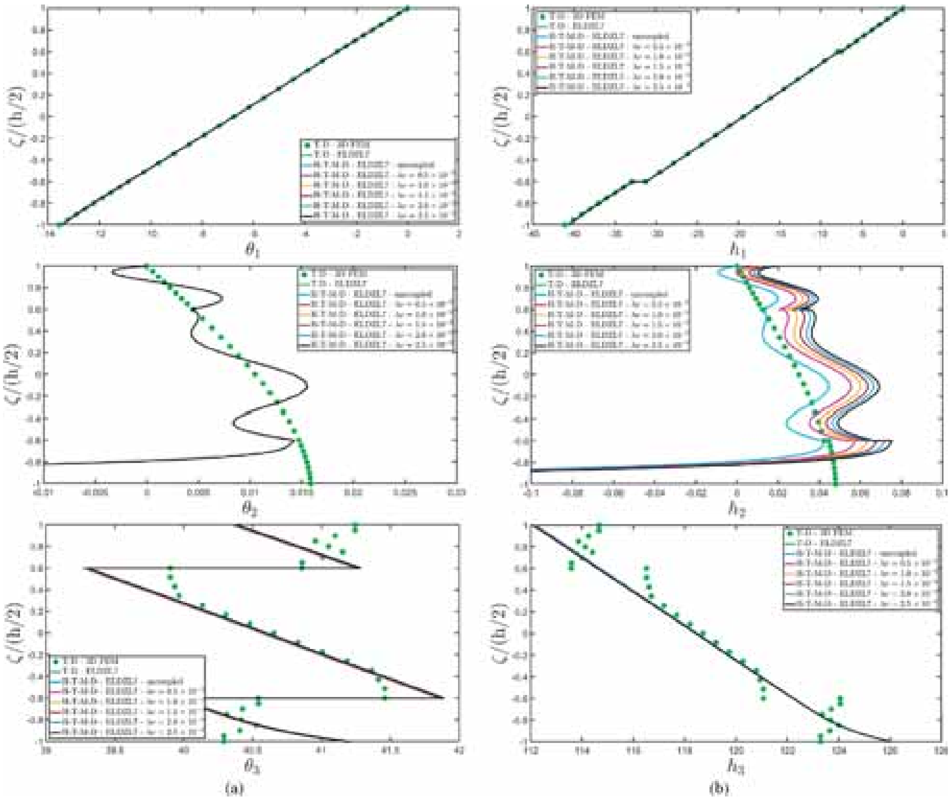

Fig. 12. Through-the-thickness distribution of thermal primary (a) and secondary variables (b) of a circular cylinder subjected to hygrometric, thermal, magnetic, and mechanical loading conditions with various surface distributions for the point located at $(s_1, s_2) = (0.25L_1, 0.75L_2)$. Effect of multiphysics coupling and comparison against numerical predictions from 3D FEM.

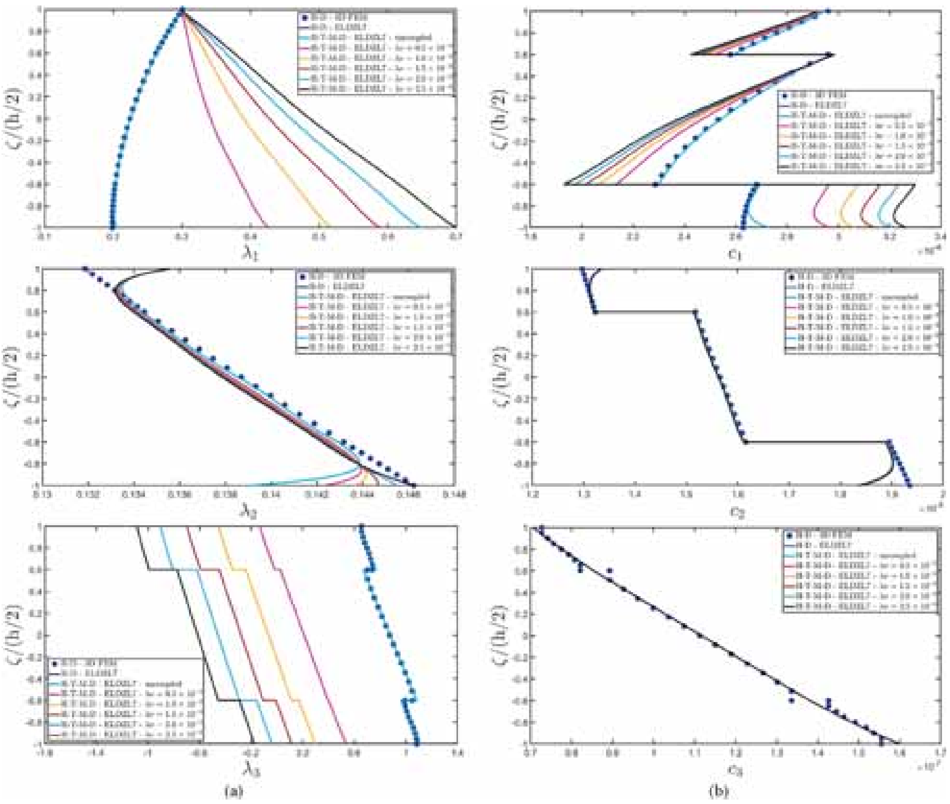

Fig. 13. Through-the-thickness distribution of hygrometric primary (a) and secondary variables (b) of a circular cylinder subjected to hygrometric, thermal, magnetic, and mechanical loading conditions with various surface distributions for the point located at $(s_1, s_2) = (0.25L_1, 0.75L_2)$. Effect of multiphysics coupling and comparison against numerical predictions from 3D FEM.

$(0\backslash 0\backslash 0)$. Three different loading conditions are considered, namely a uniform load, a patch load, and a ring load. In each case, multifield loads are applied, differing only in the surface distribution of the mechanical load. Magnetic kinematic constraints are enforced by applying a sinusoidal distribution of magnetic potential at the top surface, with magnitude $\Delta\overline{\Psi}_s^{(+)} = 1\,\mathrm{A}$ and wave number $\widetilde{N} = \widetilde{M} = 1$, while zero magnetic potential variation ($\Delta\overline{\Psi}_s^{(-)} = 0\,\mathrm{A}$) is assumed at the bottom surface. Uniform thermal flux is applied at $\zeta = -h/2$ with $\overline{q}_{\mathrm{T}}^{(-)} = 5 \times 10^2\,\mathrm{J/m^2}$, while uniform moisture flux is applied at both the top and bottom surfaces, with magnitudes $\overline{q}_{\mathrm{C}}^{(+)} = 2.8 \times 10^{-7}\,\mathrm{kg/m^2}$ and $\overline{q}_{\mathrm{C}}^{(-)} = 1.6 \times 10^{-7}\,\mathrm{kg/m^2}$, respectively. In addition, a null temperature variation distribution is ensured at the top surface by setting $\Delta\overline{\mathrm{T}}_s^{(+)} = 0\,\mathrm{K}$. As far as the mechanical surface load is concerned, uniform and ring distributions are characterized by the reference magnitude $\overline{q}_3^{(+)} = -1 \times 10^5\,\mathrm{N/m^2}$, while for a patch load, the value $\overline{q}_3^{(+)} = 1 \times 10^5\,\mathrm{N/m^2}$ is adopted. The governing parameters of this load shapes are $(s_{10}, s_{20}) = (0.5L_1, 0.5L_2)$ and $(c_{10}, c_{20}) = (3/8L_1, 1/8L_2)$. The panel lies on an elastic foundation which follows the Winkler-Pasternak model, setting $k_{3f}^{(-)} = 5 \times 10^9\,\mathrm{N/m^3}$ and $G_f^{(-)} = 5 \times 10^6\,\mathrm{N/m^2}$ the stiffnesses of the linear springs and of the shear layer, respectively. The ring load configuration is obtained from the superimposition of the uniform distribution and the patch load. Thickness plots from the simulations on this structure are evaluated at $(s_1, s_2) = (0.25L_1, 0.25L_2)$ within the physical domain, and the results are displayed in Figs. 14-19. The results derived with the ELW approach are evaluated by setting $\widetilde{N} = \widetilde{M} = 150$. Focusing on the hygro-thermo-magneto-mechanical configuration variables shown in Fig. 14, a linear distribution is observed for the in-plane displacement field components, while U_3 exhibits a parabolic profile in each simulation. As can be seen, in this example the zigzag effect is limited. The curves for the temperature variation and moisture concentration variation are smooth and continuous along the thickness direction, whereas the magnetic potential is discontinuous. In the case of mechanical ring load, the vertical deflection profile lies between those profiles associated with uniform and patch loads. It should be noted that a downward deflection occurs even under an upward surface traction due to strains induced by the multiphysic loading conditions. However, the remaining configuration variables exhibit the same distribution across all load cases. A similar behaviour is observed in Fig. 15, which presents the plots of 3D strain components. In particular, the model predicts that ε_1 and γ_{12} are linearly distributed along the thickness of the laminate, while ε_2 follows a parabolic profile. In contrast, ε_3 shows a stepwise distribution with approximately linear variations within each layer of the stacking sequence. Limited variations are observed for the out-of-plane distortions γ_{13} as the shape of the mechanical load changes, while a higher variability is observed for γ_{23}. As far as the 3D stress components shown in Fig. 16 is concerned, σ_1 and σ_2 are characterized by stepwise linear distributions, and τ_{12} displays a discontinuous variation. On the other hand, τ_{13} and σ_3 are linearly distributed in the first and third lamina, whereas the second layer contains the parabolic distributions of out-of-plane stresses. The variation in the stress state due to changes in load shape is particularly evident in τ_{23} within the second layer. The stress and strain variations caused by various surface pressures result in changes in the magnetic field distribution due to the piezomagnetic phenomenon. As shown in Fig. 17, each magnetic field component is affected by mechanical load variations, and a deviation of

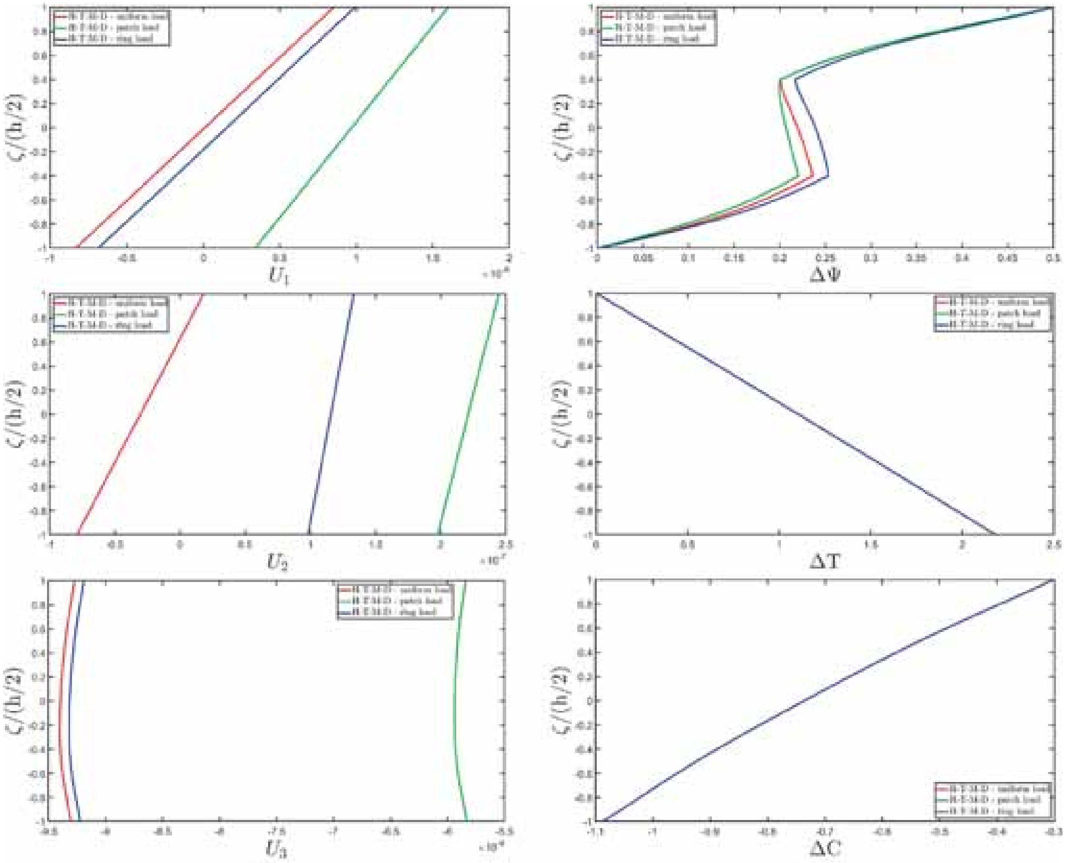

(a)

(b)

Fig. 14. Through-the-thickness distribution of displacement field components (a) and multifield configuration variables (b) of a spherical panel subjected to hygrometric, thermal, magnetic, and mechanical loading conditions with various surface distributions for the point located at $(s_1, s_2) = (0.25L_1, 0.25L_2)$. Effect of various load distributions.

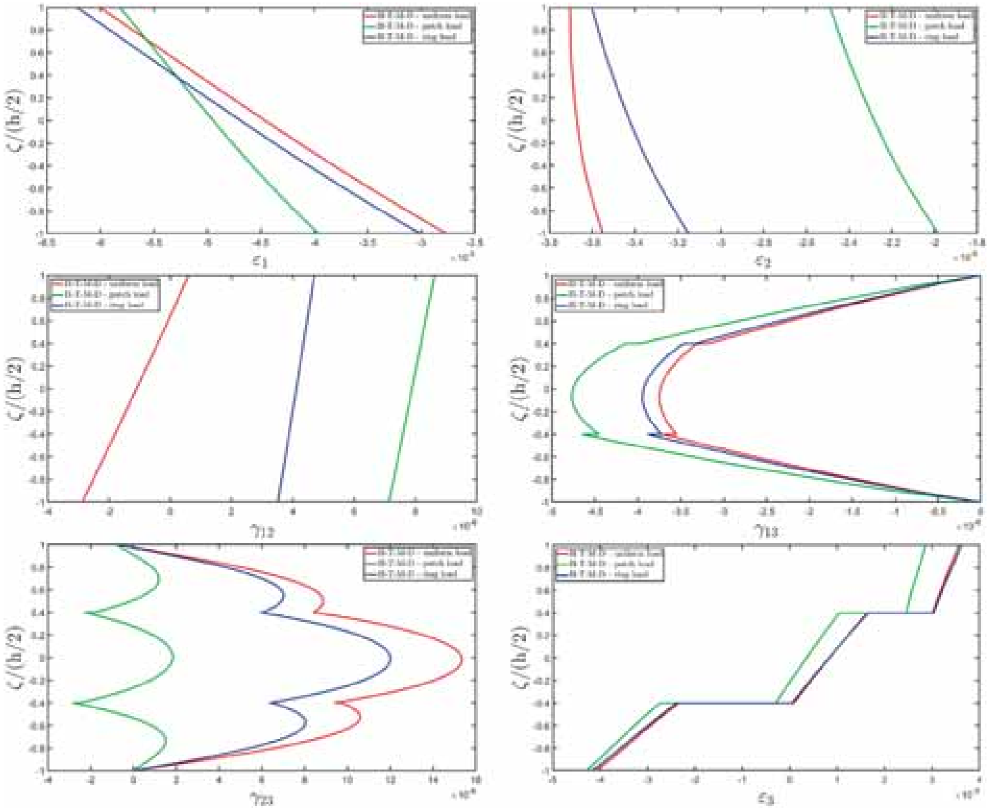

Fig. 15. Through-the-thickness distribution of 3D strain components of a spherical panel subjected to hygrometric, thermal, magnetic, and mechanical loading conditions with various surface distributions for the point located at $(s_1, s_2) = (0.25L_1, 0.25L_2)$. Effect of various load distributions.

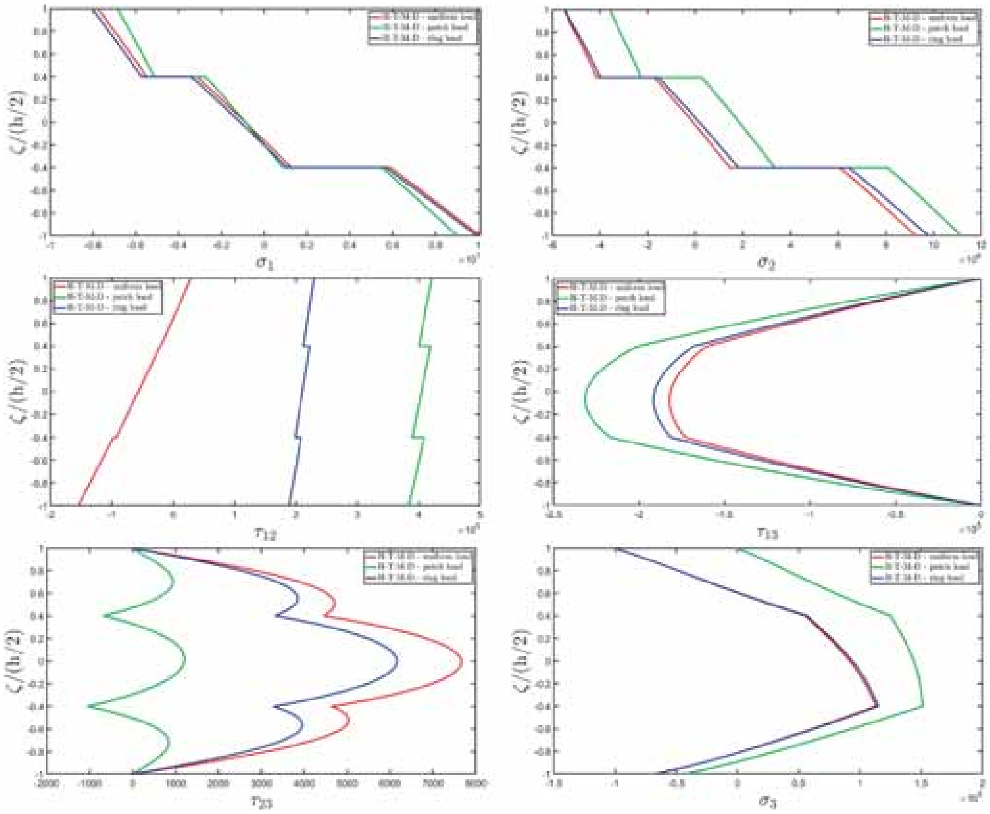

Fig. 16. Through-the-thickness distribution of 3D stress components of a spherical panel subjected to hygrometric, thermal, magnetic, and mechanical loading conditions with various surface distributions for the point located at $(s_1, s_2) = (0.25L_1, 0.25L_2)$. Effect of various load distributions.

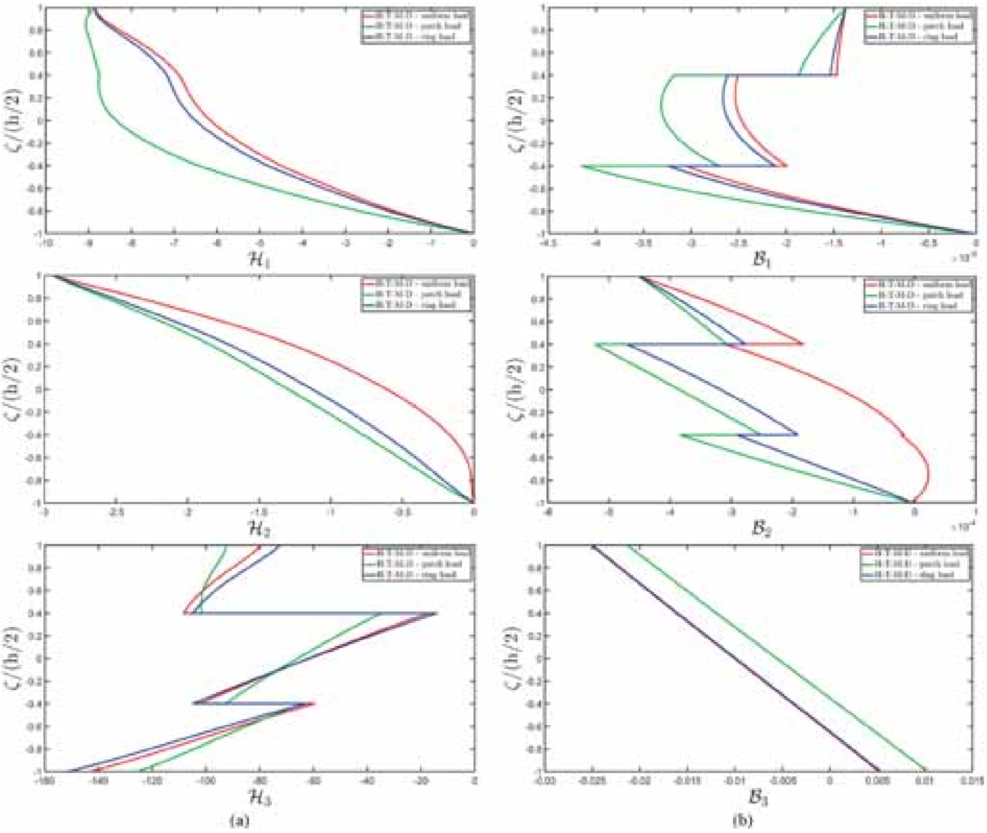

(a) (b)

Fig. 17. Through-the-thickness distribution of magnetic primary (a) and secondary variables (b) of a spherical panel subjected to hygrometric, thermal, magnetic, and mechanical loading conditions with various surface distributions for the point located at $(s_1, s_2) = (0.25L_1, 0.25L_2)$. Effect of various load distributions.

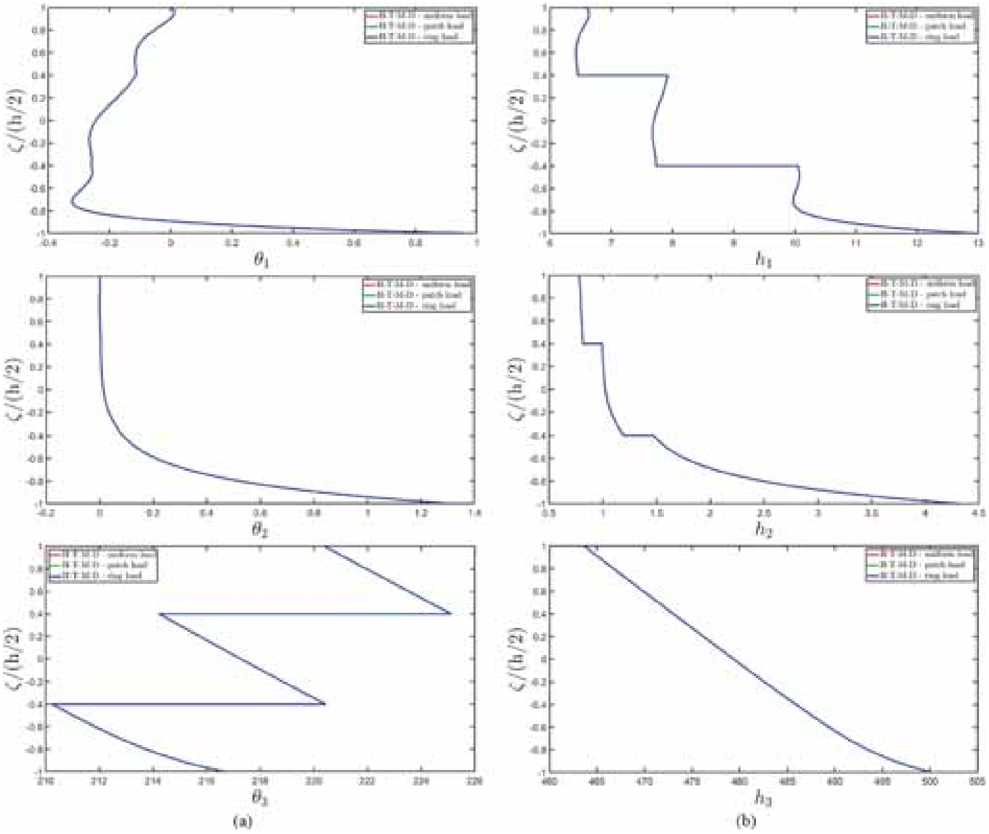

(a) (b)

Fig. 18. Through-the-thickness distribution of thermal primary (a) and secondary variables (b) of a spherical panel subjected to hygrometric, thermal, magnetic, and mechanical loading conditions with various surface distributions for the point located at $(s_1, s_2) = (0.25L_1, 0.25L_2)$. Effect of various load distributions.

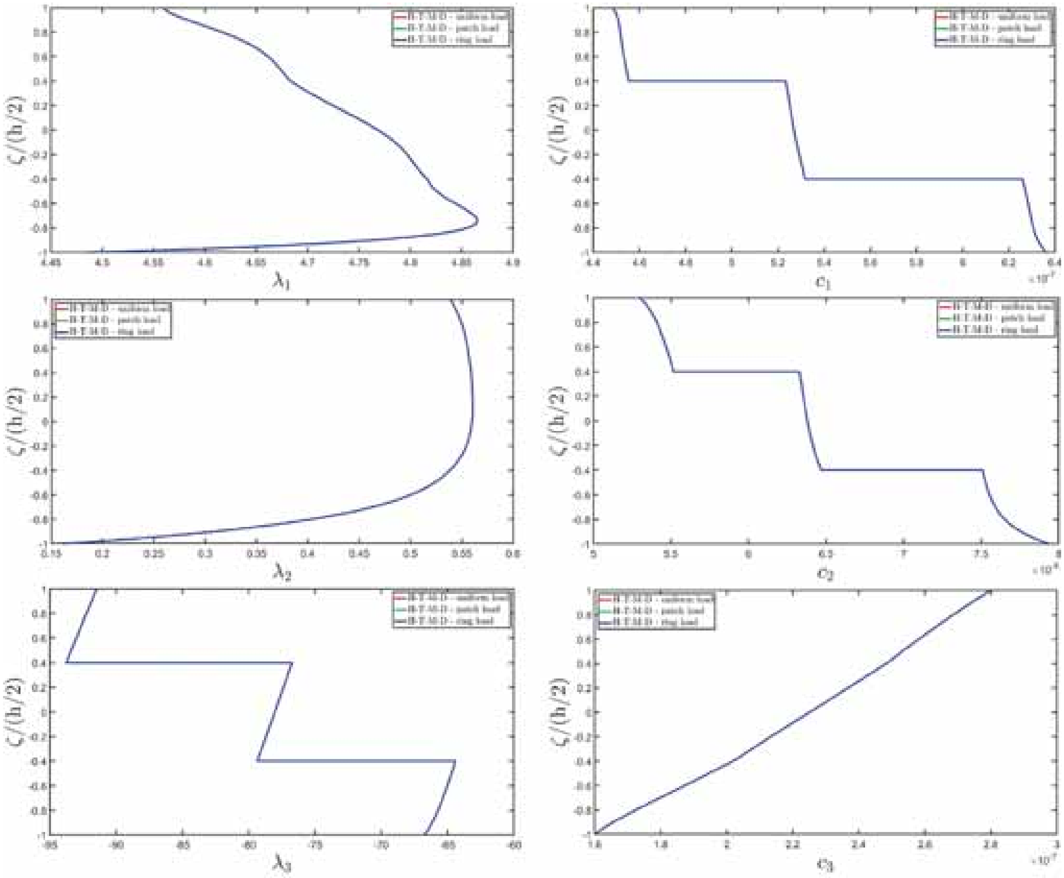

(a) (b)

Fig. 19. Through-the-thickness distribution of hygrometric primary (a) and secondary variables (b) of a spherical panel subjected to hygrometric, thermal, magnetic, and mechanical loading conditions with various surface distributions for the point located at $(s_1, s_2) = (0.25L_1, 0.25L_2)$. Effect of various load distributions.

curve is observed. Both $\mathscr{H}_1$ and $\mathscr{H}_2$ are continuously distributed along the thickness direction, while a discontinuous profile is observed for $\mathscr{H}_3$. In contrast, the magnetic flux component $\mathscr{B}_3$ is continuously distributed, while $\mathscr{B}_1$ and $\mathscr{B}_2$ are discontinuous. The highest variability in magnetic field and flux components is observed along the thickness direction, whereas a more limited variability is observed for magnitudes of in-plane components. As noted in the previous examples, the thermal and hygrometric primary and secondary variables are unaffected by variations in the mechanical pressure applied to the structure. In fact, for all load shape configurations, identical profiles are observed for temperature gradient components and thermal flux components, as depicted in Fig. 18. Similarly, no differences are observed in Fig. 19, which illustrates the thickness plots of hygrometric primary and secondary variables.

6. Conclusions

In this paper, a refined 2D formulation, based on unified formulation and higher-order theories, has been proposed for the multifield analysis of doubly-curved laminated panels under thermodynamic equilibrium conditions. The model considers mechanical, magnetic, thermal, and hygrometric effects, addressing coupling phenomena that are often neglected in classical commercial softwares. A generalized geometrical model, based on higher-order theories, has been employed, and the governing equations have been derived from the Master Balance principle considering the various coupling effects between the involved physical phenomena. The multifield material properties have been obtained through an analytical homogenization procedure based on Mori-Tanaka approach and Eshelby tensor evaluation for smart materials. By using the ELW approach, the model can consider the loading conditions in terms of both secondary variables and multifield kinematic constraints at the laminate's top and bottom surfaces. A semi-analytical Navier solution has been developed, and the 3D response of the solid has been reconstructed using an equilibrium-equation-based recovery procedure, which has adopted GDQ and GIQ numerical methods. The proposed model has demonstrated its utility in conducting multifield analyses with high accuracy, while significantly reducing the computational effort compared to established finite element simulations. Parametric investigations have been performed to explore various multifield coupling configurations, geometries, and load shapes, pointing out the efficiency of the model. Thus, the formulation can provide very accurate results in a simple and efficient way for advanced applications involving smart materials and laminated structures in multifield environments. Since the equations have been designed for arbitrary geometries and generally anisotropic materials, further enhancement of the research can be identified in the numerical implementation of the derived equations to obtain approximate solutions for more complex geometries, loading conditions, and lamination schemes.

CRediT authorship contribution statement

Francesco Tornabene: Writing – review & editing, Validation, Supervision, Software, Methodology, Investigation, Formal analysis, Data curation, Conceptualization. **Matteo Viscoti:** Writing – original draft, Validation, Investigation, Formal analysis, Data curation. **Rossana Dimitri:** Writing – review & editing, Validation, Methodology, Investigation, Formal analysis, Data curation.

Declaration of competing interest

The authors declare that they have no known competing financial interests or personal relationships that could have appeared to influence the work reported in this paper.

Appendix 1

In this appendix, a smart material with hygrometric, thermal, magnetic and mechanical properties is homogenized with proper analytical expression, following the 3D constitutive relationship of Eq. (23). These expressions are derived from the Mori-Tanaka procedure, which accounts for the evaluation of the Eshelby tensor, as detailed in Ref. [49]. The input parameters for deriving equivalent multifield properties are the constitutive coefficients of the base materials occurring in the unit cell, as well as the volume fractions V_f and V_m of cylindrical fibers oriented along ζ and of an isotropic medium, respectively. These quantities satisfy the relation $V_m + V_f = 1$ because it is assumed that no voids are present within the solid. The homogenization accounts for the full coupling between mechanical elasticity, electrostatics, magnetostatics, heat transfer, and moisture diffusion. More specifically, the homogenized smart material is characterized by the following constitutive relationship, written in the material reference system:

$$
\left[\begin{array}{c}
\hat{\sigma}_1\\ \hat{\sigma}_2\\ \hat{\tau}_{12}\\ \hat{\tau}_{13}\\ \hat{\tau}_{23}\\ \hat{\sigma}_3\\ \hline
\hat{\mathcal{D}}_1\\ \hat{\mathcal{D}}_2\\ \hat{\mathcal{D}}_3\\ \hline
\hat{\mathcal{B}}_1\\ \hat{\mathcal{B}}_2\\ \hat{\mathcal{B}}_3\\ \hline
\eta\\ \hline
\mu\\ \hline
\hat{h}_1\\ \hat{h}_2\\ \hat{h}_3\\ \hline
\hat{c}_1\\ \hat{c}_2\\ \hat{c}_3
\end{array}\right]
=
\left[\begin{array}{cccccc|ccc|ccc|c|c|ccc|ccc}
C_{11} & C_{12} & 0 & 0 & 0 & C_{13} & 0 & 0 & -p_{31} & 0 & 0 & -q_{31} & -z_{11} & -e_{11} & 0 & 0 & 0 & 0 & 0 & 0\\
C_{12} & C_{22} & 0 & 0 & 0 & C_{23} & 0 & 0 & -p_{32} & 0 & 0 & -q_{32} & -z_{22} & -e_{22} & 0 & 0 & 0 & 0 & 0 & 0\\
0 & 0 & C_{66} & 0 & 0 & 0 & 0 & 0 & 0 & 0 & 0 & 0 & 0 & 0 & 0 & 0 & 0 & 0 & 0 & 0\\
0 & 0 & 0 & C_{44} & 0 & 0 & -p_{14} & 0 & 0 & -q_{14} & 0 & 0 & 0 & 0 & 0 & 0 & 0 & 0 & 0 & 0\\
0 & 0 & 0 & 0 & C_{55} & 0 & 0 & -p_{25} & 0 & 0 & -q_{25} & 0 & 0 & 0 & 0 & 0 & 0 & 0 & 0 & 0\\
C_{13} & C_{23} & 0 & 0 & 0 & C_{33} & 0 & 0 & -p_{33} & 0 & 0 & -q_{33} & -z_{33} & -e_{33} & 0 & 0 & 0 & 0 & 0 & 0\\ \hline
0 & 0 & 0 & p_{14} & 0 & 0 & l_{11} & 0 & 0 & d_{11} & 0 & 0 & 0 & 0 & 0 & 0 & 0 & 0 & 0 & 0\\
0 & 0 & 0 & 0 & p_{25} & 0 & 0 & l_{22} & 0 & 0 & d_{22} & 0 & 0 & 0 & 0 & 0 & 0 & 0 & 0 & 0\\
p_{31} & p_{32} & 0 & 0 & 0 & p_{33} & 0 & 0 & l_{33} & 0 & 0 & d_{33} & o_{33} & g_{33} & 0 & 0 & 0 & 0 & 0 & 0\\ \hline
0 & 0 & 0 & q_{14} & 0 & 0 & d_{11} & 0 & 0 & m_{11} & 0 & 0 & 0 & 0 & 0 & 0 & 0 & 0 & 0 & 0\\
0 & 0 & 0 & 0 & q_{25} & 0 & 0 & d_{22} & 0 & 0 & m_{22} & 0 & 0 & 0 & 0 & 0 & 0 & 0 & 0 & 0\\
q_{31} & q_{32} & 0 & 0 & 0 & q_{33} & 0 & 0 & d_{33} & 0 & 0 & m_{33} & w_{33} & f_{33} & 0 & 0 & 0 & 0 & 0 & 0\\ \hline
z_{11} & z_{22} & 0 & 0 & 0 & z_{33} & 0 & 0 & o_{33} & 0 & 0 & w_{33} & \xi_{11} & \xi_{12} & 0 & 0 & 0 & 0 & 0 & 0\\ \hline
e_{11} & e_{22} & 0 & 0 & 0 & e_{33} & 0 & 0 & g_{33} & 0 & 0 & f_{33} & \xi_{12} & \xi_{22} & 0 & 0 & 0 & 0 & 0 & 0\\ \hline
0 & 0 & 0 & 0 & 0 & 0 & 0 & 0 & 0 & 0 & 0 & 0 & 0 & 0 & k_{11} & 0 & 0 & y_{11} & 0 & 0\\
0 & 0 & 0 & 0 & 0 & 0 & 0 & 0 & 0 & 0 & 0 & 0 & 0 & 0 & 0 & k_{22} & 0 & 0 & y_{22} & 0\\
0 & 0 & 0 & 0 & 0 & 0 & 0 & 0 & 0 & 0 & 0 & 0 & 0 & 0 & 0 & 0 & k_{33} & 0 & 0 & y_{33}\\ \hline
0 & 0 & 0 & 0 & 0 & 0 & 0 & 0 & 0 & 0 & 0 & 0 & 0 & 0 & x_{11} & 0 & 0 & s_{11} & 0 & 0\\
0 & 0 & 0 & 0 & 0 & 0 & 0 & 0 & 0 & 0 & 0 & 0 & 0 & 0 & 0 & x_{22} & 0 & 0 & s_{22} & 0\\
0 & 0 & 0 & 0 & 0 & 0 & 0 & 0 & 0 & 0 & 0 & 0 & 0 & 0 & 0 & 0 & x_{33} & 0 & 0 & s_{33}
\end{array}\right]
\left[\begin{array}{c}
\hat{\varepsilon}_1\\ \hat{\varepsilon}_2\\ \hat{\gamma}_{12}\\ \hat{\gamma}_{13}\\ \hat{\gamma}_{23}\\ \hat{\varepsilon}_3\\ \hline
\hat{\mathcal{E}}_1\\ \hat{\mathcal{E}}_2\\ \hat{\mathcal{E}}_3\\ \hline
\hat{\mathcal{H}}_1\\ \hat{\mathcal{H}}_2\\ \hat{\mathcal{H}}_3\\ \hline
\widehat{\Delta \mathrm{T}}\\ \hline
\widehat{\Delta \mathrm{C}}\\ \hline
\hat{\theta}_1\\ \hat{\theta}_2\\ \hat{\theta}_3\\ \hline
\hat{\lambda}_1\\ \hat{\lambda}_2\\ \hat{\lambda}_3
\end{array}\right]
\tag{A1}
$$

Here, $\widehat{\sigma}_1, \widehat{\sigma}_2, \widehat{\sigma}_3, \widehat{\tau}_{12}, \widehat{\tau}_{13}, \widehat{\tau}_{23}$ and $\widehat{\varepsilon}_1, \widehat{\varepsilon}_2, \widehat{\varepsilon}_3, \widehat{\gamma}_{12}, \widehat{\gamma}_{13}, \widehat{\gamma}_{23}$ are the 3D stress and strain components, while $\widehat{\mathscr{E}}_1, \widehat{\mathscr{E}}_2, \widehat{\mathscr{E}}_3$ and $\widehat{\mathscr{D}}_1, \widehat{\mathscr{D}}_2, \widehat{\mathscr{D}}_3$ are the electric field components and the electric flux components, respectively. Furthermore, $\widehat{\theta}_1, \widehat{\theta}_2, \widehat{\theta}_3$ and $\widehat{h}_1, \widehat{h}_2, \widehat{h}_3$ are the primary and secondary variables associated with the heat transfer problem. Finally, $\widehat{\lambda}_1, \widehat{\lambda}_2, \widehat{\lambda}_3$ and $\widehat{c}_1, \widehat{c}_2, \widehat{c}_3$ are the moisture concentration gradient components and the moisture concentration flux components within the solid. In what follows, the constitutive constants related to fibers are denoted with the subscript "*f*", while the quantities associated with the isotropic matrix are denoted by "*m*".

Preliminary computations

$$
j = 2V_f \frac{C_{44m} l_{11m} m_{11m} + p_{14m}^2 m_{11m} + l_{11m} q_{14m}^2 - 2d_{11m} p_{14m} - d_{11m}^2 C_{44m}}{(ic - gb)h + (fb - ia)e + (ga - fc)d}
$$

$$
a = V_m \Big(\big(q_{14f} - q_{14m} \big) \big(l_{11m} m_{11m} - d_{11m}^2 \big) - \big(d_{11f} - d_{11m} \big) \big(p_{14m} m_{11m} - d_{11m} q_{14m} \big) - \big(m_{11f} - m_{11m} \big) \big(q_{14m} l_{11m} - d_{11m} p_{14m} \big) \Big)
$$

$$
b = V_m \Big(\big(p_{14f} - p_{14m} \big) \big(l_{11m} m_{11m} - d_{11m}^2 \big) - \big(d_{11f} - d_{11m} \big) \big(q_{14m} l_{11m} - d_{11m} p_{14m} \big) - \big(l_{11f} - l_{11m} \big) \big(p_{14m} m_{11m} - d_{11m} q_{14m} \big) \Big)
$$

$$
\begin{aligned}
c = V_m \Big(& \big(C_{44f} - C_{44m} \big) \big(l_{11m} m_{11m} - d_{11m}^2 \big) + \big(p_{14f} - p_{14m} \big) \big(p_{14m} m_{11m} - d_{11m} q_{14m} \big) + \big(q_{14f} - q_{14m} \big) \big(q_{14m} l_{11m} - d_{11m} p_{14m} \big) \Big) + \\
& + \frac{j}{V_f} \big((ic - gb)h + (fb - ia)e + (ga - fc)d \big)
\end{aligned}
$$

$$\begin{gathered}
d = V_m\Big(-\left(d_{11f}-d_{11m}\right)\left(d_{11m}C_{44m}+p_{14m}q_{14m}\right)+\Big(p_{14f}-p_{14m}\Big)\left(p_{14m}m_{11m}-d_{11m}q_{14m}\right)+\left(l_{11f}-l_{11m}\right)\left(q_{14m}^2+C_{44m}m_{11m}\right)\Big)+\\
+\frac{j}{V_f}\left(\left(ic-gb\right)h+\left(fb-ia\right)e+\left(ga-fc\right)d\right)\\
e = V_m\Big(\Big(q_{14f}-q_{14m}\Big)\left(d_{11m}C_{44m}+p_{14m}q_{14m}\right)+\left(C_{44f}-C_{44m}\right)\left(p_{14m}m_{11m}-d_{11m}q_{14m}\right)-\Big(p_{14f}-p_{14m}\Big)\left(q_{14m}^2+C_{44m}m_{11m}\right)\Big)\\
f = V_m\Big(-\left(d_{11f}-d_{11m}\right)\left(d_{11m}C_{44m}+p_{14m}q_{14m}\right)+\Big(q_{14f}-q_{14m}\Big)\left(q_{14m}l_{11m}-d_{11m}p_{14m}\right)+\left(m_{11f}-m_{11m}\right)\left(p_{14m}^2+C_{44m}l_{11m}\right)\Big)+\\
+\frac{j}{V_f}\left(\left(ic-gb\right)h+\left(fb-ia\right)e+\left(ga-fc\right)d\right)\\
g = V_m\Big(\Big(p_{14f}-p_{14m}\Big)\left(d_{11m}C_{44m}+p_{14m}q_{14m}\right)+\left(C_{44f}-C_{44m}\right)\left(q_{14m}l_{11m}-d_{11m}p_{14m}\right)-\Big(q_{14f}-q_{14m}\Big)\left(p_{14m}^2+C_{44m}l_{11m}\right)\Big)\\
h = V_m\Big(-\left(m_{11f}-m_{11m}\right)\left(d_{11m}C_{44m}-p_{14m}q_{14m}\right)+\Big(q_{14f}-q_{14m}\Big)\left(p_{14m}m_{11m}-d_{11m}q_{14m}\right)+\left(d_{11f}-d_{11m}\right)\left(q_{14m}^2+C_{44m}m_{11m}\right)\Big)\\
i = V_m\Big(-\left(l_{11f}-l_{11m}\right)\left(d_{11m}C_{44m}+p_{14m}q_{14m}\right)+\Big(p_{14f}-p_{14m}\Big)\left(q_{14m}l_{11m}-d_{11m}p_{14m}\right)+\left(d_{11f}-d_{11m}\right)\left(p_{14m}^2+C_{44m}l_{11m}\right)\Big)
\end{gathered} \tag{A2}$$

Density

$$\rho = V_m\rho_m + V_f\rho_f \tag{A3}$$

Elastic stiffness coefficients

$$\begin{gathered}
k = \frac{k_m k_f + V_f m_m k_f + V_m m_m k_m}{V_m k_f + V_f k_m + m_m}\\
m = \frac{m_m\left(k_m m_f + V_f k_m m_f + V_m k_m m_m + 2m_m m_f\right)}{V_m k_m m_f + k_m m_m + V_f k_m m_m + 2V_m m_m m_f + 2V_f m_m^2}\\
C_{11} = C_{22} = k + m\\
C_{12} = k - m\\
C_{13} = C_{23} = C_{13m} + \frac{V_f\left(C_{13f}-C_{13m}\right)\left(k_m+m_m\right)}{V_m k_f + V_f k_m + m_m}\\
C_{33} = C_{33m} + V_f\left(C_{33f} - C_{33m} - \frac{V_m\left(C_{13m}-C_{13f}\right)^2}{V_m k_f + V_f k_m + m_m}\right)\\
C_{44} = C_{55} = C_{44m} + j\Big(\Big(p_{14f}-p_{14m}\Big)\left(fe-gh\right)+\left(C_{44f}-C_{44m}\right)\left(ih-fd\right)+\Big(q_{14f}-q_{14m}\Big)\left(gd-ie\right)\Big)
\end{gathered} \tag{A4}$$

Piezomagnetic coefficients

$$\begin{gathered}
q_{31} = q_{32} = q_{31m} + \frac{V_f\Big(q_{31f}-q_{31m}\Big)\left(k_m+m_m\right)}{V_m k_f + V_f k_m + m_m}\\
q_{33} = q_{33m} + V_f\left(q_{33f} - q_{33m} + \frac{V_m\left(C_{13m}-C_{13f}\right)\Big(q_{31f}-q_{31m}\Big)}{V_m k_f + V_f k_m + m_m}\right)\\
q_{14} = q_{25} = q_{14m} + j\Big(\Big(p_{14f}-p_{14m}\Big)\left(ch-ae\right)+\left(C_{44f}-C_{44m}\right)\left(ad-bh\right)+\Big(q_{14f}-q_{14m}\Big)\left(be-cd\right)\Big)
\end{gathered} \tag{A5}$$

Magnetic permeability coefficients

$$\begin{gathered}
m_{11} = m_{22} = m_{11m} + j\Big(\left(d_{11f}-d_{11m}\right)\left(ch-ae\right)+\Big(q_{14f}-q_{14m}\Big)\left(bh-ad\right)+\left(m_{11f}-m_{11m}\right)\left(be-cd\right)\Big)\\
m_{33} = m_{33m} + V_f\left(m_{33f} - m_{33m} + \frac{V_m\left(m_{31f}-m_{31m}\right)^2}{V_m k_f + V_f k_m + m_m}\right)
\end{gathered} \tag{A6}$$

Thermal expansion coefficients

$$a_{11} = \frac{V_f E_f a_f + V_m E_m a_m}{E_1}$$

$$a_{22} = a_{33} = \left(1+\nu_f\right)a_f V_f + (1+\nu_m)a_m V_m - \nu_{12}a_{11} \tag{A7}$$

Hygroscopic expansion coefficients

$$b_{11} = \frac{V_f E_f b_f + V_m E_m b_m}{E_1}$$

$$b_{22} = b_{33} = \left(1+\nu_f\right)b_f V_f + (1+\nu_m)b_m V_m - \nu_{12}b_{11} \tag{A8}$$

Pyromagnetic coefficient

$$w_{33} = V_m w_{33m} + V_f w_{33f} - V_m V_f \frac{\left(q_{31f}-q_{31m}\right)\left(z_{11f}-z_{11m}\right)}{C_{11m} + V_m k_f - V_m k_m} \tag{A9}$$

Hygromagnetic coefficient

$$f_{33} = V_m f_{33m} + V_f f_{33f} - V_m V_f \frac{\left(q_{31f}-q_{31m}\right)\left(e_{11f}-e_{11m}\right)}{C_{11m} + V_m k_f - V_m k_m} \tag{A10}$$

Specific heat capacity.

$$c_p = \frac{V_f \rho_f c_{pf} + V_m \rho_m c_{pm}}{\rho} \tag{A11}$$

Equilibrium moisture content.

$$M_\infty = \frac{V_m \rho_m M_{\infty m} + V_f \rho_f M_{\infty f}}{\rho} \tag{A12}$$

Thermal conductivity

$$k_{11} = k_{22} = \frac{k_m k_f}{V_f k_m + V_m k_f}$$

$$k_{33} = V_m k_m + V_f k_f = \left(1-V_f\right)k_m + V_f k_f = \left(k_f - k_m\right)V_f + k_m \tag{A13}$$

Diffusion coefficients

$$s_{11} = s_{22} = \frac{s_m s_f}{V_f s_m + V_m s_f}$$

$$s_{33} = V_m s_m + V_f s_f = \left(1-V_f\right)s_m + V_f s_f = \left(s_f - s_m\right)V_f + s_m \tag{A14}$$

Thermodiffusion (Dufour) coefficients

$$y_{11} = \nu\rho c s_{11} = \nu u_d k_{11}, \quad y_{22} = \nu\rho c s_{22} = \nu u_d k_{22}, \quad y_{33} = \nu\rho c s_{33} = \nu u_d k_{33} \tag{A15}$$

Thermophoretic (Soret) coefficients

$$x_{11} = \frac{\lambda}{\rho c}k_{11}, \quad x_{22} = \frac{\lambda}{\rho c}k_{22}, \quad x_{33} = \frac{\lambda}{\rho c}k_{33} \tag{A16}$$

Data availability

No data was used for the research described in the article.

References

[1] Noor AK, Burton WS. Computational models for high-temperature multilayered composite plates and shells. Appl Mech Rev 1992;45:419–46.

[2] Ahmad SN, Prakash O. A review on modelling, experimental analysis and parametric effects of earth–air heat exchanger. Model Earth Syst Environ 2022;8:1535–51.

[3] Nguyen NTT, Nguyen TTT, Nguyen DTC, Van Tran T. Functionalization strategies of metal-organic frameworks for biomedical applications and treatment of emerging pollutants: a review. Sci Total Environ 2024;906:167295.

[4] Lin K, Wang Z. Multiscale mechanics and molecular dynamics simulations of the durability of fiber-reinforced polymer composites. Commun Mater 2023;4:66.

[5] Klemczak B, Smolana A, Jędrzejewska A. Modeling of heat and mass transfer in cement-based materials during cement hydration—a review. Energies 2024;17:2513.

[6] Zhao X, et al. Recycling of natural fiber composites: challenges and opportunities. Resour Conserv Recycl 2022;177:105962.

[7] Sih GC, Ogawa A. Transient thermal change on a solid surface: coupled diffusion of heat and moisture. J Therm Stresses 1982;5:265–82.

[8] Sih GC, Shih MT, Chou SC. Transient hygrothermal stresses in composites: coupling of moisture and heat with temperature varying diffusivity. Int J Eng Sci 1980;18:19–42.
[9] Sih GC, Michopoulos J, Chou SC. Hygrothermoelasticity. Dordrecht: Martinus Nijhoff Publishers; 1986.
[10] Onsager L. Reciprocal relations in irreversible processes. I-II, Phys Rev 1931;37:405.
[11] Arefi M, Zenkour AM. Effect of thermo-magneto-electro-mechanical fields on the bending behaviors of a three-layered nanoplate based on sinusoidal shear-deformation plate theory. J Sandw Struct Mater 2019;21:639–69.
[12] Whatmore RW. Pyroelectric devices and materials. Rep Prog Phys 1986;49:1335.
[13] Vinyas M. Computational analysis of smart magneto-electro-elastic materials and structures: review and classification. Arch Comput Meth Eng 2021;28:1205–48.
[14] Brischetto S, Cesare D. A 3D shell model for static and free vibration analysis of multilayered magneto-elastic structures. Thin-Walled Struct 2025;206:112620.
[15] Heyliger PR, Pan E. Static fields in magnetoelectroelastic laminates. AIAA J 2004;42:1435–43.
[16] Brischetto S, Torre R. 3D shell model for the thermo-mechanical analysis of FGM structures via imposed and calculated temperature profiles. Aerosp Sci Technol 2019;85:125–49.
[17] Brischetto S, Carrera E. Coupled thermo-mechanical analysis of one-layered and multilayered plates. Compos Struct 2010;92:1793–812.
[18] Noor AK, Malik M. An assessment of five modeling approaches for thermo-mechanical stress analysis of laminated composite panels. Comput Mech 2000;25:43–58.
[19] Reddy JN. An evaluation of equivalent-single-layer and layerwise theories of composite laminates. Compos Struct 1993;25:21–35.
[20] Reddy JN, Robbins Jr DH. Theories and computational models for composite laminates. Appl Mech Rev 1994;47:147–69.
[21] Tornabene F, Viscoti M, Dimitri R, Reddy JN. Higher order theories for the vibration study of doubly-curved anisotropic shells with a variable thickness and isogeometric mapped geometry. Compos Struct 2021;267:113829.
[22] Li D. Layerwise theories of laminated composite structures and their applications: a review. Arch Comput Meth Eng 2021;28:577–600.
[23] Tornabene F, Viscoti M, Dimitri R. Generalized higher order layerwise theory for the dynamic study of anisotropic doubly-curved shells with a mapped geometry. Eng Anal Bound Elem 2022;134:147–83.
[24] Tornabene F, Viscoti M, Dimitri R. Static analysis of anisotropic doubly-curved shell subjected to concentrated loads employing higher order layer-wise theories. Comput Model Eng Sci 2023;134:1393–468.
[25] Tornabene F. Hygro-Thermo-Magneto-Electro-Elastic Theory of Anisotropic Doubly-Curved Shells. Bologna: Esculapio; 2023.
[26] Washizu K. Variational Methods in Elasticity & Plasticity. Oxford: Pergamon Press; 1975.
[27] Reddy JN. A generalization of two-dimensional theories of laminated composite plates. Commun Appl Numerical Methods 1987;3:173–80.
[28] Reddy JN, Wang CM. An overview of the relationships between solutions of the classical and shear deformation plate theories. Compos Sci Technol 2000;60:2327–35.
[29] Khandan R, Noroozi S, Sewell P, Vinney J. The development of laminated composite plate theories: a review. J Mater Sci 2012;47:5901–10.
[30] Wang CM, Reddy JN, Lee KH. Shear deformable beams and plates: Relationships with classical solutions. Amsterdam: Elsevier; 2000.
[31] Reddy JN, Liu C. A higher-order shear deformation theory of laminated elastic shells. Int J Eng Sci 1985;23:319–30.
[32] Reddy JN. On refined theories of composite laminates. Meccanica 1990;25:230–8.
[33] Bouhadra A, et al. Improved HSDT accounting for effect of thickness stretching in advanced composite plates. Struct Eng Mech 2018;66:61–73.
[34] Thai HT, Choi DH. Improved refined plate theory accounting for effect of thickness stretching in functionally graded plates. Compos B Eng 2014;56:705–16.
[35] Ferreira AJM, Roque CMC, Jorge RMN. Analysis of composite plates by trigonometric shear deformation theory and multiquadrics. Comput Struct 2005;83:2225–37.
[36] Vu TV, et al. Meshfree analysis of functionally graded plates with a novel four-unknown arctangent exponential shear deformation theory. Mech Based Des Struct Mach 2023;51:1082–114.
[37] Murakami H. Laminated composite plate theory with improved in-plane responses. J Appl Mech 1986;53:661–6.
[38] Toledano A, Murakami H. A high-order laminated plate theory with improved in-plane responses. Int J Solids Struct 1987;23:111–31.
[39] Tornabene F, Viscoti M, Dimitri R. Free vibration analysis of laminated anisotropic doubly-curved shell structures reinforced with three-phase polymer/CNT/fiber material. Eng Anal Bound Elem 2024;164:105762.
[40] Tornabene F, Viscoti M, Dimitri R. Effect of thermal and electric coupling on the multifield response of laminated shell structures employing higher-order theories. Compos Struct 2024;1:118801.
[41] Wang J, Yang J. Higher-order theories of piezoelectric plates and applications. Appl Mech Rev 2000;53:87–99.
[42] Tessler A, Di Sciuva M, Gherlone M. Refined zigzag theory for laminated composite and sandwich plates, NASA Technical. Publication 2009:20090007494.
[43] Tessler A, Di Sciuva M, Gherlone M. A consistent refinement of first-order shear deformation theory for laminated composite and sandwich plates using improved zigzag kinematics. J Mech Mater Struct 2010;5:341–67.
[44] Bishara D, Xie Y, Liu WK, Li S. A state-of-the-art review on machine learning-based multiscale modeling, simulation, homogenization and design of materials. Arch Comput Meth Eng 2023;30:191–222.
[45] Gay D. Composite materials: design and applications. Boca Raton: CRC Press; 2022.
[46] Jones RM. Mechanics of composite materials. Philadelphia: CRC Press; 1999.
[47] Stroeven M, Askes H, Sluys L. Numerical determination of representative volumes for granular materials. Comput Methods Appl Mech Eng 2004;193:3221–38.
[48] El Moumen A, Kanit T, Imad A. Numerical evaluation of the representative volume element for random composites. Eur J Mech-A/Solids 2021;86:104181.
[49] Li JY, Dunn ML. Micromechanics of magnetoelectroelastic composite materials: average fields and effective behavior. J Intell Mater Syst Struct 1998;9:404–16.
[50] Mori T, Tanaka K. Average stress in matrix and average elastic energy of materials with misfitting inclusions. Acta Metall 1973;21:571–4.
[51] Kim HS, Hong SI, Kim SJ. On the rule of mixtures for predicting the mechanical properties of composites with homogeneously distributed soft and hard particles. J Mater Process Technol 2001;112:109–13.
[52] Eshelby JD. The determination of the elastic field of an ellipsoidal inclusion, and related problems. Proc R Soc Lond 1957;241:376–96.
[53] Eshelby JD. The elastic field outside an ellipsoidal inclusion. Proc R Soc Lond 1959;252:561–9.
[54] Gavazzi AC, Lagoudas DC. On the numerical evaluation of Eshelby's tensor and its application to elastoplastic fibrous composites. Comput Mech 1990;7(1):13–9.
[55] Li JY, Dunn ML. Anisotropic coupled-field inclusion and inhomogeneity problems. Philos Mag A 1998;77:1341–50.
[56] Mura T. Micromechanics of defects in solids. The Hague: Martinus Nijhoff Publishers; 1982.
[57] Mura T. Inclusion problems. Appl Mech Rev 1988;41:15–20.
[58] Trotta S, Marmo F, Rosati L. Analytical expression of the Eshelby tensor for arbitrary polygonal inclusions in two-dimensional elasticity. Compos B Eng 2016;106:48–58.
[59] Trotta S, Marmo F, Rosati L. Evaluation of the Eshelby tensor for polygonal inclusions. Compos B Eng 2017;115:170–81.
[60] Shi DL, et al. The effect of nanotube waviness and agglomeration on the elastic property of carbon nanotube-reinforced composites. J Eng Mater Technol 2004;126:250–7.
[61] Kundalwal SI, Ray MC. Effect of carbon nanotube waviness on the elastic properties of the fuzzy fiber reinforced composites. J Appl Mech 2013;80:021010.
[62] Tornabene F, Viscoti M, Dimitri R. Effect of porosity on the modal response of doubly-curved laminated shell structures made of functionally graded materials employing higher order theories. Structures 2024;60:105848.
[63] Wang L, Zhou X, Wei X. Heat conduction: mathematical models and analytical solutions. Berlin: Springer Science & Business Media; 2008.
[64] Reddy JN. An introduction to the finite element method. New York: McGraw-Hill; 2005.
[65] Zimmerman WB. Multiphysics modeling with finite element methods. Singapore: World Scientific Publishing Company; 2006.
[66] Zienkiewicz OC, Taylor RL. The finite element method. New York: McGraw-Hill; 1967.
[67] Tornabene F. Generalized Differential and Integral Quadrature. Bologna: Esculapio; 2023.
[68] Shu C, Richards BE. Application of generalized differential quadrature to solve two-dimensional incompressible Navier-Stokes equations. Int J Numer Meth Fluids 1992;15:791–8.
[69] Bert CW, Malik M. Differential quadrature method in computational mechanics: a review. Appl Mech Rev 1996;49:1–28.
[70] Shu C. Differential quadrature and its application in engineering. Berlin: Springer Verlag; 2000.
[71] Shu C, Du H. Free vibration analysis of laminated composite cylindrical shells by DQM. Compos B Eng 1997;28:267–74.
[72] Talebitooti M. Three-dimensional free vibration analysis of rotating laminated conical shells: layerwise differential quadrature (LW-DQ) method. Arch Appl Mech 2013;83:765–81.
[73] Shu C. An efficient approach for free vibration analysis of conical shells. Int J Mech Sci 1996;38:935–49.
[74] Tornabene F, Viscoti M, Dimitri R, Aiello MA. Higher order formulations for doubly-curved shell structures with a honeycomb core. Thin-Walled Struct 2021;164:107789.
[75] Tornabene F, Viscoti M, Dimitri R, Aiello MA. Higher-order modeling of anisogrid composite lattice structures with complex geometries. Eng Struct 2021;244:112686.
[76] Tornabene F. Free vibration analysis of functionally graded conical, cylindrical shell and annular plate structures with a four-parameter power-law distribution. Comput Methods Appl Mech Eng 2009;198:2911–35.
[77] Hsu MH. Vibration analysis of edge-cracked beam on elastic foundation with axial loading using the differential quadrature method. Comput Methods Appl Mech Eng 2005;194:1–17.
[78] Tornabene F, Dimitri R, Viola E. Transient dynamic response of generally-shaped arches based on a GDQ-time-stepping method. Int J Mech Sci 2016;114:277–314.
[79] Hong CC. Transient responses of magnetostrictive plates by using the GDQ method. Eur J Mech-A/Solids 2010;29:1015–21.
[80] Shu C, Khoo BC, Chew YT, Yeo KS. Numerical studies of unsteady boundary layer flows past an impulsively started circular cylinder by GDQ and GIQ approaches. Comput Methods Appl Mech Eng 1996;135:229–41.
[81] Shu C, Chew YT, Richards BE. Generalized differential and integral quadrature and their application to solve boundary layer equations. Int J Numer Meth Fluids 1995;21:723–33.
[82] Chaudhuri RA. On boundary-discontinuous double Fourier series solution to a system of completely coupled P.D.E.'s. Int J Eng Sci 1989;27:1005–22.

[83] Chaudhuri RA. On the roles of complementary and admissible boundary constraints in Fourier solutions to boundary-value problems of completely coupled rth order P.D.E.'s. J Sound Vib 2002;251:261–313.
[84] Tornabene F, Viscoti M, Dimitri R. On the importance of the recovery procedure in the semi-analytical solution for the static analysis of curved laminated panels: comparison with 3D finite elements. Materials 2024;17:588.
[85] Tornabene F, Viscoti M, Dimitri R, Rabczuk T. Thermo-magneto-mechanical analysis of curved laminated structures with arbitrary variation of the material properties and novel recovery procedure. Eng Anal Bound Elem 2025;176:106232.
[86] Tornabene F, Viscoti M, Dimitri R. Thermo-mechanical analysis of laminated doubly-curved shells: higher order equivalent layer-wise formulation. Compos Struct 2024;335:117995.
[87] Tornabene F, Viscoti M, Dimitri R. Equivalent layer-wise theory for the hygro-thermo-magneto-electro-elastic analysis of laminated curved shells. Thin-Walled Struct 2024;198:111751.